



State University of Maringá

Center of Exact Sciences

Graduate Program in Physics

Doctoral Thesis

**Effect of Nb-addition in Bioactive Borate Glasses:
from characterization to application**

Mariana Sversut Gibbin Brandão

Advisor: Dr. Francielle Sato

Co-Advisor: Dr. Vitor Santaella Zanuto

Maringá

July, 2025



State University of Maringá

Center of Exact Sciences

Graduate Program in Physics

Doctoral Thesis

Mariana Sversut Gibbin Brandão

Effect of Nb-addition in Bioactive Borate Glasses: from characterization to application

Doctoral thesis submitted to Graduate Program in Physics at State University of Maringá as a partial fulfillment of the requirements for the degree of Doctor.

Committee:

Francielle Sato, Ph.D - PFI/UEM (Advisor - Chair)

Daniela Martins F. de Oliveira, Ph.D - DQI/UEM (Internal Committee Member)

Raquel Dosciatti Bini, Ph.D - UTFPR (Internal Committee Member)

Franciana Pedrochi, Ph.D - UFMA (External Committee Member)

Laís Dantas Silva, Ph.D - UEMA (External Committee Member)

Vitor Santaella Zanuto, Ph.D - PFI/UEM (Co-advisor - Aux. Committee Member)

Taiana Gabriela Moretti Bonadio, Ph.D - Unicentro (Aux. Committee Member)

Maringá

July, 2025



Universidade Estadual de Maringá

Centro de Ciências Exatas

Programa de Pós-Graduação em Física

Tese de Doutorado

Mariana Sversut Gibbin Brandão

Efeito da adição de Nióbio (Nb) em vidros de borato bioativos: da caracterização à aplicação

Tese de doutorado apresentada ao Programa de Pós-Graduação em Física da Universidade Estadual de Maringá como preenchimento parcial dos requisitos para obtenção do título de Doutor.

Banca Avaliadora:

Dra. Francielle Sato - PFI/UEM (Orientadora)

Dra. Daniela Martins Fernandes de Oliveira - DQI/UEM (Membro Interno)

Dra. Raquel Dosciatti Bini - UTFPR (Membro Interno - Egressa)

Dra. Franciana Pedrochi - UFMA (Membro Externo)

Dra. Laís Dantas Silva - UEMA (Membro Externo)

Dr. Vitor Santaella Zanuto - (Coorientador - Membro Suplente Interno)

Dra. Taiana Gabriela Moretti Bonadio - Unicentro (Membro Suplente Externo)

Maringá

Julho, 2025

Dados Internacionais de Catalogação-na-Publicação (CIP)
(Biblioteca Central - UEM, Maringá - PR, Brasil)

B817e

Brandão, Mariana Sversut Gibbin

Effect of Nb-addition in bioactive borate glasses : from characterization to application /
Mariana Sversut Gibbin Brandão. -- Maringá, PR, 2025.
99 f. : il. color., figs., tabs.

Orientadora: Profa. Dra. Francielle Sato.

Coorientador: Prof. Dr. Vitor Santaella Zanuto.

Tese (doutorado) - Universidade Estadual de Maringá, Centro de Ciências Exatas,
Departamento de Física, Programa de Pós-Graduação em Física, 2025.

1. Vidro de borato bioativo - Aplicações biomédicas. 2. Pentóxido de Níbio. 3.
Hemostasia. 4. Biomateriais. I. Sato, Francielle, orient. II. Zanuto, Vitor Santaella, coorient.
III. Universidade Estadual de Maringá. Centro de Ciências Exatas. Departamento de
Física. Programa de Pós-Graduação em Física. IV. Título.

CDD 23.ed. 530.41

Mariana Sversut Gibbin Brandão

**Effect of Nb-addition in Bioactive Borate Glasses: from
characterization to application**


Doctoral thesis submitted to Graduate Program
in Physics at the State University of Maringá
in partial fulfillment of the requirements for the
degree of Doctor.

Approved on: July 30th, 2025


DOCTORAL COMMITTEE:

Documento assinado digitalmente
 **FRANCIELLE SATO**
Data: 31/07/2025 08:06:21-0300
Verifique em <https://validar.iti.gov.br>


Dra. Francielle Sato - PFI/UEM
Advisor - Chair

Documento assinado digitalmente
 **DANIELA MARTINS FERNANDES DE OLIVEIRA**
Data: 30/07/2025 20:21:01-0300
Verifique em <https://validar.iti.gov.br>


Dra. Daniela Martins Fernandes de Oliveira - DQI/UEM
Internal Committee Member

Documento assinado digitalmente
 **RAQUEL DOSCIATTI BINI**
Data: 30/07/2025 18:42:16-0300
Verifique em <https://validar.iti.gov.br>

Dra. Raquel Dosciatti Bini - UTFPR
Internal Committee Member

Documento assinado digitalmente
 **FRANCIANA PEDROCHI**
Data: 30/07/2025 18:25:38-0300
Verifique em <https://validar.iti.gov.br>

Dra. Franciana Pedrochi - UFMA
External Committee Member

Documento assinado digitalmente
 **LAIS DANTAS SILVA**
Data: 30/07/2025 18:15:02-0300
Verifique em <https://validar.iti.gov.br>

Dra. Laís Dantas Silva - UEMA
External Committee Member

Dedicated to my parents, Mara and Osmar (*in memoriam*), my brother Vitor, and my husband Thiago.

Dedicado aos meus pais, Mara e Osmar (*in memoriam*), ao meu irmão Vitor e ao meu esposo Thiago.

“Each moment is unique and will not be lived again. If we experience each one intensely, there is a greater chance the memory will become deeply imprinted in our minds.”

“Cada momento é único e não o viveremos de novo. Se vivermos com intensidade cada um deles, haverá uma chance maior de a experiência ficar impregnada em nossa memória.”

Ana Claudia Quintana Arantes

ACKNOWLEDGMENT

First of all, I would like to thank God for the gift of life and for the opportunity to meet so many incredible people who have crossed my path, especially during these 3.5 years of Ph.D.

I am deeply grateful to my advisor, Dr. Francielle Sato, for her support, dedication, and guidance not only throughout my academic career, but also in my personal life. I am extremely grateful for the opportunities, for the collaborations that have enriched my profile and my academic training, and for the confidence in my potential.

To my co-advisor, Dr. Vitor Zanuto, thank you for believing that diving into the world of bioactive glasses was a good idea and for accepting to join us. Your contribution was essential not only for this work but also for many other projects that taught me so much. I was able to learn something new every day.

To my external supervisor, Dr. Showan Nazhat, my sincere thanks. Even without references, he welcomed me with open arms at McGill University with kindness, generosity, and patience. His willingness to help and his constant support were fundamental.

I am also grateful to so many other professors who participated in my academic training, who taught me with dedication and empathy every day: Prof. Medina, Prof. Robson, Prof. Malacarne, among others. I carry with me each lesson that certainly contributed to the professional I am becoming.

Here I would like to give special thanks to Prof. Wilson (*in memoriam*), who, among his countless jokes and “idle” chatter, always left a lesson. His easy-going way of teaching hid profound wisdom, and even in the most relaxed moments, there was something valuable to be learned. His departure did not erase his living presence in the memories and hearts of all who had the privilege of knowing him.

I would like to thank the State University of Maringá (UEM), the secretary Mônica, the technicians, and the dear friends I made along the way: Raquel, Henrique, Lidiane, Monique, Eduardo, Jhonatan, Brenno and all the members of GEFF. Your presence made my graduation more enjoyable.

I would also like to thank McGill University, the technicians, and Gil and his family,

research associate who not only helped me with tips but also offered support at various times. A special thanks to the friends I met during my research abroad: Raquel, Thuanne, Raizza, Oksana, Thamiles, and Francisco. Also to Simone and Luiz, who were like parents during my stay in Montreal. Each of you made this experience more meaningful.

To the friends that life has given me: Bianca, who has been by my side since high school; Amanda and Marcos, for the Saturday nights, good conversations, and board games; Andreia, who was a gift from undergraduation; Adne, who even though she is far away is close, seeming like she has never been far away; and Jaque, who appeared in the midst of the chaos and has been a constant support ever since. I also would like to thank Thamires, who patiently listened to my complaints and concerns weekly.

Last but not least, I express my deepest love and gratitude to my family. Thank you to my parents, Mara and Osmar (*in memoriam*), who shaped the person I am today. To my mother, I thank you for being my strength and shelter, for having doubled her roles as mother and father, ensuring that Vitor and I became the people we are today. Your love and dedication were essential at every step of my journey. To my father, who I miss every day, mainly in the most important moments of my life. I wish he were here to celebrate achievements like this, but I carry with me the hope of meeting him. To my brother Vitor, thank you for being who you are. With your unique way, you occupy a huge space in my heart.

To Thiago, my husband and companion every day, even when we are physically apart. Thank you for always being by my side, with love, patience, and understanding. You truly understand the weight and importance of this thesis, and your presence was indispensable in every step of this journey. I thank you for sharing life, difficulties, and each achievement with you.

Finally, I would like to thank the funding agencies CAPES, CNPq, and Fundação Araucária for the financial support that made this research possible.

To each one, my sincere and profound gratitude.

Thank you!

AGRADECIMENTOS

Em primeiro lugar, agradeço a Deus pelo dom da vida e pela oportunidade de tantas pessoas incríveis terem cruzado o meu caminho, especialmente nesses 3,5 anos de doutorado.

À minha orientadora, Dra. Francielle Sato, sou profundamente grata pelo apoio, dedicação e orientação, não apenas ao longo da minha trajetória acadêmica, mas também na minha vida pessoal. Sou extremamente agradecida pelas oportunidades, pelas colaborações que enriqueceram tanto meu perfil e minha formação acadêmica e pela confiança no meu potencial.

Ao meu coorientador, Dr. Vitor Zanuto, obrigada por acreditar que mergulhar no mundo dos vidros bioativos era uma boa ideia e por ter aceitado se juntar a nós. Sua contribuição foi essencial, não apenas neste trabalho, mas também em muitos outros projetos que me ensinaram tanto. Em cada dia de convivência pude aprender algo novo.

Ao meu supervisor externo, Dr. Showan Nazhat, meus sinceros agradecimentos. Mesmo sem referências, me acolheu de braços abertos na McGill University com gentileza, generosidade e paciência. Sua disposição em ajudar e seu apoio constante foram fundamentais.

Sou também grata a tantos outros professores que participaram da minha formação acadêmica, que ensinaram com dedicação e empatia a cada dia: Prof. Medina, Prof. Robson, Prof. Malacarne, entre outros. Carrego comigo cada ensinamento que com certeza contribuíram para a profissional que tenho me tornado.

Aqui cabe um agradecimento especial ao Prof. Wilson (*in memoriam*), que dentre suas inúmeras brincadeiras e conversa “fiada” deixava sempre uma lição. Sua forma leve de ensinar escondia uma sabedoria profunda, e mesmo nos momentos mais descontraídos, havia algo valioso a ser aprendido. Sua partida não apagou sua presença viva na memória e no coração de todos que tiveram o privilégio de conhecê-lo.

Agradeço à Universidade Estadual de Maringá (UEM), à secretária Mônica, aos técnicos, e aos queridos amigos que fiz ao longo do caminho: Raquel, Henrique, Lidiane,

Monique, Eduardo, Jhonatan, Brenno e todos os membros do GEFF. A presença de vocês tornou a pós-graduação mais agradável.

Meus agradecimentos também à McGill University, aos técnicos e ao Gil e sua família, pesquisador associado que não apenas me auxiliou com dicas, mas também ofereceu apoio em diversos momentos. Um agradecimento especial aos amigos que conheci durante a pesquisa no exterior: Raquel, Thuanne, Raizza, Oksana, Thamiles e Francisco. Também à Simone e ao Luiz, que foram como pais durante minha estadia em Montreal. Cada um de vocês tornou essa experiência mais significativa.

Às amigas que a vida me presenteou: Bianca, que está ao meu lado desde o ensino médio; Amanda e Marcos, pelas noites de sábado, boas conversas e jogos de tabuleiro; Andreia, que foi um presente da graduação; Adne, que mesmo longe está perto, parecendo que nunca esteve longe; e Jaque, que apareceu em meio ao caos e tem sido um apoio constante desde então. Quero também agradecer à Thamires, que ouviu pacientemente minhas reclamações e aflições semanalmente.

Por fim, mas não menos importante, expresso meu mais profundo amor e gratidão à minha família. Obrigada aos meus pais, Mara e Osmar (*in memoriam*), que moldaram a pessoa que sou hoje. À minha mãe, agradeço por ter sido força e abrigo. Por ter se desdobrado nas funções de mãe e pai, garantindo que eu e o Vitor nos tornássemos as pessoas que somos hoje. Seu amor e dedicação foram essenciais em cada passo da minha trajetória. Ao meu pai, que tanto sinto falta nos momentos mais importantes da vida. Gostaria muito que estivesse aqui para celebrar conquistas como esta ao meu lado, mas carrego comigo a esperança do reencontro. Ao meu irmão Vitor, obrigada por ser quem é. Com seu jeitinho peculiar, ocupa um espaço imenso no meu coração.

Ao Thiago, meu marido e companheiro de todos os dias, mesmo quando a distância física se faz presente. Obrigada por estar sempre ao meu lado, com amor, paciência e compreensão. Você realmente entende o peso e a importância dessa tese, e sua presença foi indispensável em cada etapa desta jornada. Agradeço por partilhar contigo a vida, as dificuldades e cada conquista.

Por fim, agradeço às agências de fomento CAPES, CNPq e Fundação Araucária pelo apoio financeiro que tornou esta pesquisa possível.

A cada um de vocês, o meu sincero e profundo agradecimento.

Muito obrigada!

ABSTRACT

This thesis investigates the incorporation of niobium pentoxide (Nb_2O_5) into bioactive borate-based glasses synthesized by the melt-quenching method, with the aim of elucidating its structural role and its impact on the properties of these materials, focusing on biomedical applications. Considering the well-known bioactivity of borate glasses and the dual behavior of niobium, as both a network former and modifier, this study evaluates how different Nb_2O_5 contents (0, 2.5, 5, 7.5 and 10 wt.%) affect the glass structure, reactivity, bioactivity, cytocompatibility and hemostatic response. For this purpose, measurements of density, radiopacity, atomic packing factor, and Raman spectroscopy were carried out and confirmed the incorporation of Nb into the glass structure. X-ray diffraction verified the amorphous nature of the materials, while attenuated total reflectance-Fourier transform infrared spectroscopy (ATR-FTIR) indicated a conversion from BO_4 to BO_3 units with increasing Nb content, which is correlated with a decrease in hardness and elastic modulus. Dynamic vapor sorption (DVS) and inductively coupled plasma optical emission spectrometry (ICP-OES) demonstrated a reduction in reactivity and ionic release rates with increasing Nb content, as well as a lower rate of apatite layer formation when immersed in simulated body fluid (SBF). Cytocompatibility with human adipose-derived mesenchymal stem cells was demonstrated, in the presence of the glasses ionic dissolution products, increase proliferation rates in the presence of higher Nb content. On the other hand, Nb-free glasses exhibited superior hemostatic performance, which suggests that, in Nb-addition glasses, the formation of niobate complexes may interfere with ion exchange and coagulation pathways. Overall, the incorporation of Nb into bioactive borate glasses allows for tuning their properties and may enhance their functionality for biomedical applications.

Keywords: Structural Characterization; Bioactivity; Hemostasis; Tissue engineering.

RESUMO

A presente tese investiga a incorporação de pentóxido de nióbio (Nb_2O_5) em vidros bioativos à base de borato sintetizados pelo método de fusão e choque térmico, com o objetivo de elucidar seu papel estrutural e seu impacto nas suas propriedades com foco em aplicações biomédicas. Considerando a reconhecida bioatividade dos vidros de borato e o comportamento dual do nióbio, como formador e modificador de rede, este estudo avalia como diferentes teores de Nb_2O_5 (0, 2,5, 5, 7,5 e 10 wt.%) afetam a estrutura vítrea, a reatividade, a bioatividade, a citocompatibilidade e a resposta hemostática. Para isso, medidas de densidade, radiopacidade, fator de empacotamento atômico e espectroscopia Raman foram realizadas e confirmaram a incorporação de Nb na estrutura vítrea. A difração de raios X indicou a natureza amorfa dos materiais, enquanto a espectroscopia no infravermelho com reflectância total atenuada por transformada de Fourier (ATR-FTIR) indicou uma conversão de unidades BO_4 para BO_3 com o aumento do teor de Nb, o que se correlacionou com a diminuição da dureza e do módulo de elasticidade. As análises de sorção dinâmica de vapor (DVS) e espectrometria de emissão óptica com plasma acoplado indutivamente (ICP-OES) demonstraram uma redução na reatividade e nas taxas de liberação iônica com o aumento do teor de Nb, bem como uma menor taxa de formação de camada apatítica quando imersos em fluido corporal simulado (SBF). A citocompatibilidade com células-tronco mesenquimais derivadas de tecido adiposo humano foi demonstrada na presença dos produtos de dissolução iônica dos vidros, resultando em taxas de proliferação maiores na presença de maior teor de Nb. Por outro lado, os vidros sem Nb apresentaram desempenho hemostático superior, o que sugere que, nos vidros com adição de Nb, a formação de complexos de niobato pode interferir na troca iônica e nas vias de coagulação. De modo geral, a incorporação de Nb em vidros boratos bioativos permite ajustar suas propriedades e pode aprimorar sua funcionalidade para aplicações biomédicas.

Palavras-Chave: Caracterização Estrutural; Bioatividade; Hemostasia; Engenharia de Tecidos.

LIST OF FIGURES

1.1	Effect of temperature on the enthalpy of a glass forming melt.	6
1.2	DTA curve exhibiting a change in specific heat at the glass transition (T_g), an exothermic peak due to crystallization of the glass, and an endotherm due to melting of the crystals formed at the exotherm.	7
1.3	Atomic structural representation of (A) A_2O_3 crystal and (B) A_2O_3 glass. .	9
1.4	Boroxol ring structures in borate glasses.	11
1.5	Borate units where green is tetrahedral boron, pink is trigonal boron, red is BO and blue is NBO.	11
1.6	Superstructural units present in borate glasses: (a) boroxol ring, (b) borate ring, (c) diborate group, (d) metaborate ring, (e) metaborate chain, and (f) pyroborate. The symbol \emptyset indicates bonded oxygen atoms.	12
1.7	Effect of alkali oxide concentration in (a) alkali borate glasses and (b) thermal properties, especially in vitreous transition (T_g).	12
1.8	Mechanism of dissolution and precipitation at the surface of a silicate bioactive glass, where (1) ionic exchange between network-modifying cations and H^+ or H_3O^+ from the solution; (2) hydrolysis of Si–O–Si bonds and formation of silanol groups (Si–OH); (3) formation of a hydrated silica-rich layer and accumulation of Ca^{2+} and PO_4^{3-} ions at the interface, resulting in the precipitation of an amorphous calcium-phosphate-rich phase; (4) crystallization of this phase into a HCA layer, similar to bone mineral, which enables bonding between the glass and the tissue.	18
1.9	Conversion process from bioactive glass to HAp layer in (a) borate-based glasses and (b) silicate-based glasses.	20
1.10	Representations of niobium octahedra. (a) NbO_6 octahedron with Nb–O bonds of different lengths (short in red, normal in black, and long in blue), reflecting the structural asymmetry commonly found in Nb^{5+} containing compounds. (b) Connection between NbO_6 and SiO_4 units via shared oxygen atoms.	23
3.1	Photographic images of Nb-addition in PNCB glasses.	40
3.2	Radiographic images of Nb-addition in PNCB glasses, showing differences in X-ray attenuation as a function of Nb concentration.	41
3.3	Density of Nb-addition in PNCB glasses as a function of Nb_2O_5 content. .	44
3.4	Atomic packing factor (APF) of Nb-addition in PNCB glasses.	46

3.5	DSC curves of Nb-addition in PNCB glasses.	46
3.6	Glass transition temperature (T_g) of Nb-addition in PNCB glasses.	47
3.7	XRD pattern of Nb-addition in PNCB glasses.	49
3.8	ATR-FTIR of Nb-addition in PNCB glasses, where a) are the spectra and b) the estimated boron fraction in tetraordinated sites.	50
3.9	Raman spectra of Nb-addition in PNCB glasses.	52
3.10	Behavior of the peak position (left) and area (right) of Gaussian fit for each vibrational band as a function of Nb ₂ O ₅ content (mol%). The graphs are identified according to the corresponding structural units. The colors of the curves match those used in the spectral fits presented earlier in Figure 3.9.	55
3.11	Hardness and elastic modulus of Nb-addition in PNCB glasses.	56
3.12	Reactivity of as-made Nb-addition in borate glasses through vapor sorption: exposure to 90% RH followed by 0% RH.	58
3.13	Solubility of as-made Nb-addition in borate glasses through immersion in DIW (n=3): pH measurements, and release of boron, calcium, sodium, phosphorous, and niobium ions as measured through ICP-OES.	60
3.14	XRD diffractograms of acellular bioactivity assay in SBF after 1, 3, 7, and 14 days. The indexed phase corresponds to Hydroxyapatite JCPDS 9-0432.	62
3.15	ATR-FTIR spectra of acellular bioactivity assay in SBF after 1, 3, 7, and 14 days.	64
3.16	Cellular Assays: Calcein-AM labeled live huAD-MSC (green), Hoechst 33342 (blue) stained dsDNA and Ethidium Homodimer-1 binding dead nuclei (red) at days 1, 3, 7 and 10, scale bar = 100 μ m.	66
3.17	Cellular Viability based on luminescence of Calcein-AM labeled live and Ethidium Homodimer-1 binding dead nuclei at days 1, 3, 7, and 10.	67
3.18	Cell metabolic activity assessed by absorbance. All experiments were treated with culture supplemented with ionic dissolution products of Nb-Glasses at a concentration of 1.5 mg/mL.	68
3.19	Clotting profiles: G' versus time curves of citrated blood mixed with (a) ionic dissolution products of PNCB and Nb-PNCB:4 glasses and (b) their particles.	70
3.20	Photographic images of citrated blood at the end of tests mixed with ionic dissolution products of PNCB and Nb-PNCB:4 glasses to get 7 and 14 mM.	72
3.21	Photographic images of citrated blood at the end of tests mixed with glass particles at 15 and 30 mg/mL.	73
3.22	Turbidity profiles: FTU vs. time curves of citrated blood mixed with (a) ionic dissolution products and (b) glass particles of Nb-Glasses.	75
3.23	Photographic images of citrated blood at the end of Turbidity tests mixed with ionic dissolution products of Nb-Glasses to get 7 and 14 mM, based on ICP-OES.	77
3.24	Photographic images of citrated blood at the end of turbidity tests mixed with glass particles at 15 mg/mL and 30 mg/mL.	78

LIST OF TABLES

2.1	Glass sample ID and nominal compositions (wt.% and mol%).	27
3.1	Radiopacity (mmAl) of Nb-addition in PNCB glasses.	42
3.2	Average diameter (D_{10} , D_{50} , D_{90}), specific surface area (SSA), average pore width and average pore volume of Nb-addition in PNCB glasses.	43
3.3	Density of Nb-addition in PNCB glasses.	44
3.4	Atomic packing factor (APF) of Nb-addition in PNCB glasses.	45
3.5	Thermal properties (glass transition temperature (T_g), onset of crystallization temperature (T_x) and thermal stability (ΔT)) of Nb-addition in PNCB glasses.	48
3.6	Hardness (H) and Elastic Modulus (E) under different loads for various Nb concentrations.	57
3.7	Clot initiation time, clot stabilization time, and final storage modulus (G') values obtained when citrated blood was exposed to ionic release (CaCl_2 , PNCB, Nb-PNCB:4) or particles (PNCB, Nb-PNCB:4).	71
3.8	FTU initiation time, FTU stabilization time, and final FTU obtained when citrated blood was exposed to ionic release (CaCl_2 , PNCB, Nb-PNCB:4) or particles (PNCB, Nb-PNCB:4).	76

CONTENTS

Abstract	V
Resumo	VI
Introduction	1
Objectives	3
1 Literature Review	4
1.1 Glasses	4
1.1.1 Borate Glasses	10
1.2 Biomaterials	13
1.2.1 Bioactive Glasses	16
1.2.2 Bioactive Borate Glasses	18
1.3 Niobium	21
1.3.1 Nb-addition in Glasses and Bioactive Glasses	22
2 Materials and Methods	26
2.1 Glasses	26
2.1.1 Synthesis	26
2.1.2 Processing Method	27
2.2 Experimental Procedures	28
2.2.1 Radiopacity	28
2.2.2 Particle Size and Textural Properties	28
2.2.3 Density	30
2.2.4 Atomic Packing Factor (APF)	30
2.2.5 Thermal Analysis	31
2.2.6 X-Ray Diffraction (XRD)	31
2.2.7 Fourier Transform Infrared Spectroscopy	32
2.2.8 Raman Spectroscopy	33
2.2.9 Mechanical Properties	33
2.2.10 Dual Vapor Gravimetric Sorption Analyzer	34
2.2.11 Inductively Coupled Plasma Optical Emission Spectroscopy	35
2.2.12 Acellular Bioactivity - Simulated Body Fluid	36

2.2.13	Cellular and biocompatibility assays (<i>in vitro</i>)	36
2.2.14	Blood Coagulation	38
3	Results and Discussion	40
3.1	Glasses	40
3.2	Radiopacity	41
3.3	Particle Size and Textural Properties	42
3.4	Density	43
3.5	Atomic Packing Factor	45
3.6	Thermal Characterization	46
3.7	X-Ray Diffraction	48
3.8	Fourier Transform Infrared Spectroscopy	49
3.9	Raman Spectroscopy	51
3.10	Mechanical Properties	56
3.11	Aqueous Interaction	58
3.12	Ion Release	59
3.13	Acelullar Bioactivity	62
3.13.1	XRD	62
3.13.2	ATR-FTIR	63
3.14	Cellular Assays	65
3.15	Blood Coagulation	69
3.15.1	Storage Modulus	69
3.15.2	Turbidity	74
	Conclusion	79
	Published Manuscripts	82
	References	86

INTRODUCTION

Bioactive glasses are a class of materials widely studied for their regenerative capabilities in both hard and soft tissues, due to their ability to bond with biological systems and promote healing [1–3]. The development of these materials began with Bioglass® 45S5 in the 1970s, which sparked interest in creating alternative formulations based on diverse glass networks, including silicate, phosphate, borate, and borosilicate systems. These different compositions impart specific structural arrangements and chemical profiles that govern crucial properties, such as degradation rate, ionic dissolution behavior, and biological performance [2–4]. The ability to modify these characteristics arises from the tunable nature of glass, allowing researchers to precisely control its reactivity and functionality by altering the network-forming and modifying components [3–5].

Glasses based on borate compositions have emerged as promising candidates in the field of biomaterials due to their ability to degrade rapidly under physiological conditions, thus enabling a swift and controlled delivery of therapeutic ions [4, 6, 7]. This property is especially beneficial in biomedical applications that demand prompt biological responses, including soft tissue regeneration, stimulation of new blood vessel formation, wound repair, and even blood clotting control [4, 8, 9]. Despite these advantages, their elevated solubility can lead to reduced mechanical integrity, posing challenges for certain uses. Moreover, excessive and uncontrolled ion release from highly soluble borate glasses may also induce cytotoxic effects, limiting their safe application in some biomedical contexts [8, 9]. To address this drawback, researchers have explored the incorporation of various network-modifying oxides into the glass matrix, aiming to tune their properties, while maintaining their favorable bioactive performance [4, 8, 9].

A wide range of metal oxides, such as magnesium, zinc, copper, strontium, and titanium, have been incorporated into bioactive glass formulations as network modifiers,

each contributing distinct effects on the material’s structure and biological performance. These elements are capable of altering the connectivity of the glass network by affecting the bond density, which influences critical parameters such as dissolution kinetics, cytocompatibility, and stimulation of cellular activities. For example, the inclusion of copper and zinc has been associated with enhanced angiogenic and osteogenic responses, while elements like silver have demonstrated significant antimicrobial properties [10–14]. The strategic selection of modifiers not only improves the glass characteristics, but also enables the design of multifunctional biomaterials tailored to specific therapeutic needs [5, 15].

Niobium (Nb) has attracted attention as a functional additive in bioactive glasses, where its incorporation has yielded promising enhancements in both structural and biological properties. Interestingly, the role of Nb within the glass network is not limited to that of a conventional modifier, depending on its concentration and the glass composition, Nb can also function as a network former. In some cases, it may simultaneously exhibit characteristics of both roles, contributing to the complexity and versatility of the glass structure. Therefore, this dual behavior allows for adjustments in network connectivity and polymerization, offering opportunities for tailoring the glass properties [15, 16].

The incorporation of Nb oxides, particularly Nb_2O_5 , mainly into silicate matrices has been shown to enhance a variety of key attributes. These include improvements in mechanical strength, such as: increased microhardness, bioactivity through the apatite layer formation, modulation of degradation rates, and favorable cellular responses, including cytocompatibility and angiogenesis stimulation [1, 3, 5, 17, 18]. Furthermore, several studies have highlighted Nb’s ability to support both osteoconductive and osteoinductive processes [3, 5, 19].

While the influence of Nb on the properties of silicate and phosphate glasses has been explored [3, 5, 15], its role within borate glass systems, particularly in relation to bioactivity, cellular interactions, and hemostatic performance, remains less explored. Considering the structural versatility of boron units and the potential dual function of Nb in glass networks, its incorporation into borate matrices may open new findings for bioactive materials. Therefore, this study presents the synthesis and characterization of bioactive borate glasses with varying Nb_2O_5 contents, with a focus on assessing their structural, physicochemical, and biological behavior.

OBJECTIVES

General Objectives

The general objective of this study is to investigate the effects of niobium oxide (Nb_2O_5) incorporation into bioactive borate glasses produced by the melt-quenching method, focusing on their structural, thermal, mechanical, physicochemical, and biological properties to assess their potential for biomedical applications.

Specific Objectives

The specific objectives of this study are summarized as follows:

- Synthesize bioactive borate-based glasses with different Nb_2O_5 contents using the melt-quenching technique;
- Characterize the structural and thermal properties of the glasses by: X-ray diffraction (XRD), Differential Scanning Calorimetry (DSC), Fourier-transform infrared spectroscopy (ATR-FTIR), and Raman spectroscopy;
- Evaluate the physical and mechanical properties of the glasses, including: density, radiopacity, atomic packing factor (APF), hardness and elastic modulus by nanoindentation;
- Determine the aqueous interaction and ion release behavior of the glasses using dynamic vapor sorption (DVS) and inductively coupled plasma optical emission spectrometry (ICP-OES), respectively.
- Assess the *in vitro* bioactivity through immersion in simulated body fluid (SBF) and analysis of apatite layer formation by XRD and ATR-FTIR;
- Investigate the cytocompatibility of ionic dissolution products of Nb-containing glasses with human adipose-derived mesenchymal stem cells (huAD-MSCs);
- Analyze the hemostatic performance of glasses by evaluating their influence on clotting dynamics.

CHAPTER 1

LITERATURE REVIEW

The present literature review aims to highlight fundamental concepts directly related to the central theme of this thesis. This approach seeks to contextualize the problem under investigation and support the proposed study.

1.1 Glasses

The presence of glass in our daily lives is so ubiquitous that it often goes unnoticed. However, its use dates back thousands of years. Obsidian flakes, a naturally occurring volcanic glass, were extensively employed by ancient civilizations as tools and weapons. Also, both Egyptian and Mesopotamian civilizations had already developed glass, even if low quality and produced using rudimentary techniques. They utilized materials, such as sand (SiO_2), combined with sea salt (NaCl), and possibly animal bone remnants found in the embers of fires (as a source of CaO) [20, 21].

Over time, an understanding of the glass manufacturing process was achieved, and by the Middle Ages, production techniques had been refined, enabling the fabrication of higher-quality glass with transparency and mechanical strength. Nevertheless, it was during the Industrial Revolution that glass gained substantial prominence, particularly due to the large-scale production of flat glass and the introduction of molded glass products, such as bottles [20, 21].

The great success of glass is attributed to its optical property of transparency, particularly within the visible region of the spectrum. Additionally, vitreous materials have attracted significant attention due to their long-term durability, especially their devitri-

fication resistance, aqueous corrosion, and chemical degradation. From the 20th century onward, glass began to be studied scientifically, with researchers striving to understand its properties and the characteristics of this highly versatile material, aided by the development of materials science and advanced characterization techniques [20, 22].

The term “glass” originates from the Latin word “glassies”, which refers to ice. The widespread presence of glass in our daily lives is directly linked to its ability to transmit light. From a microscopic perspective, glasses exhibit a disordered atomic structure, similar to liquids, lacking periodicity or symmetry, a characteristic known as isotropy of physical properties, which causes little light scattering. [20, 22].

In 1990, Elliot defined glass as “an amorphous solid that exhibits a glass transition.” However, some materials may also exhibit this transition and not be glass, as polymers. Shelby in 2005 refined this definition in his book, stating that glass is an amorphous solid entirely devoid of long-range periodic atomic structure and that exhibits a glass transition region [20].

Glasses differ from crystalline solids in several aspects. First, crystalline solids exhibit a highly ordered atomic arrangement, with symmetry extending over long-range distances, a feature absent in glasses. Another important distinction lies in their thermal behavior: upon reaching a specific temperature, a single-phase crystalline solid undergoes a sharp transition to the liquid state. In contrast, non-crystalline solids such as glasses experience a gradual transition without a well-defined point, characterized by a progressive increase in fluidity and a corresponding decrease in viscosity [20, 22].

The behavior of glass transformation can be presented in diagrams of enthalpy or volume as a temperature function, illustrated in Figure 1.1. When a vitreous material is in its liquid state at temperatures above its melting point (T_m), structural atomic rearrangements occur upon slow cooling, leading to the formation of long-range periodic networks. Consequently, the enthalpy undergoes an abrupt decrease, transforming the material into a crystalline solid. However, if the liquid is cooled at sufficiently high rates, there is insufficient time for atomic and structural ordering to occur, preventing crystallization and resulting in a continued linear decrease of specific volume and enthalpy. This state is referred to as the supercooled liquid (SCL). In this state, the material exhibits high viscosity, and slight molecular mobility [20].

As cooling progresses, the enthalpy begins to deviate from the equilibrium line, follow-

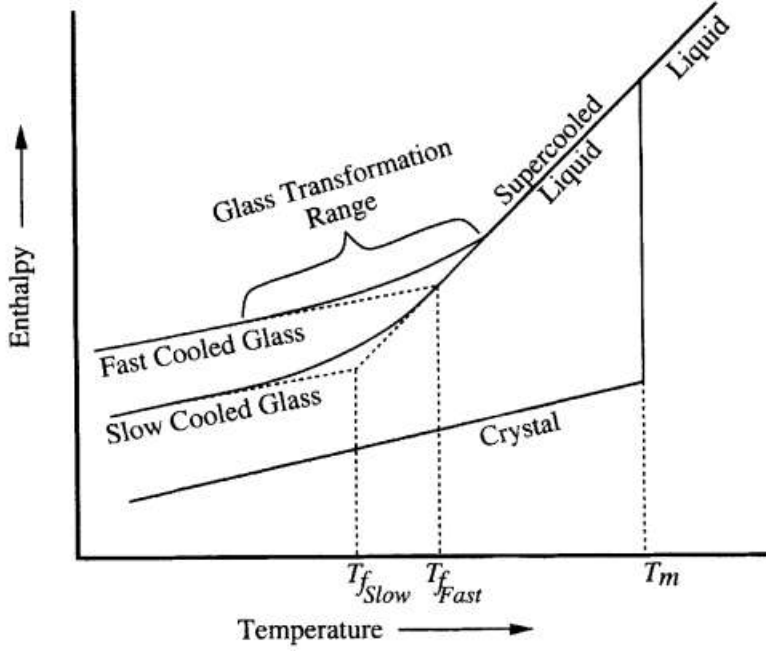


Figure 1.1: Effect of temperature on the enthalpy of a glass forming melt [20].

ing a curve with a gradually decreasing slope. This behavior continues until the material’s heat capacity starts to reflect the characteristics of a rigidly structured liquid. At this point, the viscosity becomes so high that the liquid’s structure “freezes”, meaning it no longer evolves with temperature. The temperature range between the limits where the enthalpy corresponds to that of the equilibrium liquid and that of the non-crystalline solid is known as the glass transition region. The supercooled liquid, now rigidly structured, is referred to as a glass [20].

Considering these characteristics, Brazilian researcher Edgar Zanotto and American researcher John Mauro proposed a more comprehensive and up-to-date definition of glass in their 2017 manuscript "The glassy state of matter: Its definition and ultimate fate," published in the *Journal of Non-Crystalline Solids*. According to the authors, “Glass is a non-equilibrium, non-crystalline state of matter that exhibits a glass transition. Its structure is similar to that of its precursor SCL, and it spontaneously relaxes toward this state. Its ultimate fate, in the limit of infinite time, is to crystallize.” Due to its structural similarities with the SCL, glass is considered a metastable material, it exists in an intermediate state that is not the most energetically stable, but can persist for long periods. Over time, glass tends to slowly relax toward thermodynamic equilibrium, which in the limit of infinite time, is crystallization. This perspective reinforces the dynamic

nature of the glassy state, challenging the notion that glass is a “frozen” and immutable solid [23].

Experimentally, the characteristic temperatures of a given glass can be determined through thermal analysis techniques such as Differential Thermal Analysis (DTA) or Differential Scanning Calorimetry (DSC). Both methods display the material’s characteristic temperatures in the form of DSC curves (thermograms), as shown in Figure 1.2. The main difference between them is that DTA measures the temperature difference between the sample and a reference, whereas DSC measures the variation in energy supplied to the sample relative to a thermally inert reference, allowing DSC to provide information on the enthalpy changes associated with thermal transitions and transformations of a given material [20].

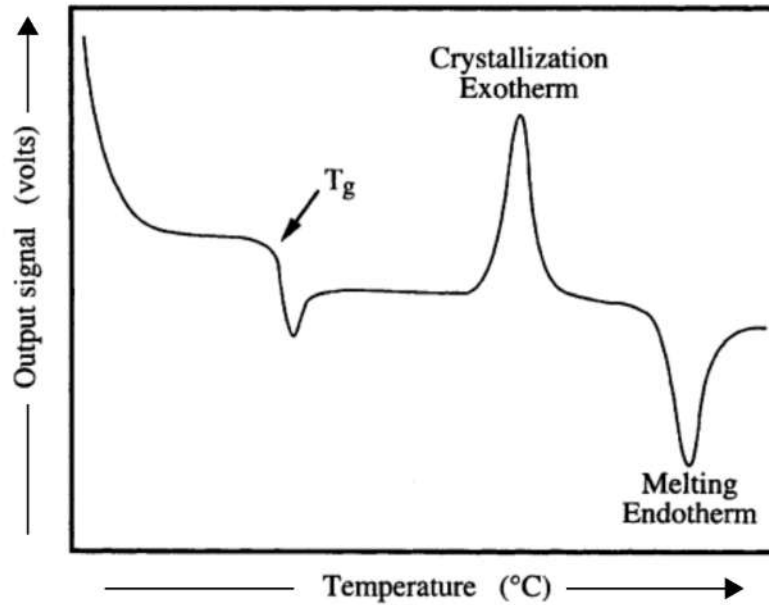


Figure 1.2: DTA curve exhibiting a change in specific heat at the glass transition (T_g), an exothermic peak due to crystallization of the glass, and an endotherm due to melting of the crystals formed at the exotherm [20].

Thus, through the DSC curve, it is possible to observe the characteristic thermal events of glasses, namely: the glass transition temperature (T_g), as previously mentioned, which is identified by a change in the baseline due to a shift in the specific heat capacity (C_p) of the glass sample. Additionally, an exothermic peak is observed, corresponding to the release of internal energy as atoms gain sufficient mobility to structurally reorganize into crystalline phases, this is referred to as the crystallization temperature (T_x at the onset and T_c at the peak). Finally, an endothermic peak appears, where the material absorbs

energy in order to return to the molten state, breaking down the crystalline structure [20].

It is important to note that rapid cooling is applicable to glasses produced by the melt-quenching technique. This method involves weighing the reagents used as raw materials, placing them in a crucible, typically made of a material resistant to high temperatures and non-reactive with the precursors, such as platinum, and heating them in a high-temperature furnace. The molten material is then poured into a preheated stainless steel mold. Subsequently, the glass undergoes a thermal treatment known as annealing, which relieves internal stresses that could otherwise compromise the mechanical properties of the material [20,22].

Other techniques can also be used for glass production, such as sol-gel sintering. This method involves dissolving the precursors in a solvent, followed by hydrolysis and condensation reactions that lead to the formation of a sol (a colloidal suspension of particles). As the condensation process progresses, the particles begin to interconnect, forming a more rigid three-dimensional network, turning the solution into a gel (a solid network with trapped solvent). The gel must be dried to remove the solvent, resulting in hardening of the structure. Although this technique has been gaining prominence in the literature, it is not the focus of the present work [24].

Although sol-gel techniques uses lower processing temperatures, they are generally more time-consuming, involve multiple processing steps [24]. In contrast, melt-quenching enables the production of dense, homogeneous glasses in a single step, with well-established protocols [22]. For these reasons, the present study employed the melt-quenching technique as the most suitable method for producing the bioactive borate glasses.

Additionally, the composition of glasses directly influences their properties, such as thermal behavior. In the classical glass formation theory proposed by Zachariasen in 1932, glasses are described as materials whose atomic arrangement is characterized by a three-dimensional network lacking symmetry. To illustrate this, he presented a two-dimensional comparison between the regular and symmetrical structure of a crystal and the disordered and irregular structure of a glass with the same composition [25], as shown in Figure 1.3.

Based on the concept of a random network, Zachariasen proposed empirical rules to explain the structure of oxide glasses. According to him, for an oxide with the general formula A_mO_n to form a glass, four conditions must be fulfilled:

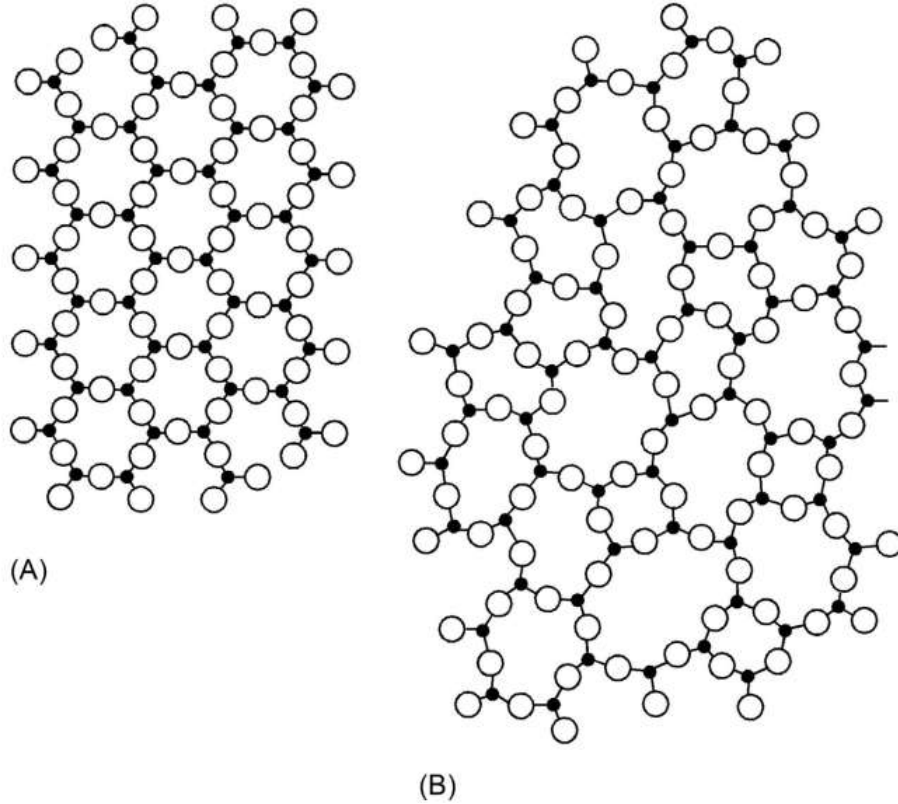


Figure 1.3: Atomic structural representation of (A) A_2O_3 crystal and (B) A_2O_3 glass [22].

1. The number of oxygen atoms surrounding the cation must be small;
2. Each oxygen atom must be bonded to no more than two cations;
3. The polyhedral units should share only corners (vertices), never edges or faces;
4. Each polyhedron must share at least three of its vertices.

Considering these structural properties, the constituent elements of glasses can be classified into three main categories: network formers, modifiers, and intermediates.

Network-forming elements are responsible for creating the fundamental structure of glasses. These elements bond together to form a three-dimensional network, in which oxygen atoms are bonded to central atoms. The most common network former is silica (SiO_2), which serves as the primary basis for silicate glasses. In this structure, silicon bonds with four oxygen atoms to form SiO_4^{4-} tetrahedra, which share their corners. Other notable network formers include boron, which forms borate-based matrices (B_2O_3), and phosphorus, which forms phosphate matrices (P_2O_5). Additionally, network formers combinations can be found, as borosilicates, which incorporate both silica and borate units [20, 22, 25].

Additionally, there are network-modifying oxides, which can not form three-dimensional

networks on their own but interact with network-forming elements to modify the glass structure and, consequently, change its properties. When added, these modifiers occupy voids and imperfections in the original network, breaking and forming new bonds and thus changing the connectivity of the matrix. As a result, network modifiers can generate non-bridging oxygens (NBOs), which significantly influence the thermal, optical, mechanical, and bioactive properties of the glass. Common network oxide modifiers include sodium, calcium, and magnesium, among others. For clarity in structural representation, NBOs are identified by the letter “O”, while bridging oxygens (BOs) are represented by a slashed “Ø”. This visual distinction facilitates the interpretation of the structural units present in the glass network. [20, 25].

Finally, intermediate oxides can not form a network on their own but, when added to an existing network, can act as network formers and exhibit a dual character, also functioning as modifiers that alter the overall structure. Depending on their composition and concentration, they may behave either as formers or modifiers. Examples include aluminum oxide (Al_2O_3), tellurium oxide (TeO_2), niobium pentoxide (Nb_2O_5), among others [16, 20, 25].

1.1.1 Borate Glasses

Borate glasses, following the model proposed by Zachariasen, consist of planar, trigonal BO_3 groups. Since these units are flat, the oxygens are connected to boron through covalent bonds, and the three-dimensional structure is formed by the network “crumpling”, similar to crumpling a sheet of paper into a ball. This 3D network involves van der Waals bonds in the third dimension, which are easily broken, leading to a decrease in the material’s melting point. This structure contrasts with the pyramidal arrangements found in crystalline boron oxide [20].

The triangles are randomly arranged within the glassy matrix and can form bridges with their neighbors through shared oxygen atoms, resulting in a ring system known as boroxol rings (B_3O_6). These rings, in turn, can be connected through shared oxygen atoms or through BO_3 units located outside the rings, which are referred to as isolated BO_3 groups, as shown in Figure 1.4. Although the existence of these groups was first proposed by Goubeau and Keller in 1953, it was not widely accepted for many decades, until neutron diffraction and nuclear magnetic resonance (NMR) spectroscopy data confirmed

that, in borate glass, approximately 70–80% of the boron atoms are present in boroxol groups [26,27].

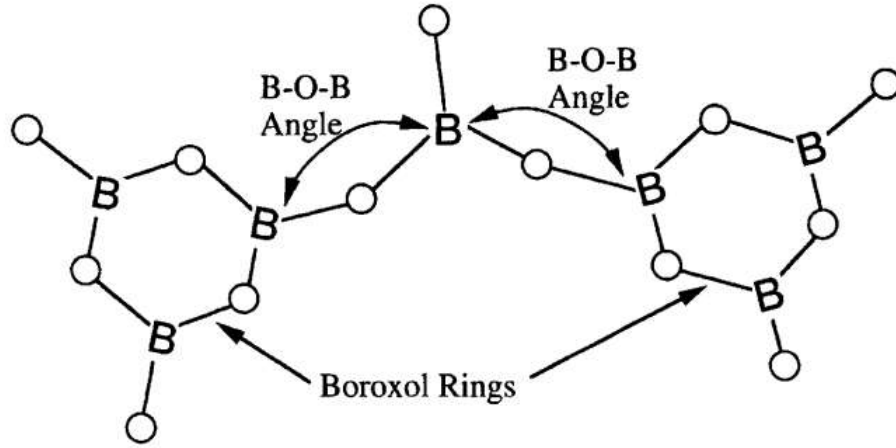


Figure 1.4: Boroxol ring structures in borate glasses [20].

The covalent bonds in the borate glasses are strong enough to prevent bond breakage when a modifier oxide is added, unlike what occurs in silicate and phosphate based glasses. However, in borate glasses, the trigonal BO_3 structure undergoes a coordination change and begins to form tetrahedral BO_4^- groups. These groups are negatively charged but have their charge stabilized by the presence of the modifier cation. Five additional structural units can be formed based on triangles and tetrahedra: i) BO_4^- , ii) BO_3 , iii) BOO_2^- , iv) BO_2O^{2-} , and v) BO_3^{3-} , as seen in Figure 1.5.

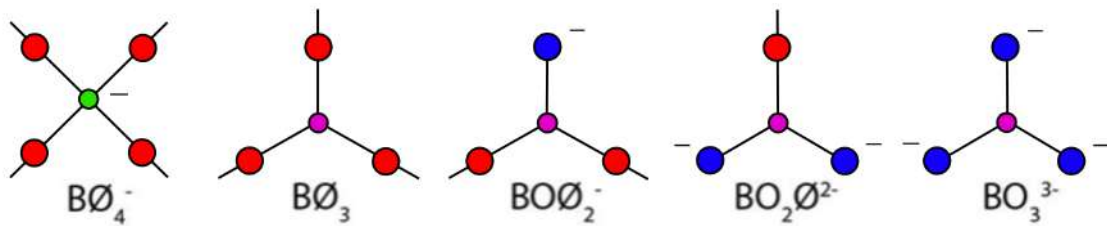


Figure 1.5: Borate units where green is tetrahedral boron, pink is trigonal boron, red is BO and blue is NBO. Adapted from [27].

These units can organize themselves into borate rings containing one or two BO_4^- units and even into larger structures, such as the diborate group. These units are unique in that they do not have freedom internal degrees in the form of variable bond angles or torsional bond angles, except for the diborate group, which is rigidly planar [20]. The boron superstructural units are formed by the combination of basic structural units of borate

glass into more complex structures, according to Figure 1.6. These superstructural units are important because they directly influence the physical and chemical properties [22].

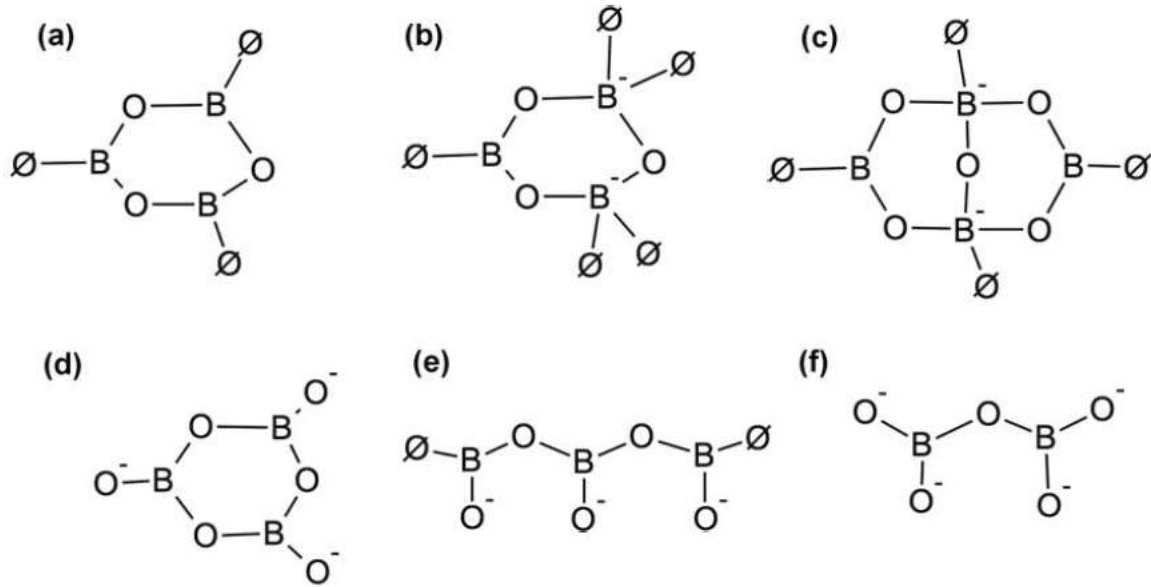


Figure 1.6: Superstructural units present in borate glasses: (a) boroxol ring, (b) borate ring, (c) diborate group, (d) metaborate ring, (e) metaborate chain, and (f) pyroborate. The symbol \emptyset indicates bonded oxygen atoms. Adapted from [28].

Furthermore, with the addition of modifier oxides, significant changes can occur in these structures and consequently in the borate network, potentially leading to nonlinear modifications in various properties and physical characteristics of the glass, giving rise to the borate anomaly, as Figure 1.7a presents, which can also influence the thermal properties, as shown in Figure 1.7b.

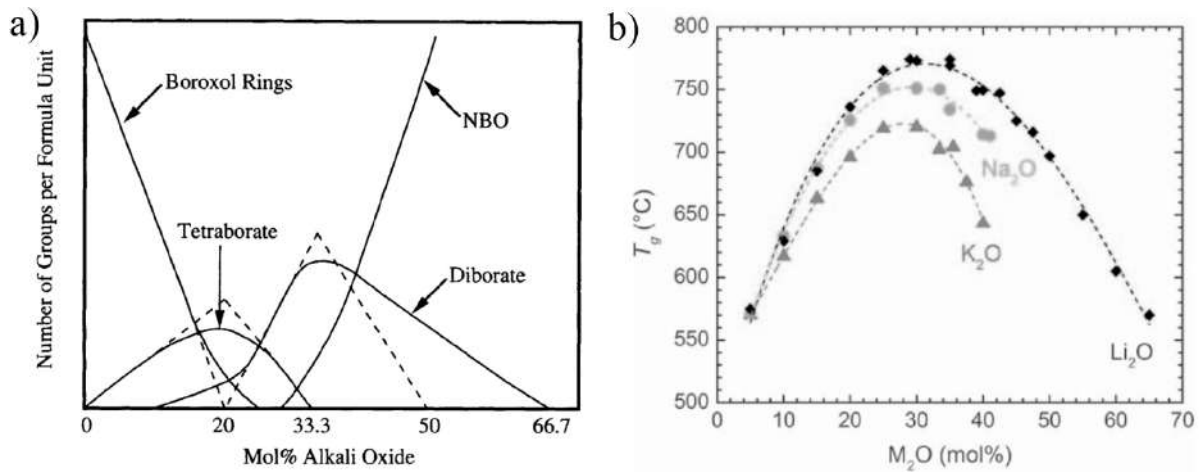


Figure 1.7: Effect of alkali oxide concentration: (a) alkali borate glasses (Dashed lines indicate simple theory and solid lines represent experimental results); (b) thermal properties, especially in vitreous transition (T_g) [20, 28].

1.2 Biomaterials

When human body tissues suffer injuries, lesions, or irreversible degenerative processes, it becomes necessary to adopt strategies that promote their replacement, support, or regeneration. Throughout history, different solutions have been developed to address these biological failures, from the empirical use of natural materials in ancient times, such as silk threads for sutures and animal bone fragments for reconstructions, to the use of metals in dental restorations. Although these materials were not formally classified as “biomaterials”, they already demonstrated the fundamental principle that underlies this field: the controlled interaction between materials and biological systems for therapeutic purposes [29, 30].

Thus, all materials that perform the respective function from living tissues when replaced are referred to “biomaterials”. During conferences, such as the *European Society for Biomaterials* in 1982, the term biomaterial was defined as “any substance or combination of substances, other than drugs, synthetic or natural origin, that can be used for a period of time as part of, or in its entirety, a system that treats, increases, or replaces any tissue, organ, or function of the body.” This definition was later revised in 1991 to: “Biomaterials are materials intended to interface with biological systems to evaluate, treat or replace any tissue, organ, or function of the body” [29, 31, 32].

These definitions have continued to be updated over time. However, fundamentally, a biomaterial can be described as a material that, when in contact with biological tissues, fluids, and intended for use in prosthetic, therapeutic, or diagnostic applications, does not adversely affect the living organism or its components [30, 31].

The development trajectory of biomaterials can be understood in terms of four generations, which reflect not only technological and scientific advances but also conceptual shifts in how these materials integrate with biological systems [29, 32].

The first generation, which emerged in the 1960s and 1970s, was characterized by the use of inert materials, whose primary function was structural. Stable metals, ceramics, and polymers were selected with the goal of minimizing the body’s reaction to the implanted material, thus promoting durability without active interaction with the surrounding tissues. Examples include alumina, zirconia, and polyethylene (PE), which are still used today with morphological-type fixation [33].

The second generation, appearing mainly from the late 1970s, was driven by a new

understanding of biological responses and introduced bioactive or biodegradable materials capable of interacting with surrounding tissues. Notable examples include bioactive glasses and ceramics, as well as synthetic or natural polymers, which stimulate processes such as osteointegration by forming chemical bonds with bone tissue. In other words, these materials are no longer passive but become active, enhancing the connection between the material and the tissue [31,33].

In the third generation, developed from the 1990s onward, the approach evolved toward the development of biofunctional biomaterials capable of modifying cellular behavior. These materials not only support cell growth but also direct regenerative processes through specific signaling mechanisms, such as functionalized surfaces, controlled drug release, and three-dimensional structures for tissue engineering. Essentially, in this generation, materials are capable of regenerating tissues rather than merely replacing them, combining the concepts of bioactivity and biodegradability. Examples include resorbable bone cements, cartilage for joint regeneration, artificial skin, and scaffolds made from bioactive glasses, glass-ceramics, and bioactive ceramics. This generation is extensively studied and refined within the field of tissue engineering [33,34].

Currently, a new generation of biomaterials is under development in the 2020s, aiming to assist in the tissue regeneration process, inspired by recent discoveries of the electrophysiological behavior of cells and tissues. This is the fourth generation of biomaterials, known as smart or biomimetic biomaterials, which is based on the ability of cells and tissues to generate and receive bioelectrical signals. An example is the nanoelectronic scaffold (NanoES) made of macroporous, flexible, and autonomous nanowires, which supports the growth of neuronal and cardiac cells while monitoring local electrical activity within these three-dimensional tissue constructs that are electronically innervated in real time [34].

The properties exhibited by each generation of materials are intended for different functions and applications. However, in general, these materials must not cause adverse biological reactions, whether local or systemic. Therefore, the material must be biocompatible, promoting good integration and harmony in the interaction between the implant and the tissue, without causing disturbances or inducing harmful responses [29,34].

Additionally, biomaterials must exhibit physicochemical stability in the physiological environment to ensure that their structure and functionality are preserved over time. In

cases where controlled resorption is desirable, such as in scaffolds for bone regeneration or drug delivery systems, the material's degradation should occur gradually, in a controlled manner, and without releasing toxic by products [31].

Another fundamental requirement is that the material possesses mechanical properties compatible with the target tissue. For applications in bone tissue, for example, the material is expected to exhibit resistance to compression, tension, and bending, as well as an elastic modulus close to that of natural bone, to avoid excessive stress effects. Conversely, materials intended for the replacement or support of soft tissues should prioritize flexibility, elasticity, and resistance to mechanical fatigue [29, 31].

Processability is also a determining factor, as the biomaterial must allow fabrication into different shapes and sizes, adapting to specific clinical needs. At the same time, it is essential that the material can be sterilized by conventional methods, such as autoclaving, gamma radiation, or ethylene oxide, without compromising its structural, chemical, or biological properties [31].

Depending on the final application and how biomaterials behave, they can also be classified according to the type of tissue-implant interaction. In general, biomaterials can be grouped into four main categories: inert, porous, bioactive, and resorbable [31].

Inert biomaterials, as previously mentioned in the first generation of biomaterials, are those that, once implanted, do not chemically react with the surrounding biological tissues. Their primary function is structural, providing mechanical support without inducing a significant biological response [29, 31].

Porous biomaterials have a structure with interconnected pores that allow cell migration and tissue growth within the material. This porosity promotes biological fixation through the penetration of connective tissue, blood vessels, and, eventually, bone (in the case of orthopedic applications) [1, 31].

Bioactive biomaterials are designed to actively interact with biological tissue, promoting direct chemical bonds with the surrounding tissues, mainly with bone and, in some cases, with soft tissues. This bioactivity is generally achieved through the release of ions or functional groups that stimulate calcium phosphate deposition or by the formation of a hydroxyapatite layer at the material-tissue interface [29, 31].

Finally, resorbable or biodegradable biomaterials undergo gradual degradation in the physiological environment, being progressively replaced by regenerated tissue. Degradation

tion can occur through hydrolytic, enzymatic, or ionic dissolution processes, depending on the chemical nature of the material. These features are characteristic of bioactive borate glasses, whose network structure enables controlled ionic dissolution in physiological environments, allowing gradual replacement by regenerated tissue while promoting the formation of a bioactive hydroxyapatite layer. [29, 31, 35].

Regardless of how these materials are categorized, their essential function is to restore, replace, or promote the regeneration of biological tissues safely and effectively, respecting the complex biophysical and biochemical interactions of the organism. Thus, the selection and design of a biomaterial must always consider its compatibility with the target tissue, its functionality in the biological environment, and its long-term performance [1, 29, 31].

In this context, bioactive glasses have stood out as a promising class of materials precisely because they combine bioactivity, the ability to modulate cellular response, and resorbable potential, characteristics that make them highly versatile and effective in tissue engineering applications. The following sections will discuss in detail the properties, mechanisms of action, and biomedical applications of bioactive glasses [35].

1.2.1 Bioactive Glasses

Classified within the second generation of biomaterials and as bioactive materials, bioactive glasses stand out for their ability to actively interact with biological tissues. Unlike inert materials, which are generally used as physical support, bioactive glasses are capable of triggering specific biological responses that result in stable formation and biologically active interface between the material and the tissue. This characteristic makes them extremely valuable in the development of solutions for tissue regeneration, including in soft tissue engineering [36].

The development of bioactive glasses began in the 1970s, when Larry Hench and his collaborators created the first bioactive glass, known as Bioglass®45S5. This discovery was revolutionary, because it demonstrated that a glassy material could not only be biocompatible, but also form a direct chemical bond with the host tissue. Since then, bioactive glasses have been extensively studied and modified to enhance their performance and clinical applicability [36, 37].

Basically, the material's bioactivity is defined by its ability to undergo chemical reactions. When implanted in the body, due to the biological environment, it results in the

formation of a surface layer rich in calcium phosphate, chemically similar to carbonated hydroxyapatite (HCA) found in the mineral composition of bone tissue. This concept was largely established based on the work of Kokubo and collaborators, who developed an *in vitro* protocol using a solution called Simulated Body Fluid (SBF), whose ionic composition is carefully designed to closely replicate that of human blood plasma. The formation of a hydroxyapatite-like layer during *in vitro* tests in SBF is now widely accepted as an indication of the material’s bioactivity and its potential ability to bond with bone tissue *in vivo* [37, 38]. This layer is not only compatible with biological tissues but also acts as a chemical bridge that enables the formation of a direct and stable bond between the material and the living tissue. This process is essential to ensure the integration of the implant with the host tissue [28, 35, 39].

The original composition of bioactive glasses was based on silicate matrix (SiO_2), which acts as a network former, combined with network-modifying oxides such as calcium oxide (CaO), sodium oxide (Na_2O), and phosphorus pentoxide (P_2O_5). Silica provides the structural framework of the glass network, while calcium and sodium oxides modify this network, making the material more susceptible to controlled degradation in the biological environment. Phosphorus pentoxide directly contributes to the formation of the calcium phosphate layer. The proportion of these components is crucial in determining the final properties of the material, such as dissolution rate, apatite layer formation, and other properties, as well as mechanical properties [28, 35, 39].

The mechanism that imparts bioactivity to glasses is directly related to their interaction with bodily fluids. When a bioactive glass comes into contact with the biological environment, an initial ionic exchange occurs, in which Na^+ and Ca^{2+} ions from the glass are replaced by H^+ or H_3O^+ ions from the solution. This process leads to a local increase in pH and the formation of reactive sites on the glass surface. Subsequently, the breaking of Si-O-Si bonds in the glass network occurs, promoting the formation of silanol groups (Si-OH) on the surface. These silanol groups then undergo condensation, resulting in the formation of an amorphous silica-rich layer. Simultaneously, calcium and phosphate ions from the solution or the glass itself migrate to this surface layer, leading to nucleation and growth of an apatite phase. This layer is fundamental, as it enables adhesion, a schematic representation of this process is shown in Figure 1.8 [28, 35].

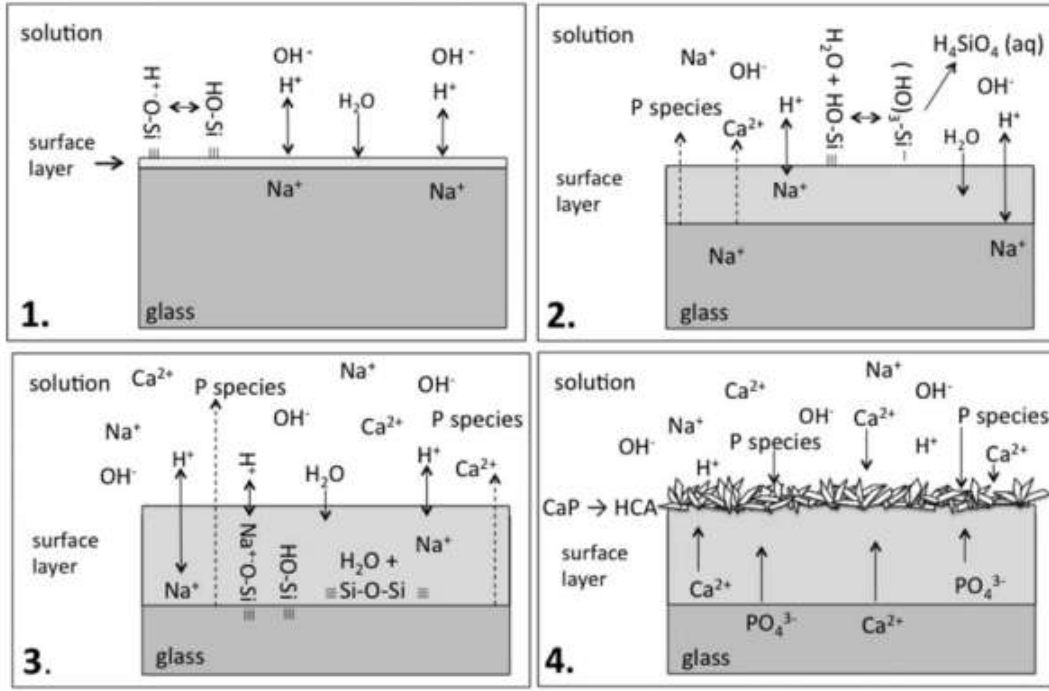


Figure 1.8: Mechanism of dissolution and precipitation at the surface of a silicate bioactive glass, where (1) ionic exchange between network-modifying cations and H^+ or H_3O^+ from the solution; (2) hydrolysis of Si-O-Si bonds and formation of silanol groups (Si-OH); (3) formation of a hydrated silica-rich layer and accumulation of Ca^{2+} and PO_4^{3-} ions at the interface, resulting in the precipitation of an amorphous calcium-phosphate-rich phase; (4) crystallization of this phase into a HCA layer, similar to bone mineral, which enables bonding between the glass and the tissue [28].

With the advancement of research in the field of biomaterials, new formulations of bioactive glasses have been developed by incorporating different oxides into their composition. Borate-based glasses, for example, exhibit a significantly higher degradation rate compared to silica-based glasses, making them promising for applications where faster material resorption is desired. Similarly, the incorporation of elements such as strontium, zinc, copper, silver, and cerium has been explored to provide additional functionalities, such as antibacterial activity, osteogenic effects, and the promotion of neovascularization [10–14, 28].

1.2.2 Bioactive Borate Glasses

Bioactive borate glasses represent an innovative class of biomaterials with distinct properties compared to traditional silica-based bioactive glasses. While they share the core characteristic of bioactivity, borate glasses stand out due to their chemical structure, higher dissolution rate in the biological environment, and remarkable versatility in ionic

incorporation, accommodating a wide range of modifiers within their structure [20, 28].

Chemically, borate glasses by melt-quenching process are based on boron trioxide (B_2O_3), which acts as the network former. The basic structure of these glasses can contain structural units such as trigonal BO_3 and tetrahedral BO_4^- , whose ratio can be adjusted by the addition of network-modifying oxides such as CaO , Na_2O , K_2O , MgO , ZnO , among others. The presence of these units and the nature of the bonding between them give borate glasses distinct characteristics when compared to silicate glasses [10–14, 20, 28].

The growing interest in bioactive borate glasses is largely due to their ability to change cellular responses through the controlled release of bioactive ions into the implant microenvironment. This rapid and continuous release of ions, such as B^{3+} , Ca^{2+} , Na^+ , and PO_4^{3-} , stimulates key cellular processes involved in tissue regeneration, including cell migration, proliferation, and differentiation. Additionally, it positively influences angiogenesis, a critical process for the formation of new blood vessels and, consequently, for the successful regeneration of both bone and soft tissues [28].

From the bioactivity perspective, borate glasses are also capable of forming an HCA-like layer when immersed in physiological fluids or simulated solutions such as SBF, following a mechanism that, although similar to that of silicate glasses, presents particularities related to their less stable network [28, 40]. The mechanism of HCA formation in borate glasses involves multiple steps:

- **Initial ionic exchange:** As soon as the glass comes into contact with the aqueous environment, a rapid exchange of soluble cations from the glass network, such as Na^+ , K^+ , and Ca^{2+} , occurs with H^+ (or H_3O^+) ions from the solution. This process leads to the formation of hydroxyl groups ($-\text{OH}$) on the surface and an increase in the local pH;
- **Hydrolysis and breaking of the borate network:** Unlike silicate glasses, whose structure is based on relatively stable $\text{Si}-\text{O}-\text{Si}$ bonds, the borate network, composed of BO_3 and BO_4^- units, has bonds more susceptible to hydrolysis. Surface hydration breaks the $\text{B}-\text{O}-\text{B}$ bonds, leading to the progressive dissolution of the glass network and the release of borate species and other ions into the solution;
- **Formation of a calcium- and phosphorus-rich layer:** As calcium (Ca^{2+}) and phosphate (PO_4^{3-}) ions are released from the glass or absorbed from the surround-

ing environment, they begin to accumulate at the solid-liquid interface. The local supersaturation promotes the nucleation of amorphous calcium phosphate on the glass surface;

- **Nucleation and growth of apatite:** With the continuous accumulation of these ions, the amorphous calcium phosphate undergoes structural transformations, evolving into a crystalline phase of HCA, chemically similar to that found in human bone. This process is facilitated by the local increase in pH and the presence of functional groups on the surface that act as nucleation sites. The hydroxyapatite layer progressively grows, becoming thicker and more stable, capable of promoting a direct bond with bone tissue or, in some cases, also with soft tissues, depending on the local conditions and the composition of the glass.

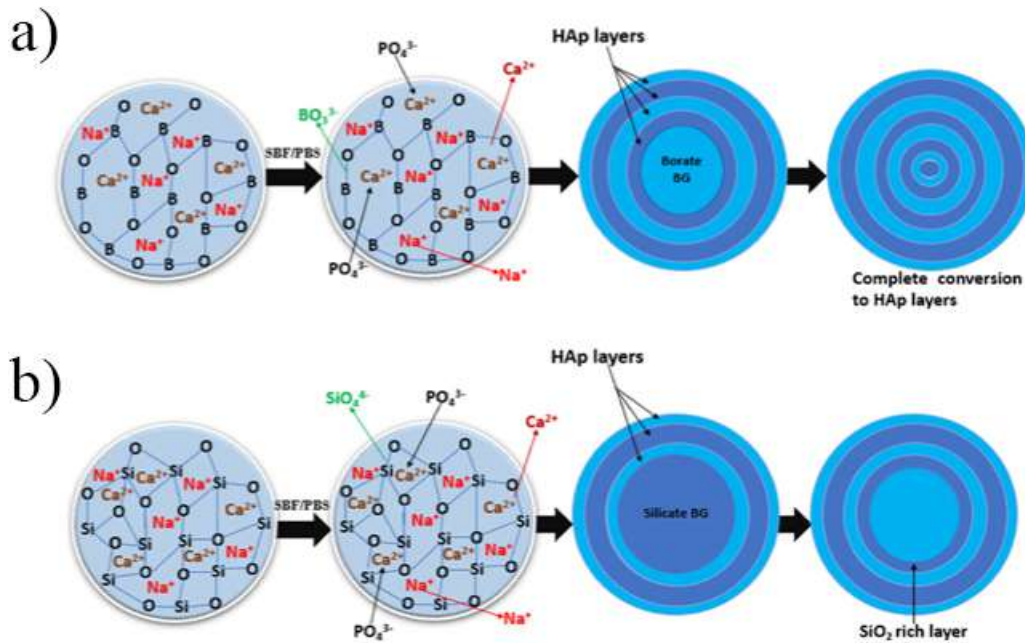


Figure 1.9: Conversion process from glass to HAp layer in (a) borate-based glasses and (b) silicate-based glasses [41].

In contrast to silicate glasses, which form a silica gel layer during the initial stages of the reaction, borate glasses do not develop this intermediate layer, as illustrated in Figure 1.9. Instead, their higher dissolution rate and, consequently, the more immediate availability of ions necessary for the nucleation of the mineral phase, which can be advantageous in applications that require the resorption of the biomaterial within shorter timeframes [28, 41].

One of the great advantages of bioactive borate glasses lies in their ability to be designed as controlled release systems for drugs and therapeutic ions. Boron itself has been associated with beneficial effects on osteoblastic proliferation, but the borate matrix is highly permissive to the incorporation of a wide range of functional ions, such as copper (Cu^{2+}), silver (Ag^+), strontium (Sr^{2+}), zinc (Zn^{2+}), which can impart additional properties to the glass. This versatility has significantly expanded the applications of borate glasses beyond orthopedics and dentistry, reaching fields such as soft tissue engineering and regenerative medicine [10–14, 28].

1.3 Niobium

Building on these advances, recent research has explored the incorporation of niobium as a dopant in glasses [15, 16]. This is a transition metal with the atomic number 41 and atomic weight of 92.906 g/mol. It resides in Group 5 and Period 5 of the periodic table, sharing chemical similarities with tantalum (Ta). The element was first discovered in 1801 by Charles Hatchett and originally named “columbium”. Its name was later changed to niobium, referencing Niobe, Tantalus’ daughter in Greek mythology, highlighting its similarity to tantalum [42].

Niobium is a refractory metal with high corrosion resistance, good thermal and electrical conductivity, and a high melting point. Its main applications are in the steel industry, superalloys, aerospace, energy, and transportation sectors. Niobium is considered a strategic and critical material for defense purposes [42].

Until the 1930s, niobium had few commercial applications. Its use expanded with the production of ferroniobium, used as an alloying element in steels, and niobium carbide, for high-speed cutting tools. Although there are substitutes (molybdenum, tantalum, titanium, tungsten, and vanadium), they can reduce performance or cost-effectiveness. Historically, the main source of niobium was the mineral columbite, extracted in Nigeria as a byproduct of tin mining until the 1960s. After that, large deposits of pyrochlore were discovered and developed in Brazil and Canada, becoming the main global sources [42, 43].

Brazil dominates global production, accounting for over 90% since the 1980s by *Companhia Brasileira de Metalurgia e Mineração (CBMM)*. All pyrochlore concentrate is processed domestically into refined products like ferroniobium and niobium pentoxide, which

are then exported. Canada also became a relevant producer after starting direct ferroniobium production at its Quebec mine in 1994 [42,43].

Niobium is a versatile transition metal that can be incorporated into materials in various forms depending on the application. In its pure metallic form, it is used in superconducting components and thin-film substrates due to its purity and stability [44, 45]. As an alloying element, niobium enhances mechanical properties, being essential in superconducting Nb-Ti magnets, corrosion-resistant Nb-Zr alloys for nuclear reactors, and in high-strength low-alloy (HSLA) steels through grain refinement [46,47]. Its oxide forms, especially niobium pentoxide (Nb_2O_5), are widely used in optics, electronics, catalysis, and as precursors in advanced material synthesis [48].

While niobates like lithium niobate (LiNbO_3) and potassium niobate (KNbO_3) are used in photonic and piezoelectric devices, niobium carbides (NbC) and nitrides (NbN) provide exceptional hardness and wear resistance, being applied in cutting tools and superconducting technologies [49]. These versatile applications are enabled by its electronic structure. Its excellent corrosion resistance arises from a protective Nb_2O_5 layer, making it suitable for harsh chemical environments and biomedical implants [42,43]. These properties underpin niobium’s growing importance in the development of advanced materials, including biomaterials and bioactive glasses.

1.3.1 Nb-addition in Glasses and Bioactive Glasses

Niobium (Nb), in its neutral state, has the electron configuration $[\text{Kr}] 4d^3 5s^2$, following the orbital filling order. However, due to the stability associated with half-filled subshells, it can also be represented as $[\text{Kr}] 4d^4 5s^1$. When incorporated into compounds, such as Nb_2O_5 used in glass, the element is found in the +5 oxidation state, which implies the loss of all five valence electrons. In this state, its electron configuration becomes $[\text{Kr}] 4d^0$. This electronic characteristic enables the Nb^{5+} cation to act as a network former in the glass matrix, typically coordinated to six oxygen atoms to form NbO_6 octahedral units. These units are fundamental to the organization of the glass network and directly influence properties such as chemical stability, reactivity, and the functional behavior of the material [15,16].

However, these octahedra are not perfectly regular, as they exhibit an intrinsic distortion resulting from the second-order Jahn-Teller effect, caused by the interaction between

the empty d orbitals of Nb and the p orbitals of oxygen. As a result, the Nb–O bonds within the octahedron have different lengths: short, normal, and long, as illustrated in Figure 1.10a, leading to slightly or highly distorted octahedra. These octahedra can be distributed in various ways within the glass matrix: they may form clusters or three-dimensional blocks interconnected through Nb–O–Nb covalent corner-sharing bonds, but they can also exist as isolated units, embedded in the glass matrix without direct connections to other Nb octahedra. The presence of such isolated octahedra reflects a greater dispersion of niobium within the network, which also influences the local polarizability, charge distribution, and the optical properties of the material [16].

Another relevant aspect associated with the presence of Nb in glass is the tendency to form structures based on Nb–O–T bonds, where T represents network forming elements, such as Si, P, B, Ge, among others. In compositions containing oxides such as SiO_2 , P_2O_5 , or GeO_2 , the NbO_6 octahedra can share vertices with TO_4 tetrahedra, giving rise to highly connected three-dimensional networks, as shown in Figure 1.10b. These networks exhibit structural cavities that may be compensated by monovalent alkali cations (K^+), which act to neutralize the negative charges generated by the structural units. Unlike other glass systems, these compositions are characterized by the absence of NBOs, since charge compensation occurs predominantly through the local incorporation of modifier cations, thus preserving a high level of connectivity in the glass network [16].

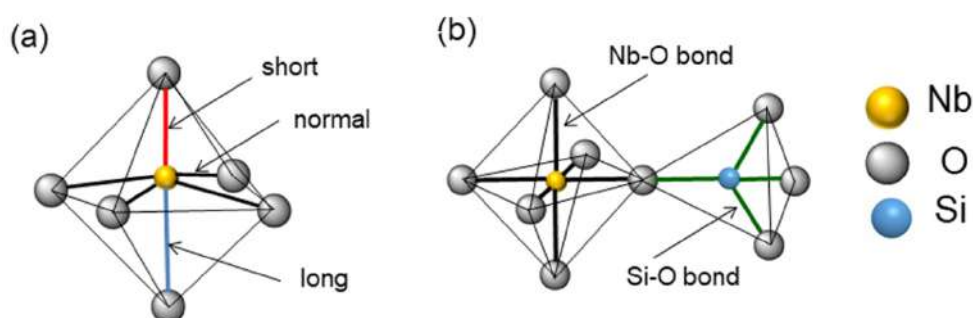


Figure 1.10: Representations of niobium octahedra. (a) NbO_6 octahedron with Nb–O bonds of different lengths (short in red, normal in black, and long in blue), reflecting the structural asymmetry commonly found in Nb^{5+} containing compounds. (b) Connection between NbO_6 and SiO_4 units via shared oxygen atoms. Adapted from [16].

Due to the heteropolymeric bonds such as Nb–O–Si, Nb–O–B, Nb–O–P, Nb–O–Ge, and Nb–O–Te, as well as the covalent bonds of the type Nb–O–Nb, niobium is capable of structuring a connected three-dimensional network. These characteristics classify it as

an intermediate oxide in glass science, meaning that it can act either as a network former or as a network modifier, depending on the system's composition [15].

Although the octahedral NbO_6 configuration is the predominant coordination form of Nb in glasses, there is evidence in the literature that, in certain specific compositions and in highly modified or depolymerized environments, Nb may also be incorporated in the form of tetrahedral NbO_4 units. This configuration, although rare, has been identified in some crystalline compounds, such as LaNbO_4 , and may also occur to a limited extent in glass matrices. The formation of NbO_4 is generally associated with environments rich in network modifiers, which reduce the density of bridging oxygens and favor tetrahedral coordination. Under these conditions, NbO_4 units act as true network formers, establishing Nb–O–Si, Nb–O–P, or Nb–O–B bonds and contributing to the stabilization of the glass network [16].

Therefore, in general, Nb_2O_5 plays an intermediate role in the network of glass systems. Its structural participation occurs through the formation of a highly connected network based on NbO_6 units linked by corners and complemented by bonds with other formers. Moreover, the possibility of these octahedra appearing either as isolated units or in clusters, as well as the occasional incorporation of NbO_4 units in specific environments, allows control over the structural and functional properties of the glasses. This structural arrangement is responsible for imparting to the glasses a combination of high thermal stability, chemical resistance, and optical properties [16].

However, despite the structural influence of Nb in the glass matrix, studies available in the literature do not directly correlate the structural role of niobium with the outcomes related to the bioactivity and cytocompatibility of the glasses. In other words, the local configuration of Nb in the glass network does not appear to have a significant effect on the material's ability to induce the formation of a calcium phosphate-rich bioactive layer or on the *in vitro* cellular response, since this response depends on the other components present in the matrix and their respective amounts.

On the other hand, the presence of Nb in the glass composition has been shown to exert a significant influence on the material's reactivity, which can indirectly affect its bioactive properties, mainly due to the ionic dissolution rate and the control over the release of chemical species at the material/biological medium interface. This occurs because the way Nb is incorporated into the glass network directly affects the degree of

matrix polymerization, the density of oxygen bridges, and the stability of chemical bonds, which in turn modulate the leaching rate of the glass constituents.

Phosphate and silicate glasses containing Nb have tended to exhibit a more controlled dissolution rate, with slower and more gradual ionic release, which is particularly advantageous for biomedical applications requiring bioactive materials with prolonged performance. Due to this characteristic, some studies have reported significant improvements in cytocompatibility. Thus, although the structural role of Nb is not directly reflected in biological indicators of bioactivity and cytocompatibility, it remains of great interest, as it can modulate the rate of dissolution, mineral layer formation, and the release of bioactive species, parameters that are fundamental to the success of bioactive materials [3, 5, 15, 17, 19, 50].

Some studies report the addition of niobium to borate glasses, mostly focusing on structural modifications of the glass network, as well as optical, thermal properties and crystallization processes [51–53]. However, unlike what has been extensively explored in other glass matrices [3, 5, 15, 17, 19, 50], there is still a scarcity of studies that comprehensively address the biological properties of these materials, such as reactivity in simulated media and cytotoxicity. This gap highlights the importance of investigating the bioactive behavior of borate glasses modified with Nb, especially considering their potential for biomedical applications.

CHAPTER 2

MATERIALS AND METHODS

This chapter describes the protocols used, detailing the steps for sample preparation and the specifications of the techniques employed.

2.1 Glasses

Borate-based glasses containing different contents of niobium pentoxide (Nb_2O_5) were synthesized using the conventional melt-quenching technique. The glasses were prepared according to the nominal compositions $60\text{B}_2\text{O}_3 - (19-x/2)\text{CaO} - (19-x/2)\text{Na}_2\text{O} - 2\text{P}_2\text{O}_5 - x\text{Nb}_2\text{O}_5$ (with $x = 0, 2.5, 5, 7.5$, and 10 wt.%), where increasing concentrations of Nb_2O_5 were introduced as an equimolar substitution of the modifiers CaO and Na_2O , as detailed below.

2.1.1 Synthesis

High-purity reagents were used for glass preparation. Specifically, B_2O_3 and P_2O_5 (99.98% purity, Sigma-Aldrich), CaCO_3 (99.95%, Alfa Aesar), Na_2CO_3 (99%, Alfa Aesar), and Nb_2O_5 (99%, supplied by Companhia Brasileira de Metalurgia e Mineração). Each reagent was weighed according to the values presented in Table 2.1, using an analytical balance (Series 202, A&D Company).

Na_2CO_3 and CaCO_3 were degassed at 450 and 900 °C for 2 h to yield Na_2O and CaO , respectively. Both oxides were thoroughly mixed with other elements and well homogenized in an agate mortar, transferred to a platinum crucible, then melted in a

single-step process at a target temperature of 1200 °C for 30 minutes in a platinum crucible, under air furnace conditions. A heating rate of 20 °C/min and a short holding time at the eutectic temperature were applied to minimize volatilization and compositional losses during melting.

The melts were then immediately poured into a 10 mm diameter stainless-steel mold, preheated to 470 °C for 2 h (below the T_g). The resulting glass products underwent annealing in a muffle at the same temperature for 6 h to release internal stresses generated through the quenching process. The samples were properly identified according to the IDs in Table 2.1. All processes were carried out at *Universidade Estadual de Maringá*.

Table 2.1: Glass sample ID and nominal compositions (wt.% and mol%).

Sample ID	B ₂ O ₃		CaO		Na ₂ O		P ₂ O ₅		Nb ₂ O ₅	
	wt.%	mol%	wt.%	mol%	wt.%	mol%	wt.%	mol%	wt.%	mol%
PNCB	60.00	56.65	19.00	22.27	19.00	20.15	2.00	0.93	0.00	0.00
Nb-PNCB:1	60.00	57.91	17.75	21.27	17.75	19.24	2.00	0.95	2.50	0.63
Nb-PNCB:2	60.00	59.22	16.50	20.21	16.50	18.29	2.00	0.97	5.00	1.29
Nb-PNCB:3	60.00	60.56	15.25	19.12	15.25	17.30	2.00	0.99	7.50	1.98
Nb-PNCB:4	60.00	62.04	14.00	17.97	14.00	16.26	2.00	1.01	10.00	2.70

2.1.2 Processing Method

Glass monoliths were cut into 2 mm-thick discs and subsequently polished using a polishing machine with silicon carbide (SiC) abrasive papers with grit sizes of 400, 600, 1200, 1500, 2000, and 2500, respectively, to obtain smooth surfaces suitable for nanoindentation analyses. The discs were also used for radiopacity analysis.

The remaining portion of each glass sample was ground using an agate mortar and pestle, then sieved using stainless steel sieves (ASTM E11, Retsch) to obtain particles within the 25–75 μm size range. Mechanical sieve shaker (AS 200 Basic, Retsch) was employed to assist the process. This particles was used to other analysis including bioactivity assays. Sieving process was carried out at McGill University. While, cutting and polishing were carried out at *Universidade Estadual de Maringá*.

2.2 Experimental Procedures

This section presents the experimental methods, techniques, and procedures employed for the characterization of borate-based glasses containing different contents of niobium pentoxide.

2.2.1 Radiopacity

The radiopacity of the glass samples was evaluated using digital radiography, performed with a dental X-ray unit (model X70, Xdent) operating at 70 kV, 8 mA, and an exposure time of 90 ms, belonging to the *Departamento de Ciências* of the *Universidade Estadual de Maringá - Campus de Goioerê*. For image acquisition, the digital radiographic sensor of 20×30 mm (New Ida, Dabi Atlante) was firmly positioned over foam support, placed at a standardized distance of 15 cm from the X-ray source. To ensure radiological safety, the entire setup was arranged within a lead-shielded environment that prevented the dispersion of ionizing radiation.

The discs samples and an aluminium penetrometer were placed on the sensor, and radiographic image was acquired. Image analysis was performed using Adobe Photoshop CS6 software. The grayscale values of the radiographic images were analyzed using the histogram tool, which provides the average gray level of a selected region on a scale from 0 (black) to 255 (white). For each step of the aluminum penetrometer, the corresponding grayscale value was recorded, creating a standard curve that relates the grayscale intensity to the aluminium thickness (mmAl). The average gray intensity of each glass sample was then measured and compared to the standard curve to estimate its radiopacity in equivalent millimeters of aluminum (mmAl).

2.2.2 Particle Size and Textural Properties

The particle size analysis was carried out using a laser diffraction analyzer (Microtrac SYNC, ATS Scientific Inc.), which operates based on light scattering. This equipment is allocated in Department of Mining and Engineering of the McGill University. In this method, a laser beam is directed at a suspension containing the particles. Isopropanol, with a refractive index of 1.38, was used as the dispersing medium. The analyzed material was considered to have a refractive index of 1.51 [54], with high transparency and irregular

particle shape. The light scattered by the particles is detected by sensors positioned at various angles, allowing the determination of the particle size distribution based on appropriate optical models [55]. Before to each measurement, the ultrasonic bath was activated for 10 s to ensure better dispersion of the particles. Among the evaluated parameters, the D_{10} , D_{50} and D_{90} values were obtained and used for relative comparison between all samples. Median particle size is represented by D_{50} , meaning that 50% of the particles are smaller than this size. While, D_{10} and D_{90} correspond to 10% and 90% of the particle volume that consists of particles smaller than this size, respectively.

The textural properties of glass particles were evaluated using nitrogen gas adsorption and desorption isotherms, obtained with a Automatic Physisorption Analyzer (TriStar II Plus, Micromeritics Instrument Corporation), also belonging to Department of Mining and Engineering of the McGill University. This technique is widely employed for the characterization, enabling the determination of specific surface area and pore volume.

Before to analysis, the samples were degassed under vacuum and heat (120 °C overnight) to eliminate any pre-adsorbed impurities or moisture. The measurements were conducted at 77 K, achieved by immersing the sample holder in liquid nitrogen. During analysis, nitrogen gas is introduced incrementally, and the volume adsorbed is recorded as a function of relative pressure (P/P_o), where P is the equilibrium pressure and P_o is the saturation vapor pressure of nitrogen at 77 K. Once saturation is reached, the pressure is gradually reduced to obtain the desorption isotherm.

The area (S_{BET} or SSA - Specific Surface Area) was determined using the Brunauer–Emmett–Teller (BET) method, which is based on multilayer physical adsorption of gas molecules on the solid surface [56]. The BET equation is applied to the linear region of the adsorption isotherm. From the linear plot, the monolayer adsorbed gas quantity (V_m) is calculated and used to estimate the surface area, taking into account the cross-sectional area of a nitrogen molecule (approximately 0.162 nm²) and the mass of the sample. The results are expressed in m²/g.

The pore volume (PV) was determined using the Barrett–Joyner–Halenda (BJH) method, applied to the desorption isotherm [57]. This method is based on the capillary condensation of nitrogen within the pores of the material and uses the Kelvin equation, which correlates the relative pressure to the curvature of the liquid meniscus and thus to the pore radius. From the desorption data, the amount of gas released at specific pressure

intervals is used to calculate the pore volume corresponding to each pore diameter range. This allows for estimation of the total pore volume (expressed in cm^3/g).

The combination of BET and BJH methods provides a comprehensive characterization of the material's texture, yielding essential information regarding the particles' characteristics.

2.2.3 Density

The density (ρ) of the glass samples was determined using the Archimedes method, performed on glass discs immersed in distilled water at room temperature. Analytical balance (AUW220D, Shimadzu) equipped with the Specific Gravity Measurement kit was used. This apparatus belongs to GEOPT (*Grupo de Espectroscopia Ópticas e Propriedades Termofísicas*) of the *Universidade Estadual de Maringá*. This technique is based on the principle of buoyancy, which states that a body submerged in a fluid experiences an upward force equal to the weight of the fluid displaced [58]. In practice, the method involves measuring the weight of the dry sample in air (W_{air}) and its apparent weight when submerged in fluid, as deionized water (W_{water}). The difference between these two values corresponds to the buoyant force, which is equal to the weight of the displaced water and, consequently, can be used to determine the sample's volume.

Therefore, the density of the glass is calculated using the following equation:

$$\rho = \frac{W_{air}}{W_{air} - W_{water}} \cdot \rho_{water} \quad (2.1)$$

where ρ is the density of the sample (g/cm^3) and ρ_{water} is the density of fluid at the measurement temperature (approximately $0.997 \text{ g}/\text{cm}^3$ at 25°C).

Measurements were repeated three times, and the average value with standard deviation was reported.

2.2.4 Atomic Packing Factor (APF)

The Atomic Packing Factor (APF) is a fundamental parameter in materials science that quantifies how efficiently atoms are packed within a crystalline solid. It is defined as the ratio of the total volume occupied by atoms in a unit cell to the total volume of the unit cell. In the case of crystalline materials, this calculation is straightforward, as the

arrangement of atoms is regular and periodic [59].

For amorphous materials, such as glasses, the atomic arrangement lacks long-range order, making it impossible to define a unit cell in the traditional crystallographic sense. However, an effective APF can still be estimated based on macroscopic parameters such as the molar volume and ionic radii of the constituent elements [60]. In such cases, the APF serves as an indirect measure of the structural compactness or free volume within the glass matrix.

An approximate expression to estimate APF for amorphous systems like oxide glasses, reported by Smedskjaer *et al.* [60], is:

$$APF = \rho \frac{\sum_i f_i V_i}{\sum_i f_i M_i} \quad (2.2)$$

for the i^{th} constituent with the formula $A_x B_y$, f_i is the molar fraction, M_i is the molar mass, ρ is the density, and $V_i = (4/3)\pi N_a(xr_A^3 + yr_B^3)$ is the theoretical volume, where N_a the Avogadro's number and r_A and r_B are the ionic radii, obtained by Shannon [61].

2.2.5 Thermal Analysis

Differential Scanning Calorimetry (STA 449 F3 Jupiter, Netzsch) measurements were carried out to investigate the thermal behavior of the samples, including glass transition, crystallization, and melting events. This equipment is from the P²[AM]² lab at McGill University and the measurements was carried out through collaboration. Approximately 40 mg of powder was accurately weighed and placed into a platinum crucible with a lid. An identical empty platinum crucible was used as a reference.

The samples were subjected to a controlled heating program from room temperature (25 °C) to 1100 °C at a constant heating rate of 10 °C/min. The analysis was conducted under a nitrogen (N₂) atmosphere, using a high-purity nitrogen gas flow rate of 20 mL/min, to prevent oxidative reactions and ensure an inert environment. The thermal events were recorded and analyzed using Proteus software (Netzsch).

2.2.6 X-Ray Diffraction (XRD)

The diffraction patterns were acquired using a diffractometer (D2 Phaser, Bruker) equipped with a CuK_α radiation source ($\lambda = 1.5418 \text{ \AA}$), operating at 40 kV and 30 mA.

Measurements were performed in θ - 2θ geometry, scanning over an angular range of 10 – 60° (2θ) with a step size of 0.02° and a counting time of 2 s per step. The glass particles were positioned on a zero-background sample holder.

For the as-prepared glass samples, the XRD analysis was used to verify the absence of long-range atomic order and to confirm the amorphous structure of glassy materials. Also, it was conducted on the glass samples after immersion in simulated body fluid (SBF) to assess the formation of HCA, a key indicator of *in vitro* bioactivity. In this context, the emergence of characteristic diffraction peaks indicates the formation of crystalline phases on the glass surface. Diffraction patterns were analyzed using X'Pert software, and phase identification was carried out by comparison with standard data from ICDD PDF-2 database.

The equipment used is available in both the *Departamento de Ciências* of the *Universidade Estadual de Maringá – Campus de Goioerê* and the Department of Mining and Materials Engineering at McGill University, both housing the same model. The measurements on the as-prepared amorphous samples were performed at UEM (Goioerê campus), while the measurements after immersion experiments were carried out at McGill University.

2.2.7 Fourier Transform Infrared Spectroscopy

Attenuated Total Reflectance Fourier Transform Infrared Spectroscopy (ATR-FTIR) is a vibrational spectroscopy technique that enables the identification of molecular functional groups based on their characteristic infrared absorption bands. The method relies on the generation of an evanescent wave produced by the total internal reflection of infrared light within a high-refractive-index crystal, when it comes into contact with the sample surface. This wave penetrates a few micrometers into the surface of the sample, allowing direct, non-destructive analysis without the need for extensive sample preparation [62, 63].

In this study, ATR-FTIR measurements were performed using a spectrometer (Vertex 70V, Bruker) equipped with a diamond crystal ATR plate. Equipment belongs to COMCAP (*Complexo de Centrais de Apoio à Pesquisa*) at *Universidade Estadual de Maringá*. Spectra were collected over the range of 4000 to 400 cm^{-1} with a resolution of 4 cm^{-1} and an accumulation of 128 scans. The spectral data were processed using OPUS software, applying baseline correction and vector normalization.

The samples evaluated by ATR-FTIR included bioactive glass particles in two different conditions: as-prepared and after immersion in simulated body fluid (SBF). These are the same samples that were previously subjected to X-ray diffraction (XRD) analysis to investigate the formation of a hydroxycarbonate apatite (HCA) layer, as part of the *in vitro* bioactivity assessment. The ATR-FTIR analysis was aimed at complementing the structural information obtained by XRD, providing insights into the chemical changes that occur on the glass surface during the bioactive response.

2.2.8 Raman Spectroscopy

Raman spectroscopy is a vibrational technique that provides information about molecular structure by detecting inelastically scattered light resulting from the interaction between monochromatic radiation and the molecular vibrations of the sample. Unlike infrared spectroscopy, which measures absorption related to changes in the dipole moment, Raman spectroscopy is based on variations in molecular polarizability, making it particularly sensitive to symmetric vibrations and highly valuable for characterizing glass networks [62, 64].

In this study, Raman spectra were acquired using a Confocal Raman Microscope (Senterra, Bruker) equipped with a 532 nm excitation laser. The equipment is part of the facilities of COMCAP (*Complexo de Centrais de Apoio à Pesquisa*) at the *Universidade Estadual de Maringá*. The laser operated at 100 mW and was focused on the sample using a 20 \times magnification objective lens. Spectral data were collected in the range of 1750 to 400 cm^{-1} , with a spectral resolution between 3 and 5 cm^{-1} . For each sample, 30 spectra were recorded with a detector integration time of 10 s per spectrum. The resulting data were processed using OPUS software, including baseline correction and normalization via the normalization vector. Raman analysis was performed on the glass in the as-prepared condition.

2.2.9 Mechanical Properties

The mechanical properties of the glass specimens, specifically hardness (H) and elastic modulus (E), were evaluated using nanoindentation testing. The nanoindentation equipment, belonging to Professor Richard Chromik's research group at the Department of Mining and Materials Engineering, McGill University, was used in collaboration. This

technique allows for precise, localized mechanical characterization on the submicrometer scale, making it especially suitable for brittle materials, such as glasses, where conventional macroscale mechanical tests may not capture surface-specific or microstructural effects [65].

Nanoindentation tests were carried out using a nanoindenter (NHT², Anton Paar) equipped with a Berkovich diamond indenter ($\varepsilon = 0.74$). The Berkovich tip is commonly used due to its well-defined geometry and ability to produce high spatial resolution indentations. During the tests, the instrument continuously recorded the applied load and the corresponding indentation depth, generating load-displacement ($P-h$) curves. These curves were analyzed using the Oliver and Pharr method [66], a widely accepted approach for extracting the hardness and elastic modulus of materials from the unloading segment of the curve. A Poisson's ratio (ν) of 0.29, as reported in a previous study [67], was assumed for all samples.

For each glass composition, tests were performed on two independent specimens ($n = 2$), with a total of 60 indentations per sample. The indentation array was structured in a 5×12 matrix configuration, allowing spatial distribution of load points while minimizing edge effects and interactions between adjacent indents. The test series was based on the procedure described by D'Andrea *et al.* [68], with indentations distributed across four different maximum loads: 10, 50, 100, and 200 mN (15 indentations per load level). This range of loads was selected to explore the load-dependence of the mechanical response.

The nanoindentation system operated at an acquisition rate of 10 Hz. Loading was applied at a constant rate of 150 mN/min, followed by a holding period of 3 s at maximum load. Subsequently, the load was unloaded to 10% of the maximum over a period of 10 s.

2.2.10 Dual Vapor Gravimetric Sorption Analyzer

Dual Vapor Gravimetric Sorption Analyzer (DVS Resolution, Surface Measurement Systems Ltd.) is an advanced instrument employed to evaluate the interactions of materials with water vapor under precisely controlled environmental conditions. This system operates based on changes in the sample's mass, which are measured with high sensitivity $\pm 0.1 \mu\text{g}$ as it is exposed to varying levels of relative humidity (RH) and different temperature. The equipment is part of the Regen-Eng Lab, led by Prof. Dr. Showan Nazhat at McGill University.

In this study, aqueous interactions of glass particles were investigated to understand their response to high and low humidity conditions. Approximately 10 mg of glass powder was placed in an aluminium pan and inside a chamber in the DVS analyzer. The chamber was strictly maintained at 25 °C and the sample was initially exposed to 90% relative humidity for 24 h, enabling the glass particles to absorb moisture from the atmosphere. During this phase, the instrument continuously recorded mass changes due to water uptake, generating a sorption curve that reflects the kinetics and extent of water adsorption.

Following the sorption phase, the relative humidity was abruptly reduced to 0% RH for an additional 24 h. This desorption phase allowed the system to monitor the release of previously absorbed water as the atmosphere dried. The resulting desorption curve provides insight into the reversibility of water uptake and its interactions. Together, the sorption and desorption data offer valuable information regarding the material's surface properties and water affinity, which are essential for predicting the performance of bioactive glasses in humid or physiological environments.

2.2.11 Inductively Coupled Plasma Optical Emission Spectroscopy

For ion release analysis, glass particles were first dispersed in ultrapure water in 15 mL falcon tubes at a concentration of 1.5 mg/mL. At designated time points, 1, 6, 24, and 72 h, the suspensions (n=3) were filtered through 0.2 μ m nylon membrane filters to remove residual solid particles. The filtrates were subsequently collected and stored in clean 15 mL falcon tubes. Before to analysis, each solution was diluted at a 1:1 ratio with 4% (w/v) nitric acid (Fisher Scientific) to ensure matrix compatibility with inductively coupled plasma–optical emission spectrometry (ICP-OES).

The concentrations of boron, calcium, sodium, phosphorus, and niobium ions released from the glass particles were quantified using an ICP-OES instrument (iCAP 6500, Thermo Fisher Scientific), which is housed in the Department of Chemical Engineering at McGill University. Standard curves were constructed using serially diluted standard solutions of each element: boron, calcium, sodium, and phosphorus at 0, 0.5, 5, and 50 ppm; and niobium at 0, 0.1, 1, and 10 ppm (Fisher Scientific). In parallel, the pH of each solution was measured at the same timepoints using a calibrated pHmeter (Orion

Star A211, Thermo Fisher Scientific) to monitor changes in pH resulting from ion release during the dissolution process, placed at Regen-Eng Lab from Prof. Dr. Showan Nazhat at McGill University.

2.2.12 Acellular Bioactivity - Simulated Body Fluid

Acellular bioactivity of the glass particles was assessed by evaluating their ability to induce apatite formation upon immersion in simulated body fluid (SBF), prepared according to Kokubo's protocol [38]. This solution mimics the ionic composition and concentration of human plasma. All procedures were carried out in Regen-Eng Lab from Prof. Dr. Showan Nazhat at McGill University.

Glass particles were weighed and dispersed in sterile 50 mL falcon tubes containing SBF at a concentration of 1.5 mg/mL. The tubes were incubated in an orbital shaker (KSI 4000 I Control, IKA) set to 120 rpm and maintained at 37 ± 1 °C to simulate physiological conditions [38]. To sustain ionic balance and avoid supersaturation, the SBF was refreshed every 2 days. Samples were collected at defined time intervals: 1, 3, 7, and 14 days ($n = 3$).

The glass particles were separated by centrifugation at 3000 rpm for 10 min (Megafuge 8 Heraeus, Thermo Fisher Scientific) and the supernatant was removed using a pipette. Upon reaching the incubation time, after centrifugation, the samples were rinsed twice with deionized water (DIW) and then with anhydrous ethanol to remove residual ions and prevent further reaction. The rinsed glasses were dried in an oven at 60 °C for 24 h. The dried powders were subjected to X-ray diffraction (XRD) to detect crystalline phases and Fourier-transform infrared spectroscopy (FTIR) to evaluate the formation of phosphate and carbonate functional groups indicative of apatite-like layer development on the glass surface.

2.2.13 Cellular and biocompatibility assays (*in vitro*)

The cells used were from human adipose-derived mesenchymal stem cells (huAD-MSCs; ATCC, PCS-500-011), which were cultured in Dulbecco's Modified Eagle's Medium (DMEM; Gibco), supplemented with 10% (v/v) fetal bovine serum (FBS; HyClone) and 1% penicillin/streptomycin (Gibco), and maintained at 37 °C in a humidified incubator with 5% CO₂. Experiments were conducted using cells between passages 4 and 6, harvested at approximately 70% confluency via enzymatic dissociation with 0.05% Trypsin-

EDTA (Gibco). All cell culture experiments were carried out at the Regen-Eng Lab, under the supervision of Prof. Dr. Showan Nazhat, at McGill University

Based on DVS analysis, the three most reactive samples were chosen for cellular evaluation: PNCB, Nb:PNCB:1, and Nb:PNCB:4. The medium containing ionic dissolution was obtained through a controlled dissolution process. Initially, the glass particles were added to supplemented culture medium at 1.5 mg/mL. This mixture was incubated for 6 h, allowing the ions to be released, and this period was chosen based on the ionic release test in ultrapure water. After this period, the medium containing the dissolution products was carefully filtered using a 0.2 μm nylon membrane in order to remove any residual particles. Therefore, cells were seeded at a density of 4000 cells per well in 96-well plates and allowed to adhere for 24 h, and the resulting filtrate was then used to replace the cell culture medium, allowing the biological effects of the ions released from each glass composition to be evaluated.

Cell viability and metabolic activity were treated by medium containing the dissolution products for a period of 1, 3, 7, and 10 days. At each time point, cultures were washed three times with Dulbecco's Phosphate-Buffered Saline (D-PBS; Gibco) and assessed via Live/Dead and WST⁻¹ assays, as previously described by Lepry *et al.* [69].

For the Live/Dead assay, a staining solution was prepared using 1 μL calcein-AM (4 mM; AAT Bioquest), 2 μL EthD⁻¹ (2 mM; Tocris Bioscience), and 2 μL Hoechst 33342 (18 mM; Tocris Bioscience) diluted in 1 mL D-PBS. Cells were incubated with the staining solution at 37 °C for 30 min. Fluorescence signals were measured using a microplate reader (Synergy H1, BioTek) at excitation/emission wavelengths of 485/528 nm (calcein-AM) and 528/617 nm (EthD⁻¹). Representative fluorescence images were acquired using an inverted fluorescence microscope (Axio Observer 5, Carl Zeiss).

Metabolic activity was quantified using the Cell Proliferation Reagent WST⁻¹ (Roche, Sigma-Aldrich), following the manufacturer's protocol. Briefly, 100 μL of fresh culture medium and 10 μL of WST⁻¹ reagent were added to each well, followed by incubation at 37 °C for 2 h. Absorbance was then recorded at 440 nm using a microplate reader. All experimental conditions were performed in triplicate.

Statistical analysis was conducted using Prism 7 (Graphpad). The cellular assays data followed a normal distribution (Shapiro-Wilk test), and a two-way ANOVA analysis was performed, followed by Tukey's test ($p < 0.05$).

2.2.14 Blood Coagulation

Citrated whole bovine blood (CL1700-500C, Cedarlane) was used to evaluate the hemostatic potential of the glass particles and their ionic dissolution products. The ElastoSens Bio² instrument (Rheolution Inc.) was employed to monitor real-time changes in the shear storage modulus (G') of blood, an indicator of coagulation dynamics. All these measurements were carried out at the Regen-Eng Lab, supervised by Prof. Dr. Showan Nazhat, at McGill University.

This equipment uses a contactless and nondestructive technology called VeTBiM. This technology induces free resonance using pulse vibrations, and an optical probe captures the resonance spectrum. Using known properties of the membrane and structure. Data collected from this dynamic response, including excitation and response spectra, are used to compute the G' , a key parameter in determining the stiffness and clotting behavior of blood. The contactless nature of the setup ensures the samples remain intact and available for further analysis [70, 71].

Two glass compositions were selected for this experiment: PNCB and Nb:PNCB:4, representing the extreme compositions (without Nb and with the maximum Nb content), respectively, to investigate whether the incorporation of niobium had any effect on blood coagulation. Groups containing the glass dissolution products were tested at concentrations of 7 mM and 14 mM, based on ion release data obtained via ICP-OES and 6 h of immersion. For groups containing glass particles, concentrations of 15 mg/mL and 30 mg/mL were used.

Each 6 mL sample was prepared by combining 4 mL of citrated whole bovine blood with 2 mL of either: (i) deionized water containing the glass dissolution products (7 mM or 14 mM), or (ii) deionized water containing suspended glass particles. In the latter case, the glass particles were first added directly to the sample holder, followed by the addition of the blood and water. Positive controls consisted of 7 mM and 14 mM calcium chloride (CaCl_2 , Sigma-Aldrich) solutions, while the negative control was composed of citrated blood with no CaCl_2 addition.

Sample preparation was completed within approximately 30 seconds. After the addition of all components, the sample was homogenized by pipetting up and down three times to ensure even distribution of ions or particles. Coagulation analysis was initiated immediately after homogenization.

The sample holder had a total capacity of 7 mL. After sample placement, an anti-evaporation liquid layer was added to preserve the sample volume and maintain its properties during measurement, as described [70]. All analyses were conducted in a measurement chamber maintained at 37 °C to simulate physiological conditions.

Before to testing, the blood was incubated at 37 °C for at least 30 min. The bovine blood was obtained from a single 500 mL batch, stored at 4 °C, and used within a maximum period of 7 days. G' values were recorded over 60 min with a temporal resolution of 30 s. Temporal evolution of G' was used to determine the activated coagulation time, defined as the point at which G' began to rise sharply.

To complement the mechanical data, the turbidi.T instrument (Rheolution Inc., Canada) was employed to assess blood clotting by measuring light scattering at 850 nm, reported in Formazin Turbidity Units (FTU). This optical analysis provided insight into the optical density and clot formation dynamics based on turbidity changes.

Each sample was placed in 4 mL vials and consisted of 1.33 mL of citrated whole bovine blood and: (i) either 2.66 mL of deionized water (DIW) containing 7 or 14 mM of glass (PNCB and Nb:PNCB:4) ionic dissolution products; (ii) glass particles at 15 and 30 mg/mL, which were directly added to the vial containing 2.66 mL of DIW and 1.33 mL of citrated blood. Calcium chloride (CaCl_2 , Sigma-Aldrich) in 7 and 14 mM was used as a positive control, while citrated whole bovine blood without CaCl_2 was investigated as a negative control. The equipment was calibrated before each measurement using DIW. Tests were carried out on the same bovine blood batch tested through ElastoSens Bio². FTU values were recorded over 60 min with a temporal resolution of 30 s. Temporal changes were used to determine the reaction time.

It was not possible to maintain the initially proposed ratio of water or ionic solution (1:3) to bovine blood (2:3), as this proportion led to saturation of turbidity. Therefore, the proportions were adjusted to 2:3 for the water or ionic solution and 1:3 for the bovine blood. Due to this methodological modification, the data obtained are not directly comparable to the results from the ElastoSens Bio².

CHAPTER 3

RESULTS AND DISCUSSION

This chapter is dedicated to analysis and discussion of results obtained for glasses. The data generated through the characterization methods and experimental protocols will be interpreted based on the scientific literature, aiming for a comprehensive understanding of the material.

3.1 Glasses

Figure 3.1 shows photographic images of borate glasses obtained by the melt-quenching process, containing different concentrations (wt.%) of niobium pentoxide (Nb_2O_5). In Figure 3.1a, the glasses are shown directly after the quenching process. It can be observed that all compositions resulted in translucent glassy materials, with no visible evidence of macroscopic crystallization.

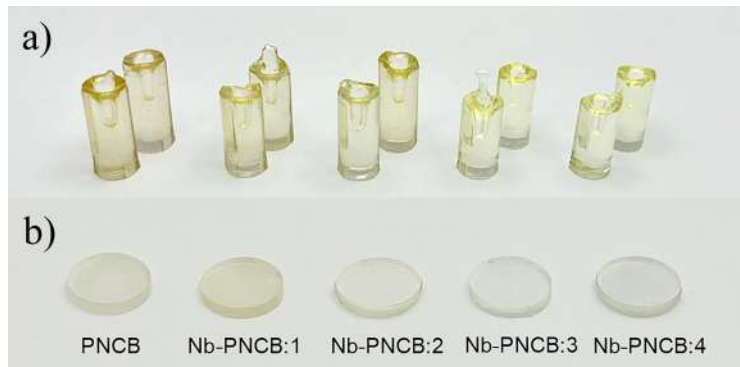


Figure 3.1: Photographic images of the borate glass samples: (a) cylindrical pieces obtained after the melt-quenching process and (b) polished disk-shaped Nb-addition in PNCB glasses.

It is noted that the PNCB, Nb-PNCB:1, and Nb-PNCB:2 compositions exhibit a slightly yellowish coloration, which is typical of borate glasses. In contrast, the Nb-PNCB:3 and Nb-PNCB:4 compositions show a clearer coloration, which may indicate that structural changes have occurred, possibly due to the incorporation of Nb, as a network former or modifier, which will be further analyzed and discussed in the following sections.

In Figure 3.1b, the polished discs for each composition are displayed. All of which exhibit good physical integrity with no visible cracks, bubbles, or defects.

3.2 Radiopacity

Elements with higher atomic numbers are strongly associated with greater radiopacity, a crucial property for clinical applications that require precise radiographic monitoring. This is particularly important in fields such as dentistry, endodontics, and orthopedics, where clear differentiation between the material and surrounding anatomical structures is essential [18, 72–74].

Niobium is one of these elements. The digital radiographs of the glasses, shown in Figure 3.2, exhibit distinct grayscale patterns that progressively change with increasing Nb content. This behavior is attributed to the fact that niobium directly influences X-ray absorption due to its relatively high atomic number and density [72]. As a transition metal, the incorporation of Nb increases the overall material density [15, 75], which consequently enhances its ability to attenuate X-ray radiation.

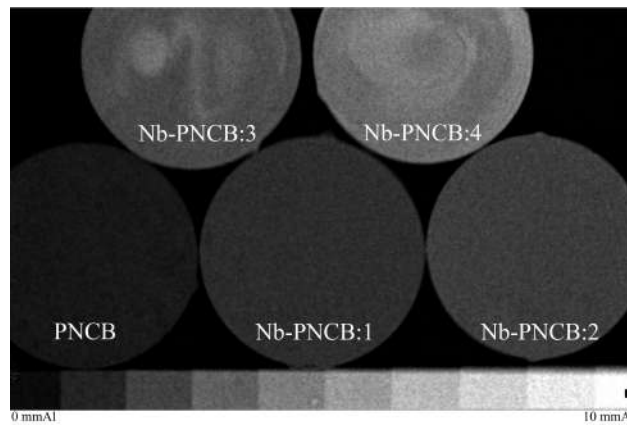


Figure 3.2: Radiographic images of Nb-addition in PNCB glasses, showing differences in X-ray attenuation as a function of Nb concentration.

This trend is visually evident: samples with higher Nb content display lighter areas in the radiographs, indicating greater radiopacity. Conversely, glasses with lower Nb content are more transparent (darker in the image). This progressive increase in radiopacity is quantitatively confirmed in Table 3.1.

Table 3.1: Radiopacity (mmAl) of Nb-addition in PNCB glasses.

Sample	Radiopacity (mmAl)
PNCB	1.38
Nb-PNCB:1	2.18
Nb-PNCB:2	2.75
Nb-PNCB:3	3.48
Nb-PNCB:4	4.77

However, it can be highlighted that PNCB, Nb-PNCB:1, and Nb-PNCB:2 samples exhibit homogeneity in the radiographic images, with a uniform distribution of contrast, confirming the gradual incorporation of Nb into the glass and enhancing its ability to attenuate X-ray radiation. While, Nb-PNCB:3 and Nb-PNCB:4 presented significantly lighter regions in the radiographic images, indicating greater local X-ray absorption. Although all samples appear macroscopically homogeneous, this observation suggests that higher Nb concentrations may influence the viscosity of the eutectic during melting and potentially leading to the formation of clusters or microdomains enriched in metal oxides [76]. These microstructural features could contribute to the observed heterogeneous distribution of radiopacity at higher Nb levels.

3.3 Particle Size and Textural Properties

Particle size and textural properties are critical parameters in determining the performance of glasses, particularly in applications related to dissolution behavior, bioactivity, and interaction with biological environments. Controlling these parameters is essential to tailor the material's performance for targeted biomedical applications. Table 3.2 summarizes the main results.

All compositions were ground to a similar median particle size, obtaining a D_{10} of $41.76 \pm 1.68 \mu\text{m}$, D_{50} of $65.4 \pm 1.7 \mu\text{m}$ and D_{90} of $100.83 \pm 1.96 \mu\text{m}$ to directly compare their

textural properties. The specific surface area (SSA) was approximately $0.10 \text{ m}^2/\text{g}$ for all samples, which is within expected range for glasses produced by melt-quenching [6], and substantially lower than those generated through chemical routes [4, 77].

Table 3.2: Average diameter (D_{10} , D_{50} , D_{90}), specific surface area (SSA), average pore width and average pore volume of Nb-addition in PNCB glasses.

	PNCB	Nb-PNCB:1	Nb-PNCB:2	Nb-PNCB:3	Nb-PNCB:4
$D_{10} \text{ (}\mu\text{m)}$	40.73	41.34	44.59	41.80	40.33
$D_{50} \text{ (}\mu\text{m)}$	64.65	65.09	68.14	65.38	63.71
$D_{90} \text{ (}\mu\text{m)}$	101.10	99.66	103.60	101.40	98.39
SSA (m^2/g)	0.10	0.11	0.10	0.09	0.11
Pore width (nm)	2.20	6.38	5.57	5.55	5.31
Pore volume ($\cdot 10^{-4} \text{ cm}^3/\text{g}$)	5.84	5.83	5.03	5.51	6.04

A notable change was observed in pore width: it increased from 2.20 nm in the PNCB sample to 6.38 nm in Nb-PNCB:1. However, further Nb additions resulted in a slight reduction, reaching 5.31 nm in the Nb-PNCB:4 composition. This trend may reflect a structural reorganization of the glass network, where the introduction of Nb leads to cross-linking of modifiers or the formation of Nb-rich microdomains that restrict further pore growth [16]. Such microstructural rearrangements may also correlate with the radiopacity behavior observed at higher Nb contents.

Conversely, pore volume values were consistent across all compositions, averaging at $5.65 \pm 0.39 \text{ cm}^3/\text{g}$. These observations suggest that, while Nb content influences pore size distribution, it has minimal impact on overall pore volume under the processing conditions used in the production of the particles.

3.4 Density

In glass systems, density changes are directly influenced by the type and proportion of oxides incorporated into the network. The addition of heavier oxides, such as niobium, typically leads to an increase in density due to their higher atomic mass and intrinsic density. Consequently, monitoring density becomes essential for evaluating how the incorporation impacts the glass structure.

In this case, glass density (ρ) gradually increased with the rise in Nb content, as expected due to the higher density (4.6 g/cm^3) and molecular weight (265.81 g/mol) of Nb_2O_5 compared to other glass components, as shown in Figure 3.3. The replacement of CaO and Na_2O by Nb_2O_5 further contributes to this densification effect [4, 77], resulting in an increase of nearly 2% compared to the PNCB.

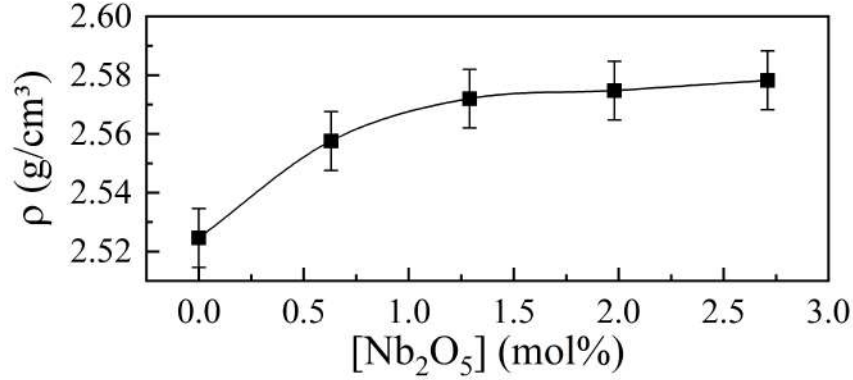


Figure 3.3: Density of Nb-addition in PNCB glasses as a function of Nb_2O_5 content.

It is interesting to highlight that at higher concentrations, beyond Nb-PNCB:2, the density reached a plateau tendency, as summarized in Table 3.3. The rate of density increase becomes negligible, indicating a potential saturation point in the structural accommodation of Nb within the glass network [16].

Table 3.3: Density of Nb-addition in PNCB glasses.

Composition	Density (g/cm^3) ± 0.01
PNCB	2.52
Nb-PNCB:1	2.56
Nb-PNCB:2	2.57
Nb-PNCB:3	2.57
Nb-PNCB:4	2.57

This behaviour suggests that, beyond a certain concentration, the incorporation of Nb into the glass matrix may occur through distinct structural configurations. Instead of continuing to contribute linearly to network densification, Nb atoms may begin to occupy sites or local structural units that do not significantly enhance packing density [16].

3.5 Atomic Packing Factor

The introduction of different oxides can modify the APF by altering the glass network atomic coordination and spatial occupancy impacting its physical and mechanical properties [60]. The calculation was performed according to Equation 2.2.

It was found that the addition of Nb_2O_5 at the expense of CaO and Na_2O resulted in an increase in the APF value from 0.598 to 0.610 in Nb-PNCB:2, according to Figure 3.4. This suggested that a larger fraction of the glass total volume is occupied by atoms, resulting in a denser structure. This behavior indicates that Nb is increasingly participating in the glass network as a network-forming component, contributing to a more compact atomic arrangement.

However, APF decreased to 0.608 in Nb-PNCB:4, suggesting a tendency toward decay, thereby displaying an anomalous trend. Probably, this reduction in the APF, despite the incorporation of a denser oxide, indicates that an excess of Nb promotes the formation of structural defects, suggesting a shift in the role of Nb. The values are summarized in Table 3.4. The literature reveals a dual character of niobium in glass structures: network former or modifier. When it acts as a modifier, the glass network may be disrupted, compromising structural compactness [16].

Table 3.4: Atomic packing factor (APF) of Nb-addition in PNCB glasses.

Composition	Atomic packing factor (APF) ± 0.002
PNCB	0.598
Nb-PNCB:1	0.606
Nb-PNCB:2	0.610
Nb-PNCB:3	0.609
Nb-PNCB:4	0.608

A similar behavior has been detected in soda-lime-borate systems, which reached a maximum at 0.597 then decreased to 0.595 for compositions of 15 and 35 mol% Na_2O [60]. It is worth noting that the density of these glasses also plateaued at higher Na_2O content at the expense of the network-forming B_2O_3 , similar to Nb-glasses, Figure 3.3. Additionally, Na_2O contributes to the densification of the network by converting BO_3 to more efficiently packed BO_4 units. However, beyond a critical concentration (25 mol%), the formation of NBOs becomes dominant, leading to a decrease in network connectivity

and packing efficiency. Moreover, the change in APF affected their thermal and structural properties [60].

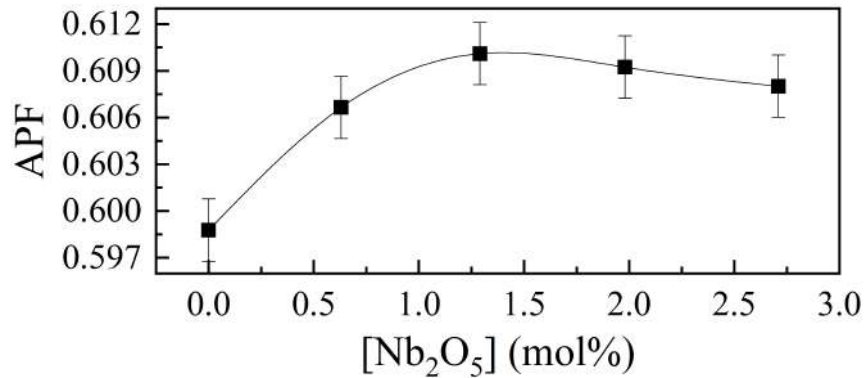


Figure 3.4: Atomic packing factor (APF) of Nb-addition in PNCB glasses.

3.6 Thermal Characterization

Differential Scanning Calorimetry (DSC) analysis was used to investigate the thermal behavior of the samples. Figure 3.5 shows the DSC curves obtained for the samples.

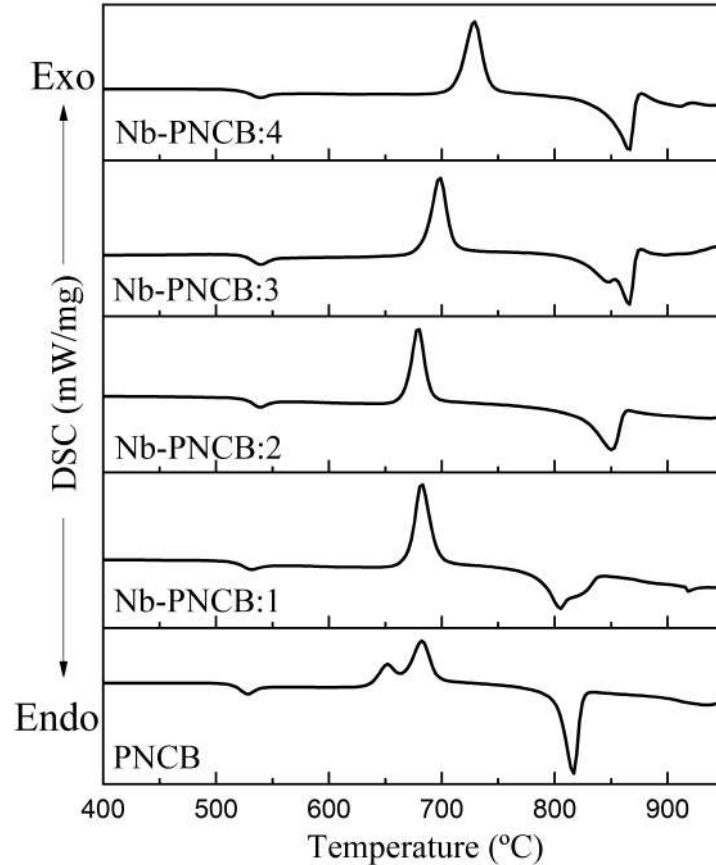


Figure 3.5: DSC curves of Nb-addition in PNCB glasses.

A single endothermic step corresponding to the glass transition temperature (T_g) was observed for all samples, followed by the onset of crystallization (T_x), and a subsequent exothermic peak associated with the crystallization temperature (T_c). The presence of a single T_g confirmed the homogeneity of the as-prepared glasses, which is plotted in Figure 3.6 as a function of Nb content.

At lower Nb_2O_5 contents, a tendency to increase in T_g is observed, up to Nb-PNCB:2. For higher Nb_2O_5 contents, specifically Nb-PNCB:3 and Nb-PNCB:4, a decrease is observed. Due to the well-known structural anomaly of boron, the addition of modifier oxides to the glass network generally leads to a gradual increase in T_g , until a certain concentration is reached, at which point this behavior stabilizes and eventually reverses, resulting in a decrease, as illustrated in Figure 3.6. However, in the present study, this inversion was observed with the addition of approximately 2 mol% of Nb_2O_5 . If the sum in mol% of the modifying oxides is considered, there is a reduction of 43.35 from PNCB to 37.94% for Nb-PNCB:4, which would indicate that the T_g value should always increase. Therefore, the hypothesis for this anomalous behaviour is the dual role of Nb in the glass network. A network that is more connected increases the T_g due to the raises the energetic barrier for structural relaxation and network less connected decrease this parameter.

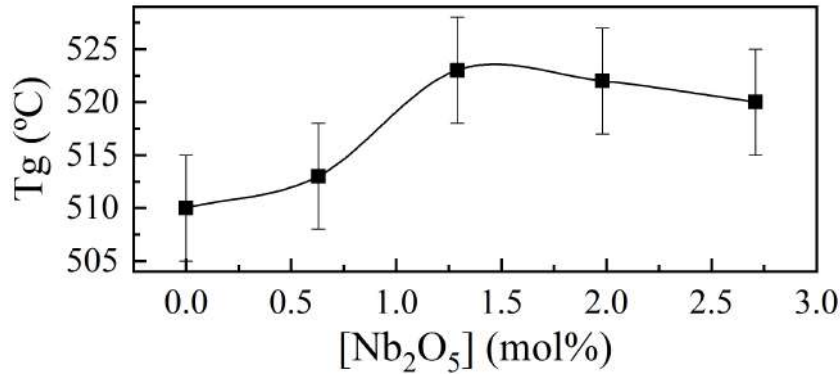


Figure 3.6: Glass transition temperature (T_g) of Nb-addition in PNCB glasses.

Basically, if Nb_2O_5 is incorporated as NbO_6 unit, forming covalent Nb-O-Nb linkages, the connections increase the crosslinking density through corner-sharing octahedra, enhancing the rigidity of the network [15,16]. However, if occurs an excess of NbO_6 units that must be accommodated in the structure, localized structural distortions may be formed, increasing the formation of non-bridging oxygen (NBOs). In this aspect, Nb could then be considered to act as a network modifier [15,16].

Changes signal a partial transition of Nb from a network former to a modifier, disrupting the continuous network and reducing the overall packing efficiency, as also observed in the APF values of Nb-PNCB:3 and Nb-PNCB:4. Furthermore, it no longer generates the densification effect, creating a saturation point. As a result, T_g shows a slight decline, reflecting a more depolymerized structure.

It is also observed that the PNCB sample exhibits two crystallization peaks, possibly indicating the formation of two distinct crystalline phases, a feature that is suppressed upon the addition of Nb. Furthermore, the presence of Nb-rich structural motifs within the glass matrix may hinder the nucleation of crystalline phases, contributing to the observed increase in T_x and in the thermal stability parameter ($\Delta T = T_x - T_g$), as shown in Table 3.5. This enhancement in thermal stability can be attributed to Nb–O bonds that are strong and contribute to increasing the energy barrier required for atomic rearrangement during crystallization [60].

The continued rise in T_x , even as T_g slightly decreases, suggests that these Nb-containing structures disrupt the network in a way that prevents crystallization. This behavior is similar to that observed in glasses containing network modifiers, where structural disruption does not necessarily lead to crystallization, due to the decoupling between network relaxation and the diffusion kinetics of the modifier ions [60]. Overall, the thermal properties also reflect the dual role of Nb, which tend to acts as former at lower contents and transitions toward a modifier role at higher, influencing both T_g and T_x through structural depolymerization.

Table 3.5: Thermal properties (glass transition temperature (T_g), onset of crystallization temperature (T_x) and thermal stability (ΔT)) of Nb-addition in PNCB glasses.

	PNCB	Nb-PNCB:1	Nb-PNCB:2	Nb-PNCB:3	Nb-PNCB:4
T_g (°C)±5	510	513	523	522	520
T_x (°C)±5	635	662	663	680	711
ΔT (°C)±10	125	149	140	158	191

3.7 X-Ray Diffraction

XRD analysis was performed on the glass particles, with the diffractograms showing no sharp diffraction peaks and instead presenting a broad diffuse halo characteristic of amorphous materials, observed in Figure 3.7. Notably, the broad scattering becomes

wider as the Nb content increases, which can be associated with increased structural disorder and the introduction of different local structural units into the glass matrix. The incorporation of Nb may lead to variations in bond lengths and angles, contributing to greater disruption of the medium-range order, thereby broadening the amorphous halo.

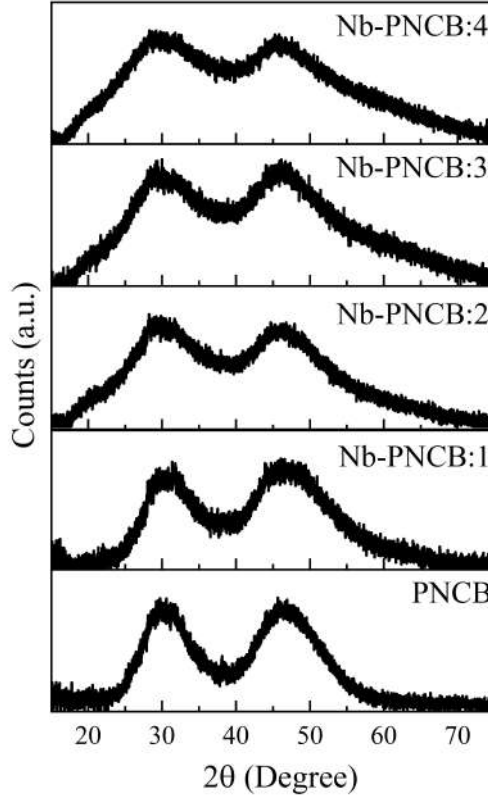


Figure 3.7: XRD pattern of Nb-addition in PNCB glasses.

3.8 Fourier Transform Infrared Spectroscopy

ATR-FTIR spectroscopy was used to analyze the molecular structure of the glasses. The spectra are presented in Figure 3.8a. It is possible to identify the three main regions that are associated with borate-based glasses. In particular, the bands between 1200 and 1500 cm^{-1} can be attributed to the vibrational mode of B–O stretching in BO_3 , while the B–O stretching of BO_4 units are present at 850–1200 cm^{-1} and B–O–B bending of BO_3 at 700 cm^{-1} [51, 78]. The broad band at approximately 950 cm^{-1} signifies the B–O linkages within BO_4 , whereas the B–O stretching of boroxol rings is highlighted by the shoulder around 870 cm^{-1} [79–82].

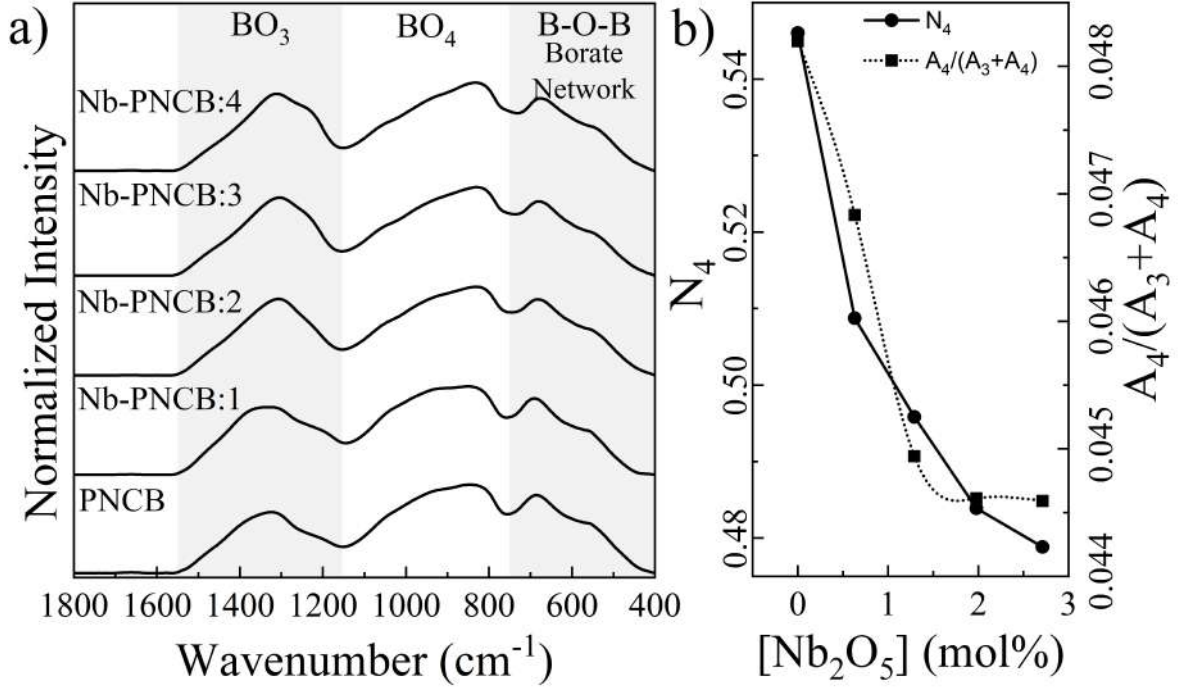


Figure 3.8: ATR-FTIR of Nb-addition in PNCB glasses, where a) are the spectra and b) the estimated boron fraction in tetracoordinated sites.

It is possible to perform a semi-quantitative analysis of boron coordination by integrating the bands corresponding to BO₃ and BO₄ units. The N₄ borate basic units are considered indicative of the network connectivity in borate-based glasses. Although the N₄ fraction is typically determined using boron nuclear magnetic resonance (NMR) spectroscopy, it can also be estimated by FTIR through the following equation [83,84]:

$$N_4 = \frac{A_r}{\alpha + A_r} \quad (3.1)$$

where A_r is the ratio between the areas associated with boron tetrahedra and boron triangles and α is the relative integrated absorption coefficient of 4-coordinated versus 3-coordinated boron. However, this coefficient may change depending on composition. For example, Hübner *et al.* reported $\alpha=1.3$ for SrO-B₂O₃ [85], whereas, Lepry and Nazhat obtained $\alpha=1.5$ for sol-gel calcium-borate systems [84] and Yiannopoulos *et al.* [83] reported $\alpha=1.9$ for glasses containing Mg. Therefore, it is possible to consider an intermediate α value ($\alpha=1.5$) as a slight approximation for N₄ calculation, as shown in Figure 3.8b.

A second method was considered to verify the consistency of the results. In this case, the analysis was based on the parameter A₄ and A₃+A₄ ratio, where A₃+A₄ is the total

spectra integration. The behavior obtained from this method was found to be similar to that observed for N_4 , showing a decreasing trend of tetrahedral boron fraction with increasing of Nb_2O_5 content.

The increase in Nb content leads to a progressive reduction in BO_4 units, revealing that the incorporation of Nb_2O_5 modifies the glass network connectivity. This structural reorganization is characterized by network depolymerization, as the decrease in BO_4 units, leads to a less polymerized borate network dominated by BO_3 units.

The high density and typical coordination number of Nb^{5+} , predominantly six, due to the formation of NbO_6 octahedra, can initially compensate for the reduction in BO_4 units. This behaviour supports the hypothesis previously proposed: up to Nb-PNCB:2, Nb acts primarily as a network former, where NbO_6 units contribute to maintaining and even enhancing the network connectivity, due to their corner-sharing octahedra. However, as the Nb content increases beyond this threshold, the glass network struggles to accommodate the excess NbO_6 units without inducing localized structural distortions. This leads to an increase in NBOs [15, 16] and the conversion from BO_4 to BO_3 continues occurring, becoming the network increasingly disrupted.

In summary, NbO_6 contribute to network densification and structural reinforcement due to their larger coordination volume, becoming the glass network structurally more connected, even as BO_4 units decline. At higher Nb_2O_5 contents, the continued reduction in BO_4 units, decrease in APF, reduction in T_g , and plateauing of density reflect a transition of Nb former to a modifier.

3.9 Raman Spectroscopy

The incorporation of alkaline oxides into borate glasses induces significant structural modifications, particularly through the formation of various polyborate units. Raman spectroscopy is a powerful tool for identifying and characterizing these structural groups [86, 87]. The distribution and relative abundance of borate units within each glass composition are highly dependent on both the type and concentration of network formers and network modifiers present [88]. Figure 3.9a shows the Raman spectra of the Nb-containing borate glasses investigated in this study. Non-bridging oxygens (NBOs) are denoted as “O”, while bridging oxygens ($B\emptyset$) are represented by “ \emptyset ”. This notation is

adopted just in this section to facilitate the identification of oxygens and their correlation with specific structural units.

The presence of bands around 1131 and 526 cm^{-1} indicates borate arrangements containing BO_4 tetrahedra [83, 86, 89, 90], which are related to diborate units, whether connected or isolated, respectively [89, 90]. When the Nb amount is increased, a reduction in this vibrational mode can be detected and consequently, it may be related to the decrease in bridging oxygens [86].

According to Yiannopoulos *et al.*, the band at 1475 cm^{-1} may be associated with the stretching of $\text{B}\text{O}_2\text{O}^-$ units, mainly attached to the segment of borate network [83, 88, 91], breaking these connections can cause a reduction in band intensity. Furthermore, depending on modifications caused by the concentrations of alkali and alkaline earth oxides, a slight shift of these bands may be exhibited in agreement with Konijnendijk and Stevels [87].

The spectral region between 1050 and 600 cm^{-1} is characterized by overlapping vibrational modes. To resolve these contributions, Gaussian deconvolution is employed as an effective method for separating individual bands. This approach enables a more detailed and accurate analysis of the structural units, particularly in cases where band overlap hinders precise identification.

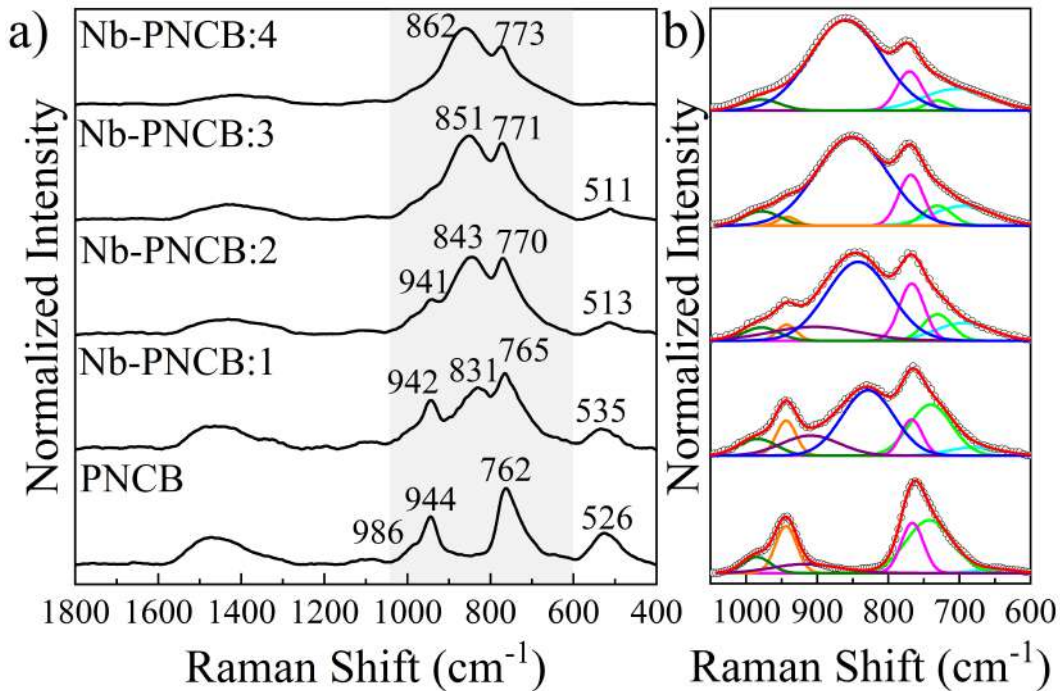


Figure 3.9: Raman spectra of Nb-addition in PNCB glasses.

Deconvolution enables the extraction of clearer band profiles, as shown in Figure 3.9b. The red line corresponds to the sum of gaussian fit and its correspondence with the experimental spectrum (open dots). The area and peak position behavior for each band as a function of the Nb content is plotted at the end of this section (Figure 3.10), with the respective fit colors. The cyan band centered at 648 cm^{-1} for PNCB is attributed to metaborate groups, specifically the fraction of $\text{B}\text{O}_2\text{O}^-$ triangles, which is arranged in metaborate rings ($\text{B}_3\text{O}_6^{3-}$) and manifested as a result of symmetric breathing vibration [83,86,88,89]. For Nb-addition in glasses, this band moves up to 703 cm^{-1} and increases the area linearly. This band may also be ascribed to the Nb–O–Nb vibrations of NbO_6 octahedra shared by vertices (literature observations related a broad band at $652\text{--}659\text{ cm}^{-1}$) [92–95], which would be expected due to the linear increase of Nb_2O_5 .

The vibrational modes of metaborate chains give rise to the green band centered at 742 cm^{-1} [86,87,90]. This band shifts progressively to lower wavenumbers, and its area decreases with increasing Nb content. However, it does not disappear entirely up to Nb-PNCB:4. The band centered at 766 cm^{-1} for PNCB, represented by the pink curve, is associated with superstructural units consisting of two six-membered rings interconnected by two BO_4^- tetrahedra [51,86,87,89,90,96]. According to Konijnendijk and Stevels, the presence of a band near 760 cm^{-1} indicates a significant amount of BO_4 units within the glass network [87]. Upon Nb incorporation, this band shifts toward higher wavenumbers, reaching 770 cm^{-1} for Nb-PNCB:4. This behavior suggests a partial transformation of BO_4^- tetrahedra into BO_3 triangles [83,96]. This interpretation is supported by contrasting behavior observed in $\text{BaO-B}_2\text{O}_3$ systems, where an opposite trend was reported [83]. Additionally, the band near 774 cm^{-1} is attributed to the symmetric breathing vibrations of six-membered rings containing a single BO_4^- tetrahedron. The progressive broadening and shifting of this band toward lower frequencies with barium addition suggests the formation of six-membered rings incorporating two BO_4^- tetrahedra [83].

Moreover, the vibrational modes of diborate groups are reflected in the olive band centered at 985 cm^{-1} for PNCB [51,86]. This band exhibits a slight shift to 979 cm^{-1} for Nb-PNCB:4, while its area and width remain relatively constant. The interaction between borate and phosphate groups gives rise to B–O–P bonds, represented by the orange band centered at 943 cm^{-1} for PNCB. With increasing Nb content, this band area progressively decreases until it disappears completely at Nb-PNCB:4, which may be attributed to the

incorporation of Nb₂O₅. Concurrently, a new and intense band emerges in the 800–900 cm⁻¹ region. This blue band appears at 828 cm⁻¹ for Nb-PNCB:1 and shifts progressively to 842, 851, and 859 cm⁻¹ for Nb-PNCB:2, Nb-PNCB:3, and Nb-PNCB:4, respectively. According to Cardinal *et al.*, a broad band within the 799–853 cm⁻¹ range is characteristic of Nb–O–Nb stretching vibrations in chains of corner-sharing NbO₆ octahedra, indicating the role of Nb as a network former [94].

The purple curve at approximately 916 cm⁻¹ for PNCB, shifted to 902 cm⁻¹ for Nb-PNCB:2. In glasses with higher concentrations of Nb, this disappears once it is no longer necessary to fit the experimental curve. Although its assignment remains uncertain, this band may be related to the asymmetric stretching vibrations of "loose" BØ₄ tetrahedra, as suggested by Kamitsos and Chryssikos for the Cs₂O–B₂O₃ system [51], or it could be associated with pentaborate structural units [91]. In contrast, the band near 900 cm⁻¹ is associated with the stretching of short Nb–O bonds in isolated or distorted NbO₆ octahedra [92, 94], and it may also reflect the presence of NBOs [95]. Therefore, the reduction of the 943 cm⁻¹ band, combined with the shift of the Nb–O–Nb band from 842 cm⁻¹ toward higher wavenumbers, suggests the formation of B–O–Nb linkages [52] and an increasing presence of distorted or isolated NbO₆ units. This structural evolution indicates a trend toward a more depolymerized glass network, likely associated with the generation of NBOs.

Finally, the borate structures within the glasses exhibit significant distortion, reflected by variations in bond angles and/or B–O bond lengths within the borate groups. This distortion is primarily evidenced by subtle shifts in peak positions, along with changes in full width at half maximum (FWHM) and band area. However, this effect is not uniform across all borate species, and Raman spectroscopy does not allow for precise determination of the number of NBOs associated with borate units [87], offering instead a general picture of the structural evolution within the glass. Despite this limitation, the Raman spectra clearly demonstrate the incorporation of Nb into the glass network. This incorporation leads to a reduction in diborate structures and a weakening of vibrational modes associated with metaborate rings and chains, indicating their consumption in favor of forming a three-dimensional network primarily composed of NbO₆ octahedra. Additionally, the content of BØ₄ tetrahedra decreases, as corroborated by FTIR analysis (Figure 3.8), and it may be a possible substitution of phosphorus by Nb within the network. It is also noteworthy that,

despite the prominent Raman features associated with Nb, the glass contains only up to 2.7 mol% Nb_2O_5 , compared to approximately 60 mol% B_2O_3 (Table 2.1). This highlights that, although Nb strongly influences the glass structure, its addition ultimately leads to a less polymerized network.

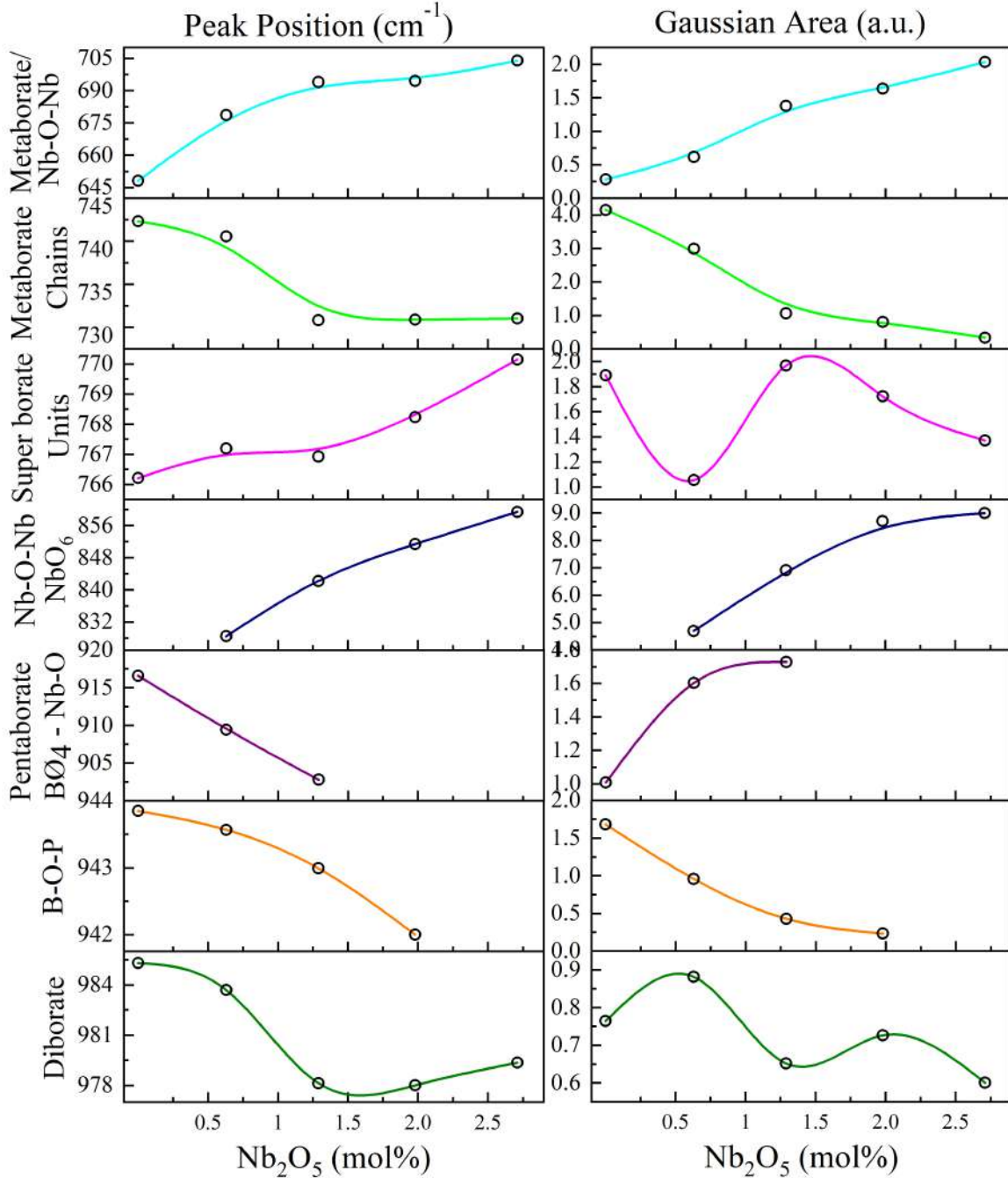


Figure 3.10: Behavior of the peak position (left) and area (right) of Gaussian fit for each vibrational band as a function of Nb_2O_5 content (mol%). The graphs are identified according to the corresponding structural units. The colors of the curves match those used in the spectral fits presented earlier in Figure 3.9.

3.10 Mechanical Properties

Hardness (H) and elastic modulus (E) of the Nb-containing glasses, determined by depth-sensing nanoindentation, are presented in Figure 3.11. The heterogeneity observed in radiopacity did not affect the mechanical properties, as the entire surface of each specimen was assessed across two independent batches.

For the same Nb content, the variation of H and E as a function of indentation load shows a linear increase behavior up to 100 mN. However, a pronounced decrease occurs at 200 mN, which is attributed to the indentation size effect. This effect is commonly linked to crack propagation beneath the indenter and the evolution of free volume within the material during the indentation process [97]. The values are summarized in Table 3.6.

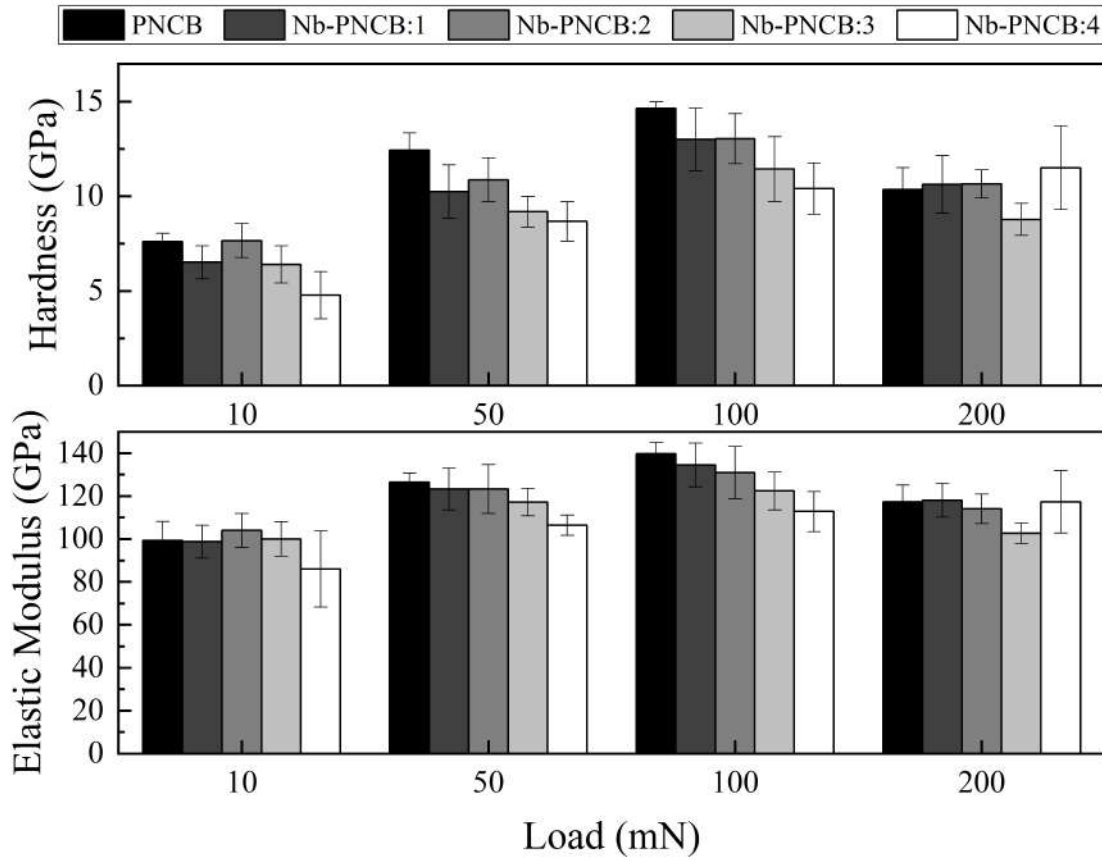


Figure 3.11: Hardness and elastic modulus of Nb-addition in PNCB glasses.

It is observed that the behavior of H and E exhibits a clear dependence on Nb content, allowing the results to be categorized in two distinct regimes based on their averages: (i) PNCB, Nb-PNCB:1, and Nb-PNCB:2; and (ii) Nb-PNCB:3 and Nb-PNCB:4, presenting anomalous behavior only at 200 mN for Nb-PNCB:4.

Table 3.6: Hardness (H) and Elastic Modulus (E) under different loads for various Nb concentrations.

	Load (mN)	PNCB	Nb-PNCB:1	Nb-PNCB:2	Nb-PNCB:3	Nb-PNCB:4
H (GPa)	10	7.6±0.4	6.5±0.9	7.7±0.9	6.4±1.0	4.8±1.2
	50	12.4±0.9	10.3±1.4	10.9±1.2	9.2±0.8	8.7±1.0
	100	14.6±0.4	13.0±1.7	13.0±1.3	11.4±1.7	10.4±1.4
	200	10.4±1.2	10.6±1.5	10.6±0.7	8.8±0.9	11.5±2.2
E (GPa)	10	99±9	99±8	104±8	100±8	86.1±1.8
	50	126±4	123±10	123±11	117±6	106±5
	100	140±5	135±10	131±12	122±9	113±9
	200	117±8	118±8	114±7	103±5	117±15

In the first group, up to Nb-PNCB:2 exhibit the highest H and E values, reaching around 11 GPa and 119 GPa across all applied loads, respectively. Notably, the Nb-PNCB:1 composition shows slightly lower H and E values compared to PNCB, whereas Nb-PNCB:2 maintains mechanical performance equivalent to the undoped glass. This behavior suggests that, within this compositional range, Nb⁵⁺ ions predominantly act as network formers, likely incorporating into the glass structure as NbO₆ octahedra. These structural units contribute to reinforcing the borate network by increasing cross-link density, thereby maintaining or enhancing the mechanical properties.

Beyond Nb-PNCB:2, a clear reduction in mechanical performance is observed. The second group, comprising Nb-PNCB:3 and Nb-PNCB:4, exhibits significant reductions in hardness (approximately 18%) and elastic modulus (around 12%) compared to the first group. This decline is attributed to a structural transition, in which Nb shifts from functioning as a network former to acting predominantly as a network modifier. At higher Nb contents, the presence of Nb₂O₅ promotes the conversion of BO₄ tetrahedra into BO₃ units and increases the formation of NBOs. This depolymerization weakens the glass network, enhances ionic mobility, and consequently reduces its rigidity and mechanical strength. A similar phenomenon was previously reported by Smedskjaer *et al.*, who observed that high Na₂O content (above 25 mol%) induces borate unit conversion, leading to comparable mechanical degradation [60].

3.11 Aqueous Interaction

Dynamic vapor sorption (DVS) was employed to assess the initial interactions of the glasses with humidity, used as an indicator of their reactivity and potential solubility. For this analysis, gravimetric sorption and desorption measurements were conducted under direct exposure to 90% relative humidity (RH) for 24 h and then to, 0% of RH for additional 24 h, totaling 48 h of experiment, as shown in Figure 3.12.

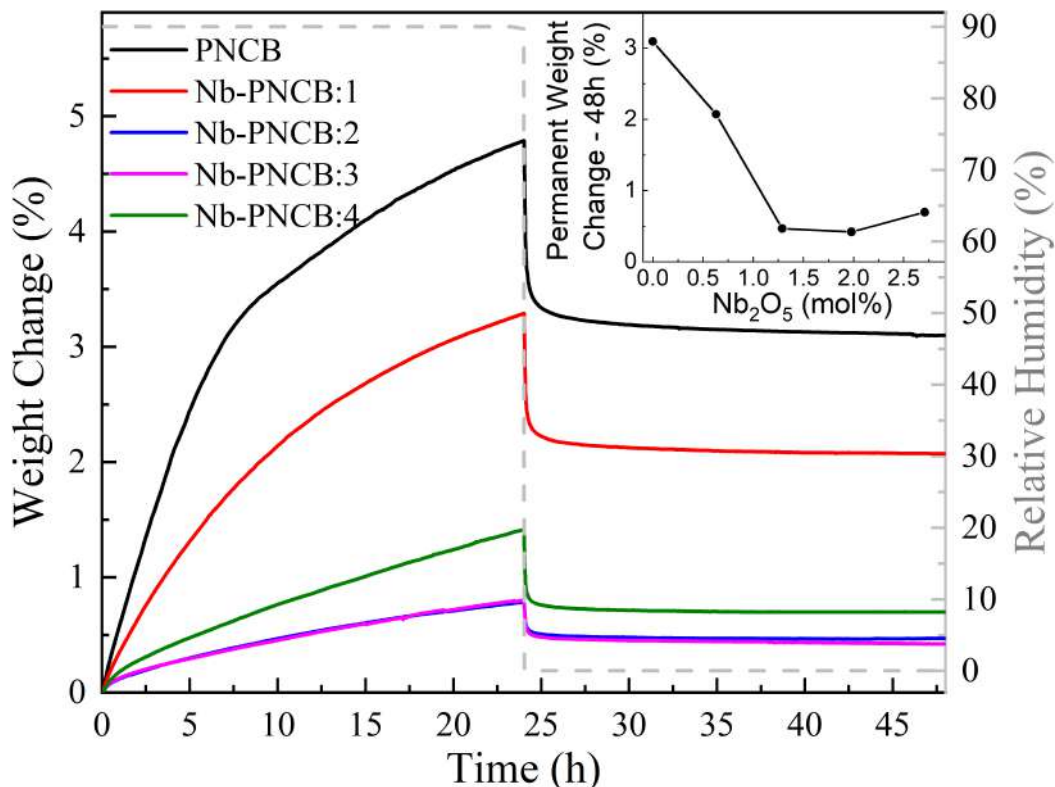


Figure 3.12: Reactivity of as-made Nb-addition in borate glasses through vapor sorption: exposure to 90% RH followed by 0% RH.

There was an immediate and pronounced increase in the weight of PNCB during the first 6 h, attributable to vapor sorption, which was followed by a slower rate of increase until 24 h, reaching approximately 5% in total. This behavior indicates relatively higher hydrophilicity and reactivity. As the Nb content increased, vapor sorption of the glasses decreased, demonstrating that both the rate and weight change depended on glass composition, and suggesting lower extents of reactivity. Nevertheless, Nb-PNCB:4 exhibited slightly higher reactivity (1.4%) compared to Nb-PNCB:2 and Nb-PNCB:3 (both at approximately 0.8%). When the RH was immediately reduced to 0%, a rapid decrease in weight was observed in all samples. After 48 h, the final weight change was higher in

glasses with no or low Nb content. Interestingly, Nb-PNCB:4 also had a higher final weight gain compared to Nb-PNCB:2 and Nb-PNCB:3, as shown in Figure 3.12 inset.

It is well established that network connectivity, along with molecular and atomic structures, critically influences reactivity and chemical durability [6,98]. In this context, the PNCB composition exhibits the highest reactivity. When Nb_2O_5 is added to the glass, Nb^{5+} ions predominantly form NbO_6 octahedra that integrate into the borate network as network formers, thereby increasing the overall cross-link density. Consequently, the glass exhibits enhanced chemical durability and reduced susceptibility to moisture-induced degradation, as demonstrated by the lower water sorption observed in the Nb-PNCB:2 and Nb-PNCB:3 samples.

However, in the case of Nb-PNCB:4, the glass network shows signs of depolymerization. ATR-FTIR spectra reveal an increase in BO_3 units alongside a decrease in BO_4 units, indicating a shift toward a less connected structure. Complementary, Raman spectroscopy highlights changes in the vibrational modes associated with Nb–O bonds, reflecting alterations in the NbO_6 environment, and borate structures. These structural changes likely lead to the formation of more NBOs, increasing the free volume and enhancing water interaction, as demonstrated by the greater residual weight gain observed in the Nb-PNCB:4 following relative humidity reduction.

3.12 Ion Release

To better understand the impact of Nb content on glass reactivity and to investigate ion release kinetics, the dissolution of boron, calcium, sodium, phosphorus, and Nb was monitored over a period of up to 72 h in deionized water (DIW) using ICP-OES, alongside measurements of the pH changes, as shown in Figure 3.13.

Initially, a significant increase in the pH of the aqueous solution was observed within the first hour of immersion, followed by a gradual rise up to 6 h, after which it remained stable until 72 h. It is well established that the hydration reaction involves the exchange of cations (such as Na^+ , Ca^{2+} , and others) with the solution, accompanied by the consumption of H^+ . In parallel, the hydrolysis reaction contributes to pH elevation through the release of OH^- ions [3, 7, 99]. These observations suggest that hydrolysis was the dominant process during the initial 6 h, after which hydration and hydrolysis proceeded

at comparable rates [7].

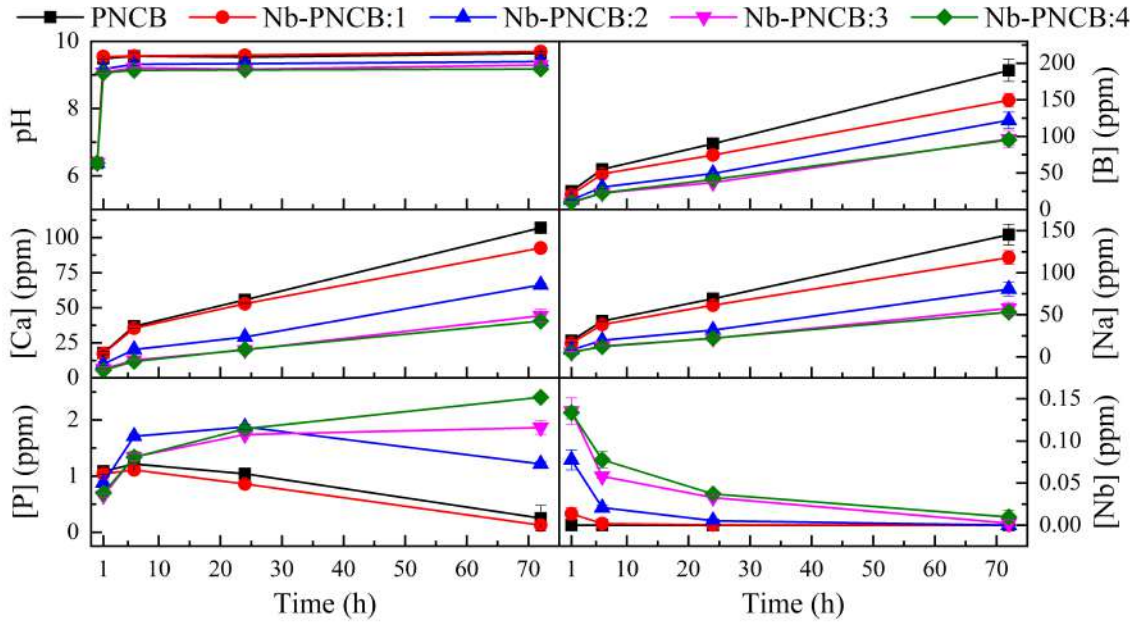


Figure 3.13: Solubility of as-made Nb-addition in borate glasses through immersion in DIW ($n=3$): pH measurements, and release of boron, calcium, sodium, phosphorous, and niobium ions as measured through ICP-OES.

The pH values of PNCB and Nb-PNCB:1 are slightly higher than those of Nb-PNCB:2, Nb-PNCB:3, and Nb-PNCB:4, decreasing from 9.5 to approximately 9. From a chemical standpoint, the modifier role of Nb at higher concentrations increases ionic mobility within the glass matrix, thereby promoting hydrolysis and ion exchange reactions at the glass-solution interface. The influence of Nb content is also reflected in the pH evolution during immersion tests, where glasses with higher Nb concentrations exhibit a less pronounced pH increase compared to those with lower Nb content. This trend is consistent with modified hydration and hydrolysis mechanisms. Similar pH behavior has been reported for Nb-doped silicate glasses [15]. For borate-based glasses containing calcium, sodium and phosphorous exhibited a significantly higher pH increase during immersion tests, reaching values around 10.5 [6].

Glasses with higher Nb content exhibited reduced overall release levels of boron, calcium, and sodium, whose release occurred progressively. In contrast, phosphorus and niobium displayed distinct release behaviors. Phosphorus showed a decreasing trend after 6 h for PNCB and Nb-PNCB:1, and after 24 h for Nb-PNCB:2. However, for Nb-PNCB:3 and Nb-PNCB:4, phosphorus release continued to increase over the entire period. Niobium exhibited a different pattern, with the highest release occurring within the first hour,

followed by a progressive decrease until it became undetectable by 72 h.

Despite the higher boron concentration in glasses with increased Nb content, this did not result in greater boron release during dissolution. It has been reported that glasses with a higher proportion of BO_4 units generally exhibit lower dissolution rates, particularly those produced via melt-quenching, as BO_4 enhances network connectivity [7, 100]. However, in binary $\text{CaO-B}_2\text{O}_3$ glasses, higher N_4 fractions have been associated with faster ion release [6], potentially due to the influence of network modifiers and interactions with other components, such as Nb [15]. More recently, Yin *et al.* demonstrated that, in calcium-borate glasses, the initial release rates of calcium and boron are primarily governed by their absolute concentrations in the material rather than the N_4 ratio [7].

As Nb was incorporated at the expense of calcium and sodium, their release profiles decreased, following the expected trend. However, phosphorus release generally decreased over time, likely due to its consumption through interactions with calcium, an effect commonly observed in bioactive glasses during the formation of a surface hydroxycarbonate apatite (HCA) layer in physiological environments, such as SBF [6, 15, 77, 101]. However, this decline in phosphorus release was not observed for the Nb-PNCB:3 and Nb-PNCB:4 compositions, suggesting that higher Nb content may interfere with the kinetics of HCA layer formation. Niobium likely affects the surface reactivity of the glass, either by altering the dissolution dynamics of phosphate ions or by inhibiting the nucleation and growth of the apatite phase [15].

The release of Nb increased proportionally with its concentration in the glasses. During the first hour, this release is primarily attributed to the leaching of Nb species near the surface and the possible dissolution of isolated NbO_6 units [19]. However, Nb can subsequently interact with phosphate and hydroxyl groups in solution, forming species such as Nb-O-P and Nb-OH [15, 19]. Additionally, the formation of calcium niobate and/or sodium niobate species has been reported [50]. As a result, the concentration of Nb-free species in solution decreases over time, potentially leading to the precipitation of a Nb-rich gel on the glass surface, which may further limit reactivity. The gradual decline in Nb concentration is mainly attributed to the progressive polymerization of Nb species in solution [15]. This behavior aligns with the pH trends and the weight changes observed through DVS analysis.

3.13 Acellular Bioactivity

3.13.1 XRD

Immersion in simulated body fluid (SBF) for up to 14 days was used to evaluate the *in vitro* bioactivity of the Nb-containing glasses. X-ray diffraction (XRD) analysis confirmed the formation of hydroxycarbonate apatite (HCA) on the surface of all compositions, evidenced by the emergence of characteristic hydroxyapatite peaks indexed to JCPDS 9-0432, particularly at $2\theta \approx 26$ and 32° [102], Figure 3.14. For the PNCB glass, the appearance of these peaks was detected within the first few days of immersion, indicating rapid surface bioactivity. With extended immersion, the peaks became sharper and more intense, suggesting progressive growth and crystallization of the HCA layer.

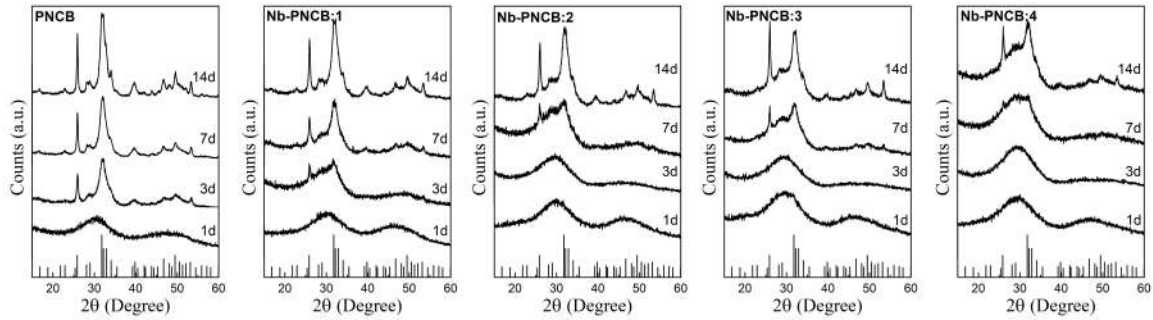


Figure 3.14: XRD diffractograms of acellular bioactivity assay in SBF after 1, 3, 7, and 14 days. The indexed phase corresponds to Hydroxyapatite JCPDS 9-0432.

In contrast, the incorporation of Nb noticeably affected the kinetics of HCA formation. As the Nb content increased, the formation of HCA occurred at slower rates, as evidenced by broader and less intense diffraction peaks, which are characteristic of poorly crystalline or nanocrystalline apatite, as well as partially amorphous phases [77, 102]. Specifically, HCA formation was detected around day 3 for the Nb-PNCB:1 glass, day 7 for the Nb-PNCB:2 and Nb-PNCB:3 compositions, and only between days 7 and 14 for the Nb-PNCB:4.

This retardation in HCA formation with increasing Nb content may be attributed to several factors related to the structural role of Nb within the glass network. Niobium, acting primarily as a network former through NbO_6 octahedra, increases the cross-link density of the glass, reducing its dissolution rate and subsequently delaying the release of critical ionic species such as Ca^{2+} and PO_4^{3-} , which are necessary for apatite nucleation. Furthermore, Nb may directly interact with phosphate species in solution or at the

glass–solution interface, forming Nb–O–P linkages or Nb-rich surface layers that could act as physical or chemical barriers to apatite nucleation and growth.

Despite the delayed onset, all Nb-containing glasses eventually demonstrated bioactivity through HCA formation, confirming that the incorporation of Nb does not suppress bioactivity, but rather modulates the kinetics of surface mineralization. This behavior aligns with previous studies on Nb-doped bioactive silicate glasses, which report similar trends of reduced dissolution rates and delayed apatite formation [15].

3.13.2 ATR-FTIR

ATR-FTIR spectra of the glasses immersed in SBF over time provided clear molecular evidence of the surface conversion process, confirming the XRD results about the formation of the hydroxycarbonate apatite (HCA) layer, indicated in Figure 3.15. This conversion was marked by the progressive appearance and intensification of characteristic vibrational bands associated with phosphate and carbonate groups, which are signatures of the apatite structure. Specifically, the spectra exhibited the ν_3 asymmetric stretching mode of phosphate (PO_4^{3-}) centered around 1020 cm^{-1} , accompanied by a shoulder at approximately 961 cm^{-1} attributed to the ν_1 symmetric stretching of phosphate. The presence of the ν_4 phosphate bending modes between 550 and 600 cm^{-1} , particularly the splitting of these bands, is indicative of increasing crystallinity in the apatite layer [103, 104].

Additionally, the broad band around 1640 cm^{-1} was associated with O–H bending vibrations, reflecting both structural hydroxyl groups within the HCA lattice and adsorbed water from the immersion medium. The progressive formation of a carbonated apatite phase was evidenced by the emergence of the ν_3 asymmetric stretching bands of CO_3^{2-} at 1420 and 1457 cm^{-1} . These carbonate groups can substitute for OH^- (Type A substitution) or PO_4^{3-} (Type B substitution) sites within the hydroxyapatite lattice, resulting in the formation of HCA, a feature that closely mimics biological bone mineral [6, 11].

Temporal analysis of the spectra demonstrated that all compositions initially formed an amorphous CaP-rich layer within the first 24 h of immersion. However, the rate of subsequent crystallization into a well-ordered HCA phase was significantly influenced by the Nb_2O_5 content. For the Nb-free glass, the transformation into crystalline HCA occurred rapidly, with clear phosphate band splitting observable by day 3. The Nb-PNCB:1

exhibited a moderately delayed crystallization, with the crystalline features becoming evident around day 7. In contrast, glasses with higher Nb content (Nb-PNCB:2, Nb-PNCB:3, and Nb-PNCB:4) showed markedly slower conversion, with crystallization signatures only emerging by day 14. Even at this stage, the bands remained broader, suggesting incomplete crystallization.

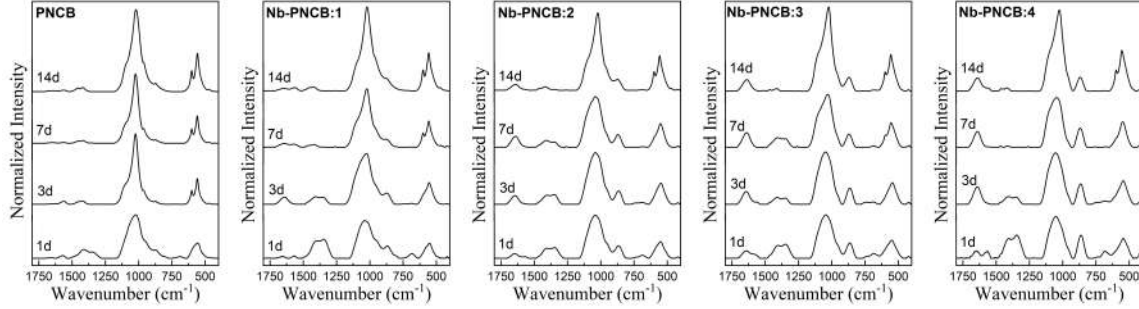


Figure 3.15: ATR-FTIR spectra of acellular bioactivity assay in SBF after 1, 3, 7, and 14 days.

This progressive slowdown in HCA formation with increasing Nb₂O₅ content aligns with prior observations in Nb-doped silicate glasses, which similarly exhibited reduced bioactivity and slower *in vitro* mineralization rates [15]. This behavior is primarily attributed to the chemical role of Nb within the glass network. Nb⁵⁺, predominantly in the form of NbO₆ octahedra, acts as a network former, enhancing network connectivity. This increased connectivity reduces the rate of hydrolysis and ionic dissolution, particularly of key species like Ca²⁺ and PO₄³⁻ that are essential for apatite nucleation.

Moreover, it is suggested that the formation of a hydrated Nb-rich surface layer, primarily Nb–OH or Nb–O–P species, passivates the glass surface, further inhibiting ion release necessary for HCA formation [15, 19]. This is consistent with the ion release profiles observed in DIW, where Nb-PNCB:3 and Nb-PNCB:4 compositions showed minimal phosphorus consumption within the early days, implying suppressed phosphate precipitation or delayed nucleation kinetics.

Additionally, in some silicate glass compositions, ion release is delayed due to the formation of an SiO₂-rich layer [3, 78, 105]. However, borate glasses do not form this type of silica gel layer due to the inherently higher solubility of borate species and the absence of a stable B₂O₃-rich surface phase. Consequently, HCA formation in borate glasses occurs directly on the external surface via a dissolution–precipitation mechanism, progressing from the surface toward the interior of the glass particle. This leads to a

shrinking core model of conversion, wherein the outer glass continuously reacts until it is entirely transformed, causing a reduction in particle volume.

This process is driven by the rapid leaching of highly soluble species such as BO_3^{3-} and Na^+ , while less soluble ions like Ca^{2+} and PO_4^{3-} accumulate at the glass-solution interface to nucleate and grow the amorphous calcium phosphate layer. Over time, this layer crystallizes in HCA, as reflected in the ATR-FTIR and XRD results. The presence of Nb modifies this process by stabilizing the glass network and reducing the availability of key ions, thereby slowing the formation and maturation of the HCA layer, probably due to the formation of a Nb-rich layer.

In summary, ATR-FTIR analysis reveals a clear correlation between Nb content and the kinetics of HCA formation, underscoring the trade-off between improved chemical durability and reduced bioactivity as Nb_2O_5 content increases. This highlights the critical need to balance structural stability with biological performance in the design of Nb-containing bioactive glasses.

3.14 Cellular Assays

Figure 3.16 displays a matrix of fluorescence micrographs capturing the behavior of huAD-MSCs cultured for up to 10 days under four conditions: culture medium only (control) and media containing ionic dissolution products from PNCB, Nb-PNCB:1, and Nb-PNCB:4 glasses. Cells were stained with fluorescent markers to differentiate cellular components: the actin cytoskeleton appears green, nuclei are stained blue with DAPI, and dead cells are highlighted in red (DNA stain), enabling visualization of cell morphology, density¹, and viability² over time, respectively.

Across all experimental conditions, a consistent increase in cell density was observed from day 1 to day 10, reflecting cell proliferation. Remarkably, the Nb-PNCB:4 group exhibited particularly high confluence³ by day 10, suggesting a strong capacity to support cell growth. Additionally, no notable differences in cell morphology were detected between groups. Cells maintained the characteristic elongated, spindle-like morphology typical of MSCs, with no evidence of abnormal shapes or stress-related morphological

¹**Cell density** is the number of cells per unit of volume or area.

²**Cell viability** refers to the proportion of live cells in a sample.

³**Confluence** is the percentage of the surface of a flask or culture plate that is covered by adherent cells.

changes. The presence of dead cells was minimal in all conditions, further supporting the cytocompatibility of the ionic products derived from the glasses.

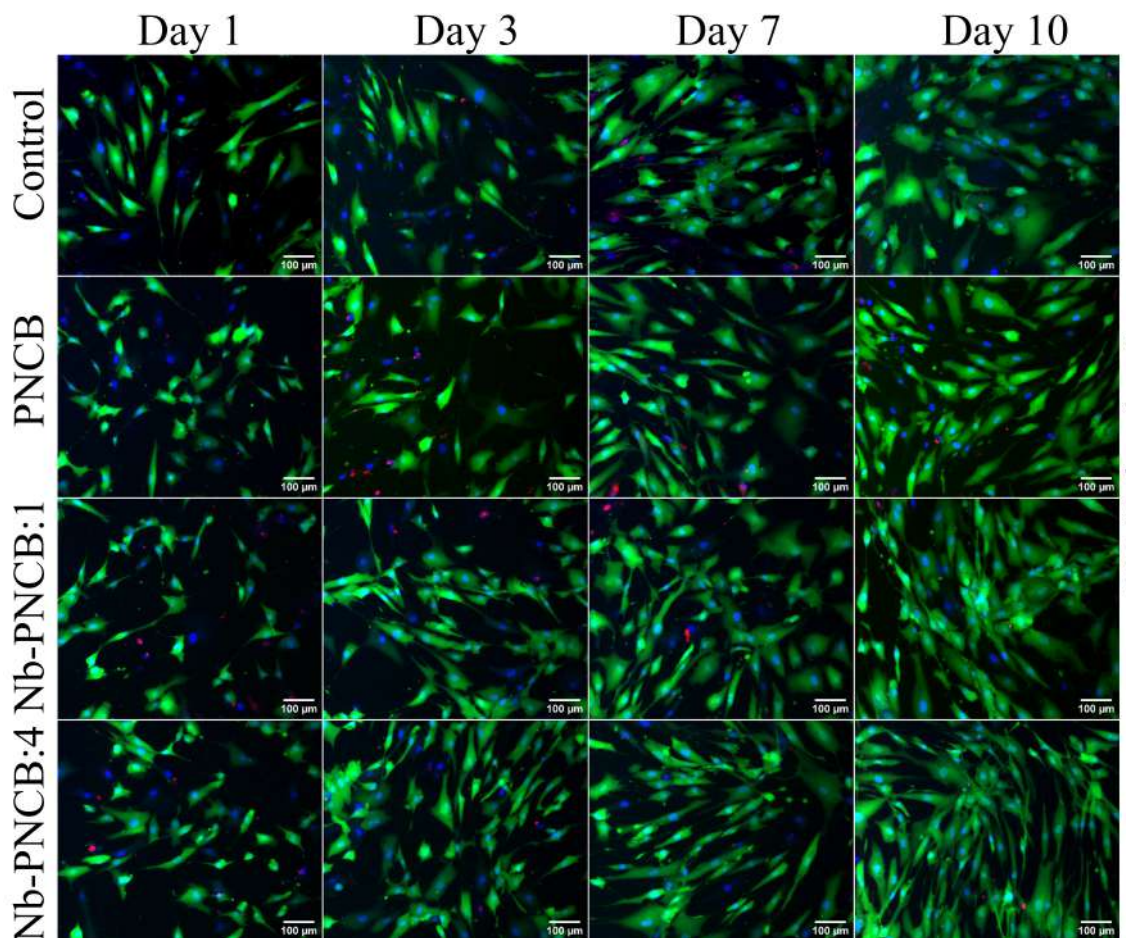


Figure 3.16: Cellular Assays: Calcein-AM labeled live huAD-MSC (green), Hoechst 33342 (blue) stained dsDNA and Ethidium Homodimer-1 binding dead nuclei (red) at days 1, 3, 7 and 10, scale bar = 100 μm .

Quantification was carried out using fluorescence-based live/deadTM assays. Figure 3.17 presents the cell viability expressed as a percentage and calculated from live and dead cells, which corresponds to the total number of cells. Basically, live and dead cells are the total and viability is expressed based on the relation between live cells and the total. The results were also obtained over 10 days of culture, in the same conditions of microscopy analysis.

It can be observed that, in all groups, cell viability remained high, reaching almost 100%, throughout the entire period, indicating excellent cytocompatibility. However, statistically significant differences were detected between groups. On day 1, the control group showed slightly lower viability compared to Nb-PNCB:1 ($p < 0.01$). This trend persisted on days 3 and 7, when Nb-PNCB:1 and Nb-PNCB:4 showed significantly higher

viabilities compared to the control ($p<0.05$ and $p<0.01$, respectively). Finally, on day 10, this difference became more pronounced, where all groups present higher viability than control, exhibiting a highlight to Nb-PNCB:4 ($p<0.001$).

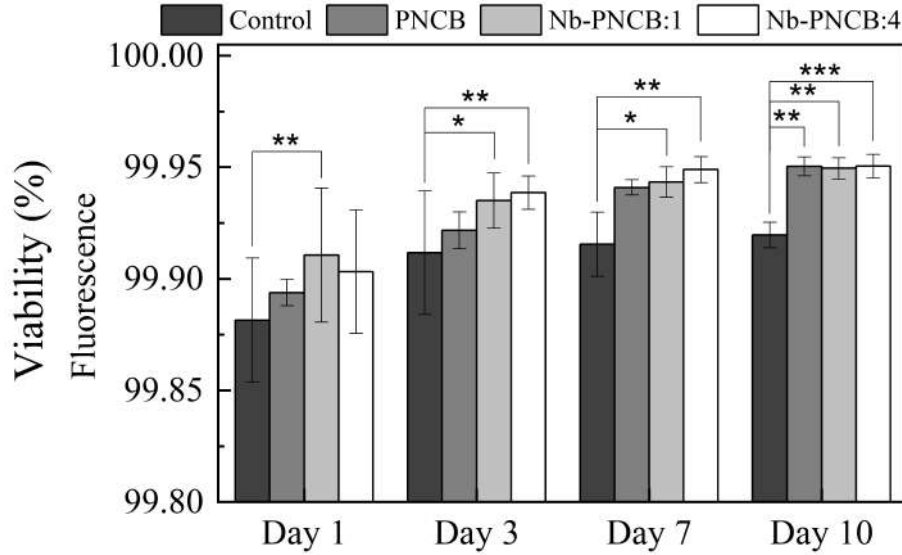


Figure 3.17: Cellular Viability based on luminescence of Calcein-AM labeled live and Ethidium Homodimer-1 binding dead nuclei at days 1, 3, 7, and 10.

These results, together with the fluorescence micrographs, confirm that the ionic products from the Nb-containing glasses not only maintain, but may even enhance cell viability over time.

WST⁻¹ metabolic assay further supported these data, as exhibited in Figure 3.18, which evaluates cell viability based on mitochondrial activity. The assay revealed a progressive increase in optical density over time across all groups, indicating an enhancement in cellular metabolic activity as the culture progressed. Up to day 7, no statistically significant differences were observed between any of the treated groups and the control, suggesting that the ionic dissolution products did not negatively impact metabolic function. However, by day 10, a significant increase in metabolic activity was detected in the Nb-PNCB:4 group when compared to PNCB ($p<0.05$) and Nb-PNCB:1 ($p<0.01$), although this difference was not statistically significant when compared to the control. Conversely, the PNCB and Nb-PNCB:1 groups did not show significant differences relative to the control group. This means, higher Nb content increase the cell metabolic activity compared to lower contents.

The pH of the culture medium is widely recognized as a critical factor in regulating cell viability and proliferation [106–108]. The DVS analysis (previously discussed - Figure

3.12) demonstrated that the PNCB glass exhibited higher reactivity than Nb-PNCB:1 and Nb-PNCB:4, which directly influenced their ionic release profiles (Figure 3.13). A lower ion release rate is associated with more stable pH levels, maintaining values closer to physiological conditions. Despite these differences in reactivity, the results clearly indicate that the incorporation of Nb into the borate glass did not induce any cytotoxic effects. On the contrary, the presence of Nb appeared to support and even enhance cell proliferation when cells were exposed to the ionic dissolution products.

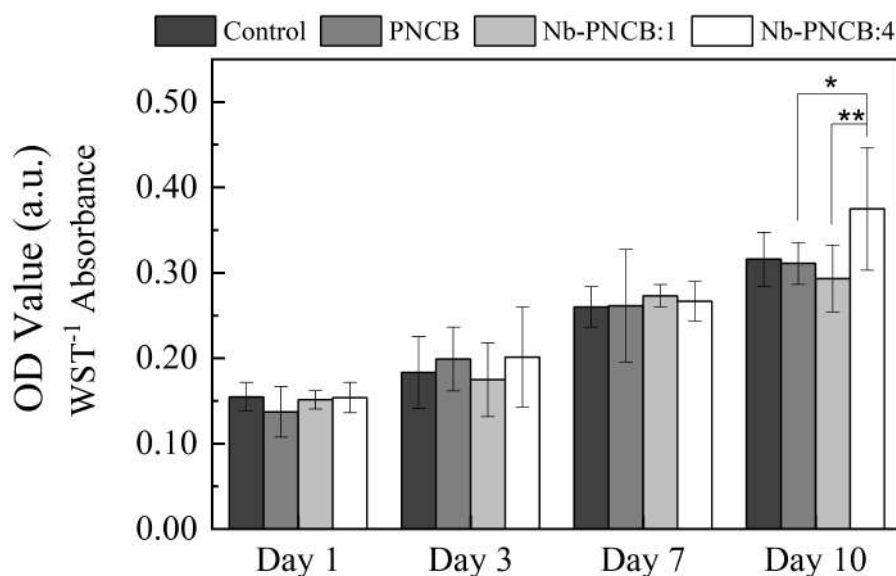


Figure 3.18: Cell metabolic activity assessed by absorbance. All experiments were treated with culture supplemented with ionic dissolution products of Nb-Glasses at a concentration of 1.5 mg/mL.

Similar trends have been reported in previous studies. For instance, Souza *et al.* investigated silicate glasses doped with up to 2.7 mol% Nb₂O₅ and reported no cytotoxicity, although cell proliferation was not significantly enhanced in human embryonic stem cells based on metabolic assays [50]. In contrast, Míguez-Pacheco *et al.* [1] observed improved proliferation of bone marrow-derived stromal cells exposed to ionic extracts of silicate glasses containing up to 1 mol% Nb₂O₅, with the strongest effect observed at intermediate dilution levels (0.1 mg/mL).

In phosphate-based glasses, the incorporation of Nb has been shown to substantially reduce ion release rates and mitigate the acidification commonly associated with phosphate glass dissolution. This adjustment led to improved cell proliferation even in compositions containing up to 30 mol% Nb₂O₅ [109]. Similarly, calcium phosphate invert glasses doped with up to 10 mol% Nb₂O₅ demonstrated excellent cytocompatibility, enhanced alkaline

phosphatase (ALP) activity, and increased calcium deposition, particularly in compositions containing 3 and 5 mol% Nb₂O₅, even in the absence of osteogenic supplements [5].

Moreover, Lopes *et al.* evaluated the biological response of bone marrow-derived mesenchymal stem cells (MSCs) exposed to conditioned media from 45S5-based silicate glasses doped with up to 5 mol% Nb₂O₅. Their findings revealed no cytotoxicity, with the 1 mol% Nb₂O₅ composition promoting the highest levels of cell proliferation. Notably, the 1 and 2.5 mol% compositions also induced osteogenic differentiation, as evidenced by mineralized nodule formation and osteocalcin expression. These observations suggest that the dissolution products from these compositions can promote osteoblastic maturation even in the absence of osteogenic chemical signals. Furthermore, *in vivo* experiments confirmed the osteoconductive potential of the 1 mol% Nb₂O₅ glass, which supported bone formation around implants placed in rat tibiae [19].

Taken together, these results provide strong evidence that the incorporation of Nb into borate glass compositions enhances cytocompatibility and supports cell proliferation in a manner consistent with the literature on other Nb-containing bioactive glasses. The ionic concentration used in this study appears to be within an effective and safe range for stimulating cellular activity. However, further investigations are warranted to assess whether these materials also promote osteogenic differentiation and mineralization. Future studies should aim to elucidate the molecular mechanisms underlying the biological effects of Nb ions, which remain not fully understood [3, 5, 19].

3.15 Blood Coagulation

3.15.1 Storage Modulus

The storage modulus (G') is a rheological parameter that represents the elastic, or solid-like, behavior of a material. In the context of blood coagulation, an increase in G' over time indicates the transformation of blood from a liquid to a viscoelastic gel as the fibrin network forms during clotting. Monitoring G' provides a sensitive and quantitative measure of the kinetics and strength of clot formation.

Figure 3.19 shows the G' curves related to clot formation in citrated blood⁴ exposed to

⁴Sodium citrate acts by chelating calcium ions (Ca²⁺), which are essential for blood coagulation. By temporarily removing free calcium, citrate prevents the blood from clotting, allowing it to be used for analyses.

different concentrations of ionic dissolution products (Figure 3.19a) and particles (Figure 3.19b) from PNCB and Nb-PNCB:4. The curves illustrate how the presence of these materials affects the onset, rate, and final stiffness of the clot, reflecting their potential impact on coagulation behavior.

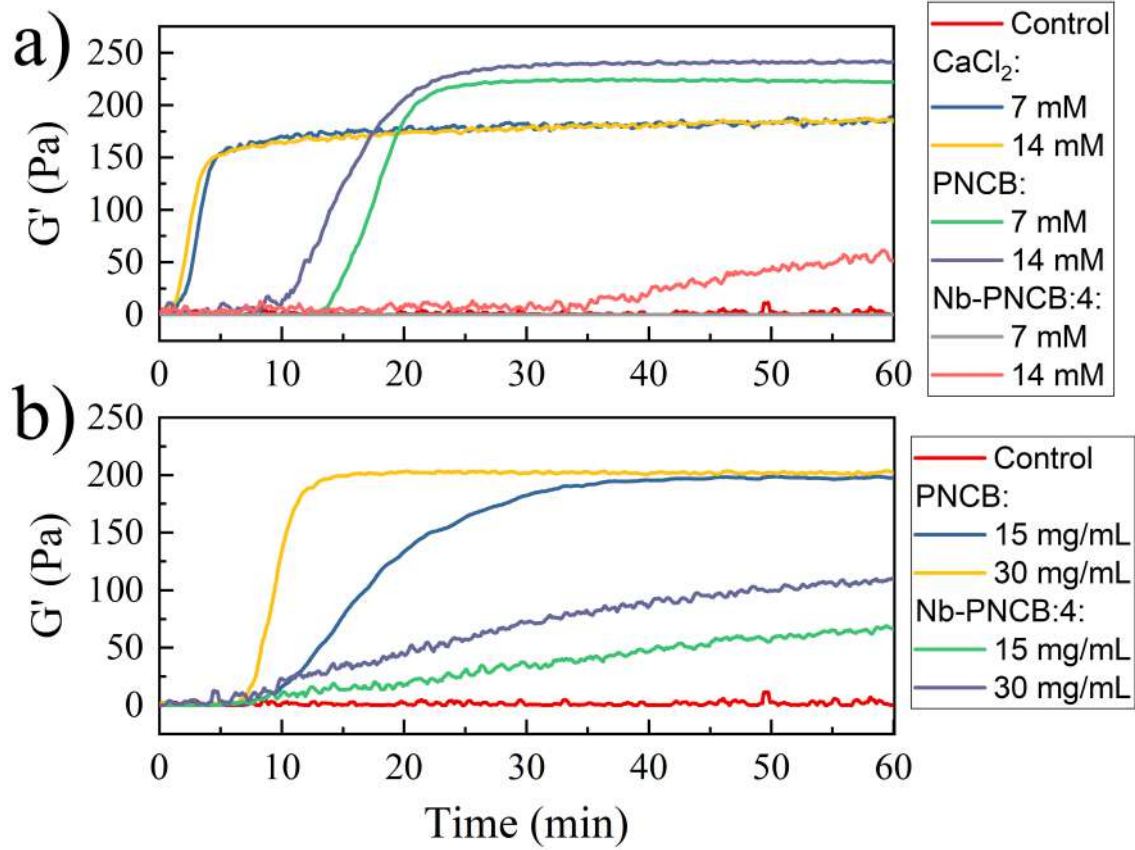


Figure 3.19: Clotting profiles: G' versus time curves of citrated blood mixed with (a) ionic dissolution products of PNCB and Nb-PNCB:4 glasses and (b) their particles.

The negative control, Figure 3.19, showed no evidence of clot formation, with the G' remaining at 0 Pa throughout the entire analysis period. In contrast, the positive controls containing 7 and 14 mM of CaCl₂ exhibited similar clotting behaviors. Clot initiation occurred at 1.19 ± 0.09 min and 1.1 ± 0.2 min, with stabilization reached at 4.4 ± 0.1 min and 3.83 ± 0.07 min, respectively. After 60 min, both conditions achieved comparable final G' values of 178 ± 3 Pa and 179 ± 3 Pa.

For the PNCB dissolution products, a delayed onset of clot formation was observed compared to the controls, with initiation times of 13 ± 2 min at 7 mM and 10 ± 1 min at 14 mM. Stabilization occurred at 22 ± 2 min and 20.4 ± 0.4 min, respectively. Notably, despite the delayed clotting, both conditions resulted in higher final G' values of 223 ± 3 Pa (7

mM) and 236 ± 5 Pa (14 mM), indicating stronger clot structures.

In contrast, the Nb-PNCB:4 dissolution products demonstrated a markedly reduced ability to induce clot formation. At 7 mM, no clot formation was detected within the analysis time. At 14 mM, clotting was initiated only after a considerable delay of 36 ± 2 min, and only a weak clot was formed.

Similar trends were observed when whole blood was directly exposed to the glass particles, Figure 3.19b. Higher particle concentration (30 mg/mL) generally enhanced clot formation compared to 15 mg/mL. For PNCB, clot initiation occurred at 8 ± 4 min for 15 mg/mL, with stabilization at 29 ± 4 min and a final G' of 199 ± 8 Pa. Increasing the concentration to 30 mg/mL accelerated clot initiation to 5.8 ± 0.7 min and stabilization to 12 ± 1 min, with a final G' of 200 ± 2 Pa.

For Nb-PNCB:4 particles, clot initiation was observed at 7 ± 2 min for 15 mg/mL and 4.5 ± 0.8 min for 30 mg/mL. However, no stabilization of the G' curve was observed within 60 min for either concentration, suggesting incomplete or unstable clot formation. A summary of all rheological parameters is provided in Table 3.7.

Table 3.7: Clot initiation time, clot stabilization time, and final storage modulus (G') values obtained when citrated blood was exposed to ionic release (CaCl_2 , PNCB, Nb-PNCB:4) or particles (PNCB, Nb-PNCB:4).

	Condition	Clot Initiation Time (min)	Clot Stabilization Time (min)	G' Stabilized (Pa)
Ion Release				
CaCl_2	7 mM	1.19 ± 0.09	4.4 ± 0.1	178 ± 3
	14 mM	1.1 ± 0.2	3.83 ± 0.07	179 ± 3
PNCB	7 mM	13 ± 2	22 ± 2	223 ± 3
	14 mM	10 ± 1	20.4 ± 0.4	236 ± 5
Nb-PNCB:4	7 mM	—	—	—
	14 mM	36 ± 2	—	—
Particles				
PNCB	15 mg/mL	8 ± 4	29 ± 4	199 ± 8
	30 mg/mL	5.8 ± 0.7	12 ± 1	200 ± 2
Nb-PNCB:4	15 mg/mL	7 ± 2	—	—
	30 mg/mL	4.5 ± 0.8	—	—

Photographic images of ionic dissolution products are exhibited in Figure 3.20, further corroborate the rheological data. The negative control remained a homogeneous fluid with no visible signs of coagulation. In contrast, the positive control with CaCl_2 exhibited the formation of a well-defined, stable clot. Samples treated with PNCB showed substantial clot formation, characterized by dense fibrin networks and minimal residual fluid, particularly at 14 mM, where blood flow was markedly reduced. Conversely, Nb-PNCB:4 demonstrated limited clot formation, with no visible clot at 7 mM and a highly fluid appearance at 14 mM, indicating impaired fibrinogen-to-fibrin conversion and reduced coagulation capacity.

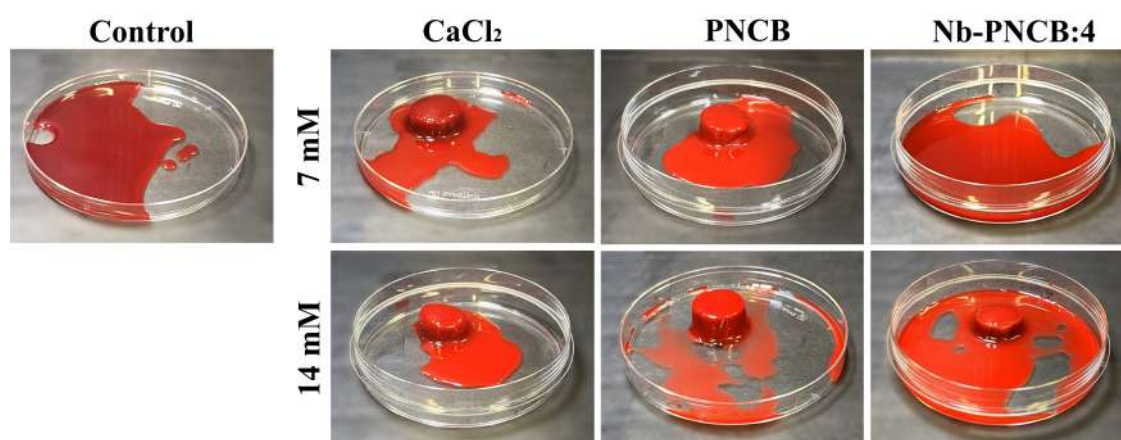


Figure 3.20: Photographic images of citrated blood at the end of tests mixed with ionic dissolution products of PNCB and Nb-PNCB:4 glasses to get 7 and 14 mM.

A similar pattern was observed with glass particles, as shown in Figure 3.21. Clot formation in the presence of PNCB particles resulted in more compact, cohesive, and well-structured clots compared to those formed with Nb-PNCB:4. This was clearly evident in both top and bottom views of the samples. From the bottom view, where the glass particles tend to settle, the clots with PNCB appeared denser and more interconnected, suggesting effective fibrin polymerization. In contrast, samples containing Nb-PNCB:4 displayed loose, fragile, and poorly organized clot structures, with large areas of residual fluid and less visible integration of particles into the clot network. This observation reinforces the rheological findings, indicating that Nb-PNCB:4 has a diminished capacity to support coagulation.

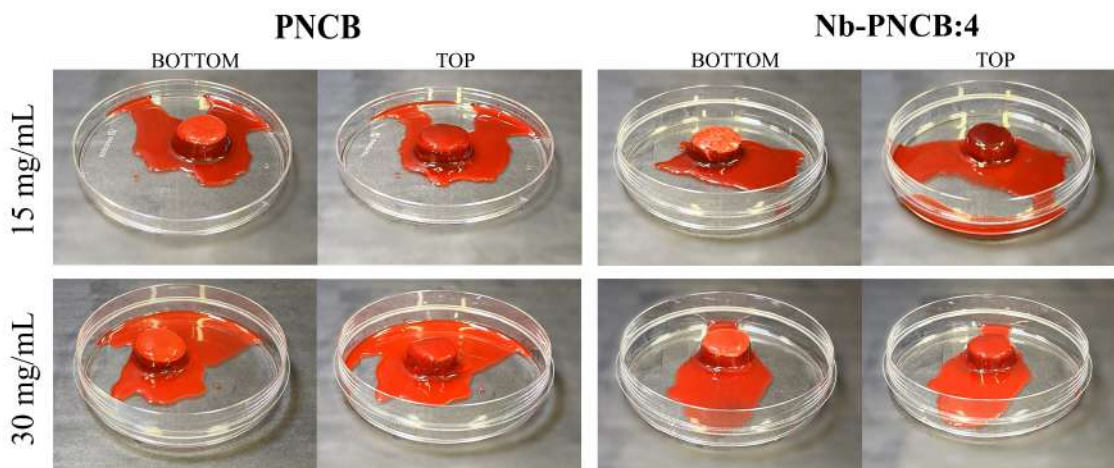


Figure 3.21: Photographic images of citrated blood at the end of tests mixed with glass particles at 15 and 30 mg/mL.

Blood coagulation, or hemostasis, is a tightly regulated process comprising three main stages: vasoconstriction, formation of the platelet plug, and the coagulation cascade. The latter involves a complex enzymatic sequence in which plasma proteins (clotting factors) are activated stepwise, ultimately leading to the conversion of fibrinogen into fibrin, forming a stable clot. Calcium ions (Ca^{2+}) are indispensable in this process, serving as essential cofactors for the activation of clotting factors II (prothrombin), VII, IX, and X, and for the assembly of the tenase and prothrombinase complexes, which drive thrombin generation [70,110,111]. While sodium ions (Na^+) do not directly participate in the enzymatic steps of the cascade, they are critical for maintaining osmotic balance and supporting platelet function [111]. Additionally, other ions such as potassium and zinc are being increasingly recognized for their modulatory roles in coagulation and platelet physiology [112]. Thus, the coagulation process depends not only on the interplay of proteins and cells but also on a finely balanced ionic environment to proceed efficiently [8,110,111].

Although CaCl_2 induced a faster coagulation response, the PNCB achieved a higher G' values, indicating a more elastic and mechanically stable clot, potentially influenced not only by the released calcium but also by the contribution of other ions present in the composition. A clear dose-dependent effect was observed, where increasing the concentration of either ionic dissolution products or particles led to higher G' values, reflecting stronger clot formation. However, the presence of niobium in Nb-PNCB:4 significantly impaired the clotting process. This impairment may be attributed to the lower calcium

content and reduced calcium release (as shown in Table 2.1 and Figure 3.13) or potentially to the formation of niobate complexes, which could interfere with the coagulation cascade, as previously discussed. Therefore, both the ionic dissolution profile and the physicochemical interactions at the particle surface are key factors influencing the blood response.

In this context, the evolution of the storage modulus (G') serves as a rheological marker of clot formation. Higher G' values and steeper increases in G' are associated with the polymerization and stabilization of the fibrin network, signaling the transition from a liquid to a gel-like state.

These observations are consistent with previous reports. Naseri *et al.* [110] demonstrated a similar dose-dependent response for CaCl_2 , highlighting the sensitivity of clot formation to calcium levels. Likewise, Rezabeigi *et al.* [70] validated the effectiveness of rheological assessment for characterizing different hemostatic materials, showing that their performance depends on material-specific mechanisms. The results of this study further support the concept that the hemostatic response can be modulated by tailoring the composition of bioactive glasses, controlling ion release kinetics, and adjusting particle concentration according to the clinical need. This tunability underscores the potential of bioactive borate glasses as versatile local hemostatic agents, particularly in applications requiring rapid hemorrhage control, such as surgical procedures or trauma care, as also emphasized by Pourshahrestani *et al.* [111].

3.15.2 Turbidity

Another technique that can be employed to monitor clot formation is turbidity measurement. This method assesses changes in sample opacity over time. Figure 3.22 presents the turbidity curves, expressed in FTU (Formazin Turbidity Unit), for citrated blood exposed to different concentrations of ionic dissolution products derived from PNCB and Nb-PNCB:4 (Figure 3.22a) and their particles (Figure 3.22b).

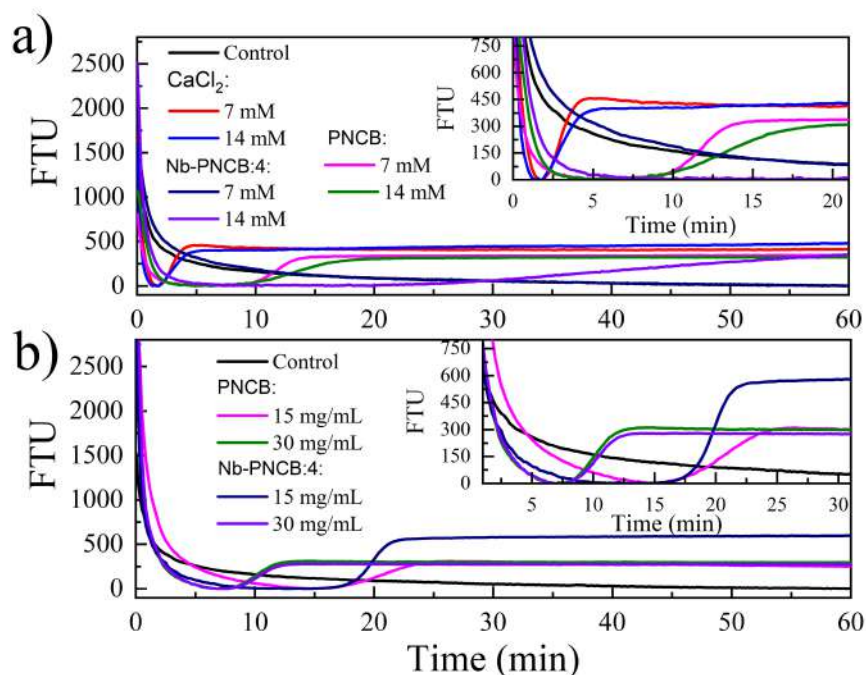


Figure 3.22: Turbidity profiles: FTU vs. time curves of citrated blood mixed with (a) ionic dissolution products and (b) glass particles of Nb-Glasses.

An initial decrease in FTU was observed, which may be attributed to the sedimentation of blood components, similarly to what occurs with glass particles. The clotting initiation time was defined as the point at which the turbidity curve begins to rise, while the stabilization time corresponds to the point at which the curve reaches a steady-state plateau.

The negative control, Figure 3.22, showed no evidence of clot formation, with FTU values remaining at zero throughout the entire analysis period. In contrast, the positive controls containing 7 mM and 14 mM CaCl_2 exhibited similar clotting behavior. Clot initiation occurred at 1.7 ± 0.2 and 1.6 ± 0.2 min, with stabilization reached at 3.8 ± 0.6 min and 3.9 ± 0.2 min, respectively. After 60 min, both conditions reached comparable final FTU values of 391 ± 81 and 387 ± 110 .

For the PNCB ionic dissolution products, a delayed onset of clot formation was observed compared to the CaCl_2 controls, with initiation times of 10.3 ± 0.8 min at 7 mM and 11 ± 1 min at 14 mM. Clot stabilization occurred at 14.2 ± 0.9 min and 18 ± 2 min, respectively. Despite the delayed clotting kinetics, both concentrations achieved final FTU values (345 ± 11 for 7 mM and 326 ± 9 for 14 mM) comparable to those of the positive control group.

In contrast, the Nb-PNCB:4 dissolution products exhibited a markedly diminished

capacity to induce clot formation. At 7 mM, no clot formation was detected throughout the analysis period. At 14 mM, clot initiation occurred only after a substantial delay of 26 min, with no stabilization observed within the monitored timeframe.

Figure 3.22b shows the results for blood directly exposed to glass particles. Overall, higher particle concentration (30 mg/mL) promoted faster clot formation compared to 15 mg/mL. For PNCB, clot initiation occurred at 15.4 ± 0.7 min for 15 mg/mL, with stabilization at 27 ± 3 min and a final FTU of 268 ± 64 . Increasing the concentration to 30 mg/mL significantly accelerated clot initiation to 10 ± 4 min and stabilization to 15 ± 5 min, accompanied by a higher final FTU of 354 ± 87 .

For Nb-PNCB:4, clot formation was also influenced by particle concentration. At 15 mg/mL, clot initiation occurred at 19 ± 2 min, with stabilization at 23 ± 2 min and a notably high final FTU of 617 ± 37 . Increasing the concentration to 30 mg/mL accelerated clot initiation to 12 ± 6 min and stabilization to 17 ± 6 min, while the final FTU decreased to 390 ± 119 . A summary of all parameters extracted from the curves is provided in Table 3.8.

Table 3.8: FTU initiation time, FTU stabilization time, and final FTU obtained when citrated blood was exposed to ionic release (CaCl_2 , PNCB, Nb-PNCB:4) or particles (PNCB, Nb-PNCB:4).

	Condition	FTU Initiation Time (min)	FTU Stabilization Time (min)	Final FTU
Ion Release				
CaCl_2	7 mM	1.7 ± 0.2	3.8 ± 0.6	391 ± 81
	14 mM	1.6 ± 0.2	3.9 ± 0.2	387 ± 110
PNCB	7 mM	10.3 ± 0.8	14.2 ± 0.9	345 ± 11
	14 mM	11 ± 1	18 ± 2	326 ± 9
Nb-PNCB:4	7 mM	–	–	–
	14 mM	26	–	–
Particles				
PNCB	15 mg/mL	15.4 ± 0.7	27 ± 3	268 ± 64
	30 mg/mL	10 ± 4	15 ± 5	354 ± 87
Nb-PNCB:4	15 mg/mL	19 ± 2	23 ± 2	617 ± 37
	30 mg/mL	12 ± 6	17 ± 6	390 ± 119

Although the methodology employed is not directly comparable to rheological data, some similarities can be observed, particularly about the effects of ionic release. This observation suggests that, despite turbidity not being the most conventional or precise method for assessing coagulation, it can still offer a reasonable estimation of the clotting process. Therefore, it serves as a complementary approach to evaluate the influence of ionic dissolution products and particles on blood coagulation dynamics.

It is important to emphasize that this analysis can be influenced by sample coloration due to light scattering. During the coagulation process, a gradual change in blood color is observed: initially, it appears bright red (due to the presence of oxyhemoglobin), but as coagulation progresses, biochemical and structural changes, such as fibrin network formation and clot retraction, leading to a darkening of the sample. In some cases, brownish tones may appear, attributed to hemoglobin oxidation (methemoglobin formation) [113, 114]. These chromatic changes directly affect light scattering and, consequently, impact turbidity readings in FTU units.

Photographic images of the turbidity assay are presented in Figure 3.23. The negative control remained a clear and homogeneous fluid throughout the test, with no signs of turbidity, confirming the absence of clot formation. However, the positive control with CaCl_2 exhibited marked turbidity for 7 and 14 mM, well as PNCB in the same concentrations.

Conversely, the Nb-PNCB:4 dissolution product exhibited altered turbidity changes. At 7 mM, the sample remained almost transparent, with partial clot formation. For 14 mM, the solution retained a translucent appearance, but it appears to have formed a clot.

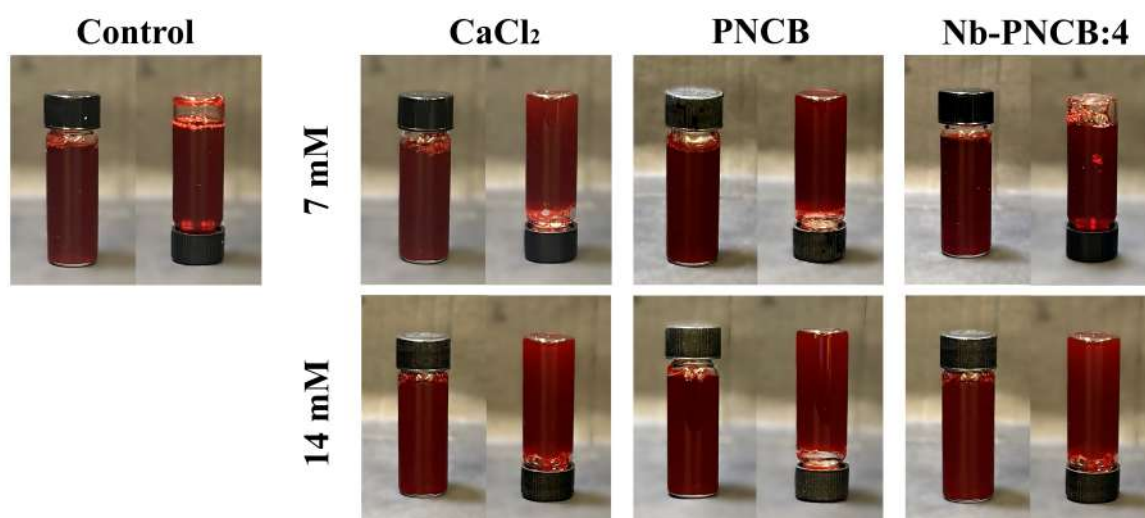


Figure 3.23: Photographic images of citrated blood at the end of Turbidity tests mixed with ionic dissolution products of Nb-Glasses to get 7 and 14 mM, based on ICP-OES.

A similar pattern was observed in the turbidity profiles for the glass particles (Figure 3.21). Vials containing PNCB particles demonstrated a clear increase in turbidity, especially at the higher concentration (30 mg/mL), indicating the formation of denser and more extensive fibrin networks. In contrast, Nb-PNCB:4 particles resulted in weaker turbidity responses, with the fluid remaining relatively transparent, particularly at the lower concentration (15 mg/mL). Notably, at 15 mg/mL of Nb-PNCB:4, a pronounced phase separation was observed, with the clot concentrating in a specific region of the vial, as also reflected by an anomalously high FTU value (617) in the quantitative data, Figure 3.22. This highlights the importance of considering physical interferences when using turbidity as a measure of clot formation.

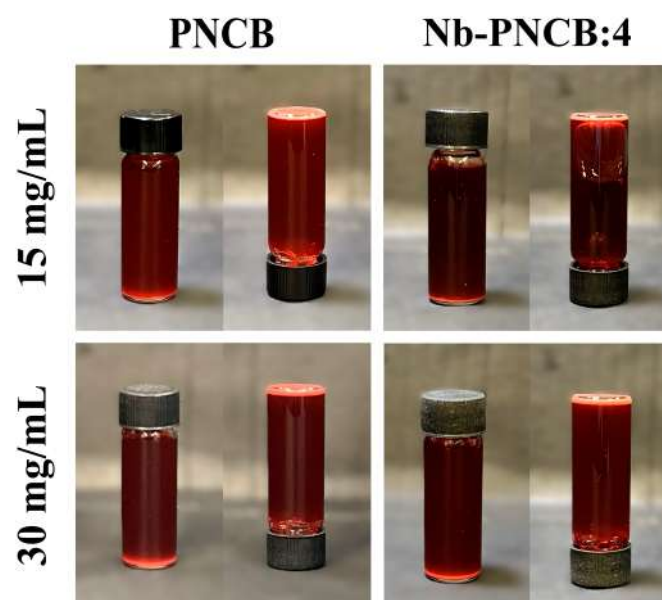


Figure 3.24: Photographic images of citrated blood at the end of turbidity tests mixed with glass particles at 15 mg/mL and 30 mg/mL.

Glasses Nb-free enhanced clot formation. In contrast, the Nb-PNCB:4 markedly impaired coagulation, evidenced by delayed or absent clot formation, likely due to reduced calcium availability and potential inhibitory effects of niobate species. Although the clotting time observed for the PNCB glass is longer than the calcium chloride control, it remains promising and can be further optimized through in-depth studies focused on adjusting composition and refining the ion release profile, which shows a clear dose-dependent behavior. These findings highlight the potential of tailored bioactive glasses for effective hemorrhage control and wound management.

CONCLUSION

The present study systematically investigated the effects of Nb_2O_5 addition in bioactive borate glasses, comprehensive structural, thermal, physicochemical, and mechanical characterization, as well as the evaluation of *in vitro* bioactivity, cytocompatibility, and hemostatic potential.

Initially, it was observed that the incorporation of Nb_2O_5 up to the Nb-PNCB:2 composition led to an increase in glass density, attributed to the formation of NbO_6 units and the equimolar substitution of network-modifying oxides (CaO and Na_2O). This modification resulted in greater structural compaction, evidenced by increasing values of the atomic packing factor (APF), as well as an increase in the glass transition temperature (T_g), both of which are indicators of enhanced network connectivity and thermal stability. In parallel, the radiopacity of the samples increased progressively with the Nb content, an effect associated with the higher electronic density and atomic number of niobium.

However, for the Nb-PNCB:3 and Nb-PNCB:4 compositions, signs of structural saturation were detected, with a stabilization of density and a decrease in both T_g and APF values, suggesting a transition in the role of Nb from network former to modifier. This change was accompanied by significant structural reorganization, marked by a decrease in BO_4 units and an increase in BO_3 units, as identified by ATR-FTIR analyses. This reorganization led to an increase in non-bridging oxygens (NBOs) and consequent depolymerization of the glass matrix, a phenomenon corroborated by Raman spectroscopy.

From a mechanical standpoint, the glasses up to Nb-PNCB:2 exhibited properties comparable to or superior to the control (PNCB), with high hardness and elastic modulus values. These results reinforce the structuring role of Nb at moderate concentrations. In contrast, the Nb-PNCB:3 and Nb-PNCB:4 samples showed a significant loss in mechanical

performance, consistent with a less connected and more fragile network.

The interaction with humidity, assessed by DVS analysis, revealed that the introduction of Nb reduced the water vapor sorption capacity, especially in intermediate compositions (Nb-PNCB:2 and Nb-PNCB:3), indicating increased chemical durability. However, the Nb-PNCB:4 composition showed increased sorption, consistent with a more depolymerized network. The ionic release indicated a decrease in medium pH with increasing Nb content, associated with a slower ion release, likely due to interactions between Nb and other species in solution. This hypothesis is supported by the progressive reduction in Nb concentration in the solution over time, suggesting the formation of Nb-rich layer or niobate units.

Regarding *in vitro* bioactivity, all compositions demonstrated the ability to form hydroxyapatite (HCA) in simulated body fluid (SBF), although the kinetics of formation decreased with higher Nb content. This deceleration is attributed to the lower dissolution rate, consistent with the formation of Nb-rich layers, which hinders the formation of HCA.

Cytocompatibility assessment, carried out with human adipose-derived mesenchymal stem cells (HuAD-MSCs), showed that the PNCB, Nb-PNCB:1, and Nb-PNCB:4 compositions did not exhibit significant cytotoxic effects over 10 days. Cell viability remained high, with active cellular metabolism, indicating that the dissolution products of the Nb-modified glasses are compatible with the cellular environment and may be considered safe for biomedical applications.

In hemorheological assays, it was evidenced that the hemostatic performance of the glasses is dose-dependent on ions or particles. Compositions containing Nb exhibited a reduced ability to induce coagulation, especially at higher concentrations, suggesting that excess Nb may interfere with the coagulation cascade, possibly due to calcium niobate species. Nevertheless, the PNCB glass demonstrated consistent pro-coagulant effects, making it promising for applications in bleeding control.

Overall, this thesis demonstrated that Nb acts as a versatile modulator of the properties of bioactive borate glasses, enabling fine-tuning of structural, mechanical, physicochemical, and biological characteristics. However, no direct link was observed between the role of niobium in glass and its bioactivity, except for the modulation of ionic release. Furthermore, it is not possible to select one composition as superior to the others, since the choice will depend on the specific biomedical application. Nevertheless, all evaluated

compositions proved to be promising candidates for future biomedical applications.

PUBLISHED MANUSCRIPTS

The research conducted during this doctoral program resulted in the submission of an original manuscript entitled “*Niobium in bioactive borate Glasses: dual structural role impacting Bioactivity, Cytocompatibility, and Hemostatic Function*” in the *ACS Applied Materials & Interfaces*. In parallel with central research activities, participation in collaborative projects led to the publication of several scientific manuscripts in peer-reviewed journals. The list below presents the publications co-authored during the period from 2022 to 2025, reflecting the contributions made throughout the Ph.D:

1. M. P. Belançon, M. Sandrini, R. Valcarenghi, R. D. Bini, M. S. Gibin, V. S. Zanuto, and R. F. Muniz, “Eu²⁺/³⁺: Yb³⁺ co-doped sodium calcium silicate glass: A case study of a spectral converter,” *Journal of Non-Crystalline Solids*, vol. 650, p. 123341, 2025
2. C. E. Scanferla, C. A. Moreira, A. G. Oliveira, H. dos Santos, M. S. Gibin, F. Sato, R. R. S. de Farias, F. P. Garcia, C. V. Nakamura, and D. M. F. de Oliveira, “Multi-functional Ca²⁺/Mg²⁺ codoped ZnO nano-semiconductors with enhanced photocatalytic performance and photo-modulated antibacterial action for the remediation of methyl orange dye and chlorpyrifos pesticide in binary systems,” *Ceramics International*, 2025
3. A. G. Oliveira, M. S. Gibin, F. P. Garcia, J. de Lara Andrade, M. V. P. Companhoni, P. R. S. Bittencourt, F. Sato, T. Ueda-Nakamura, A. A. W. Hechenleitner, E. A. G. Pineda, *et al.*, “Synthesis and characterization of Zn-modified hydroxyapatite photoactive composites from eggshell residues for bone regeneration,” *Journal of Photochemistry and Photobiology A: Chemistry*, vol. 449, p. 115432, 2024
4. J. W. Berrar, V. A. da Silva Almodôvar, M. S. Gibin, A. P. B. Cavalaro, V. S. Zanuto, A. C. Bento, N. G. C. Astrath, E. V. Bergmann, A. C. Tomé, L. C. Malacarne, *et al.*, “Diketopyrrolopyrrole-based organic dyes and their laser-induced photoactive response,” *Journal of Molecular Liquids*, vol. 398, p. 124208, 2024

5. G. B. G. Cândido, G. N. Fraga, A. R. de Souza Rossin, R. L. Lourenço, M. S. Gibin, V. S. Zanuto, J. Caetano, and D. C. Dragunski, "Influence of Lamotrigine concentration on physicochemical properties and transdermal release using PBAT/PLA electrospun fibers," *Colloids and Surfaces A: Physicochemical and Engineering Aspects*, vol. 686, p. 133216, 2024
6. L. Spessato, L. H. Crespo, M. C. Silva, M. S. Gibin, F. Sato, M. E. Winkler, and V. C. Almeida, "Tuning photodegradation performance using carbon quantum dots and niobium pentoxide," *Journal of Materials Science & Technology*, vol. 191, pp. 157–167, 2024
7. E. R. Machado Filho, A. Lazzari, B. R. Saraiva, D. E. R. Gonzaga, M. S. Gibin, W. D. dos Santos, F. Sato, and P. T. Matumoto Pinto, "Potential of barley straw pretreated with a lignin inhibitor as an adjunct during beer production," *International Journal of Food Science and Technology*, vol. 59, no. 5, pp. 3142–3150, 2024
8. G. H. D. R. Almeida, R. S. da Silva, M. S. Gibin, V. H. d. S. Gonzaga, H. Dos Santos, R. P. Igleisa, L. A. Fernandes, I. C. Fernandes, T. N. G. Nesiyaama, F. Sato, *et al.*, "Region-specific decellularization of porcine uterine tube extracellular matrix: A new approach for reproductive tissue-engineering applications," *Biomimetics*, vol. 9, no. 7, p. 382, 2024
9. G. H. D. R. Almeida, M. S. Gibin, J. d. C. Rinaldi, V. H. d. S. Gonzaga, C. R. Thom, R. P. Iglesia, R. S. da Silva, I. C. Fernandes, R. O. Bergamo, L. S. Lima, *et al.*, "Development and Biocompatibility Assessment of Decellularized Porcine Uterine Extracellular Matrix-Derived Grafts," *Tissue Engineering Part C: Methods*, vol. 30, no. 12, pp. 569–589, 2024
10. A. Lazzari, M. S. Gibin, B. R. Saraiva, F. Sato, C. I. L. F. Rosa, and P. T. M. Pinto, "Top-fermented beer enriched with Ceylon Gooseberry residue—The effect on bioactive compound content and sensorial profile," *International Journal of Gastronomy and Food Science*, vol. 37, p. 100991, 2024
11. M. Sandrini, J. C. Gemelli, M. S. Gibin, V. S. Zanuto, R. F. Muniz, F. S. de Vicente, and M. P. Belançon, "Synthesis and properties of Cerium-doped organic/silica xerogels: A potential UV filter for photovoltaic panels," *Journal of Non-Crystalline Solids*, vol. 600, p. 122033, 2023
12. T. Moriwaki, R. Falcioni, M. E. Giacomelli, M. S. Gibin, F. Sato, M. R. Nanni, S. M. Lima, L. H. da Cunha Andrade, M. L. Baesso, and W. C. Antunes, "Chloroplast and outside-chloroplast interference of light inside leaves," *Environmental and Experimental Botany*, vol. 208, p. 105258, 2023

13. G. N. Fraga, D. C. Dragunski, B. H. Vilsinski, C. K. da Silva Azevedo, H. J. Wiggers, M. G. I. Faria, J. Caetano, M. R. da Costa, V. S. Zanuto, A. R. S. Rossin, *et al.*, "Dressings produced from PVA nanofibers containing chloramphenicol," *Colloids and Surfaces A: Physicochemical and Engineering Aspects*, vol. 674, p. 131760, 2023
14. M. H. Pacheco, M. S. Gibin, M. A. Silva, G. Montagnini, R. C. Viscovini, A. Steimacher, F. Pedrochi, V. S. Zanuto, and R. F. Muniz, "BaO-reinforced SiO₂-Na₂O-Ca(O/F₂)-Al₂O₃ glasses for radiation safety: on the physical, optical, structural and radiation shielding properties," *Journal of Alloys and Compounds*, vol. 960, p. 171019, 2023
15. G. H. D. R. Almeida, L. N. da Silva-Júnior, M. S. Gibin, H. Dos Santos, B. de Oliveira Horvath-Pereira, L. B. M. Pinho, M. L. Baesso, F. Sato, L. Hernandez, C. R. Long, *et al.*, "Perfusion and ultrasonication produce a decellularized porcine whole-ovary scaffold with a preserved microarchitecture," *Cells*, vol. 12, no. 14, p. 1864, 2023
16. B. R. Saraiva, A. C. M. Cegudo, M. S. Gibin, J. B. Da Silva, F. Sato, M. L. Bruschi, and P. T. Matumoto-Pintro, "Co-product from debittering process of trub (brewing by-product) as natural antioxidant in processed cheese," *International Journal of Food Science and Technology*, vol. 58, no. 12, pp. 6752–6760, 2023
17. C. M. Paraíso, J. dos Santos Pizzo, M. S. Gibin, E. A. Volnistem, J. V. Visentainer, F. Sato, S. C. da Costa, M. H. M. Reis, and G. S. Madrona, "Intensified ultrafiltration process for fouling mitigation during concentration of bioactive compounds from hibiscus (*Hibiscus sabdariffa* L.) extract: Innovation by using ultrasound and 3D turbulence promoters," *Chemical Engineering and Processing-Process Intensification*, vol. 195, p. 109612, 2024
18. M. T. C. Wolowski, A. M. S. Grenier, V. A. de Oliveira, C. Anselmi, M. S. Gibin, L. V. de Castro-Hoshino, F. Sato, C. Perez, R. H. Scheffel, J. Hebling, *et al.*, "Performance of self-etching adhesives on caries-affected primary dentin treated with glutaraldehyde or silver diamine fluoride," *Journal of the Mechanical Behavior of Biomedical Materials*, vol. 150, p. 106293, 2024
19. R. Muniz, V. Zanuto, M. Gibin, J. Gunha, A. Novatski, J. Rohling, A. Medina, and M. Baesso, "Down-and up-conversion processes in Nd³⁺/Yb³⁺ co-doped sodium calcium silicate glasses with concomitant Yb²⁺ assessment," *Journal of Rare Earths*, vol. 41, no. 3, pp. 342–348, 2023
20. W. R. Weinand, J. A. Cruz, A. N. Medina, W. M. Lima, F. Sato, R. da Silva Palacios, M. S. Gibin, E. A. Volnistem, J. M. Rosso, I. A. Santos, *et al.*, "Dynamics of the natural genesis of β -TCP/HAp phases in postnatal fishbones towards gold standard biocomposites for bone regeneration," *Spectrochimica Acta Part A: Molecular and Biomolecular Spectroscopy*, vol. 279, p. 121407, 2022

21. B. R. Saraiva, J. C. Zancheta, M. Sversut Gibin, F. A. Anjo, A. Lazzari, E. R. Machado Filho, F. Sato, and P. Matumoto-Pintro, “Brewing by-product valorisation: trub debittered for nutritional and quality improvement of pasta,” *International Journal of Food Sciences and Nutrition*, vol. 73, no. 7, pp. 915–926, 2022
22. R. Falcioni, T. Moriwaki, M. S. Gibin, A. Vollmann, M. C. Pattaro, M. E. Giacomelli, F. Sato, M. R. Nanni, and W. C. Antunes, “Classification and prediction by pigment content in lettuce (*Lactuca sativa* L.) varieties using machine learning and ATR-FTIR spectroscopy,” *Plants*, vol. 11, no. 24, p. 3413, 2022

BIBLIOGRAPHY

- [1] V. Miguez-Pacheco, D. De Ligny, J. Schmidt, R. Detsch, and A. Boccaccini, “Development and characterization of niobium-releasing silicate bioactive glasses for tissue engineering applications,” *Journal of the European Ceramic Society*, vol. 38, pp. 871–876, Mar. 2018.
- [2] H. Maeda, S. Lee, T. Miyajima, A. Obata, K. Ueda, T. Narushima, and T. Kasuga, “Structure and physicochemical properties of $\text{CaO-P}_2\text{O}_5\text{-Nb}_2\text{O}_5\text{-Na}_2\text{O}$ glasses,” *Journal of Non-Crystalline Solids*, vol. 432, pp. 60–64, Jan. 2016.
- [3] G. D. S. Balbinot, F. M. Collares, F. Visioli, P. B. F. Soares, A. S. Takimi, S. M. W. Samuel, and V. C. B. Leitune, “Niobium addition to sol-gel derived bioactive glass powders and scaffolds: In vitro characterization and effect on pre-osteoblastic cell behavior,” *Dental Materials*, vol. 34, pp. 1449–1458, Oct. 2018.
- [4] W. C. Lepry, S. Smith, and S. N. Nazhat, “Effect of sodium on bioactive sol-gel-derived borate glasses,” *Journal of Non-Crystalline Solids*, vol. 500, pp. 141–148, Nov. 2018.
- [5] A. Obata, Y. Takahashi, T. Miyajima, K. Ueda, T. Narushima, and T. Kasuga, “Effects of Niobium Ions Released from Calcium Phosphate Invert Glasses Containing Nb_2O_5 on Osteoblast-Like Cell Functions,” *ACS Applied Materials & Interfaces*, vol. 4, pp. 5684–5690, Oct. 2012.
- [6] W. C. Lepry and S. N. Nazhat, “Highly Bioactive Sol-Gel-Derived Borate Glasses,” *Chemistry of Materials*, vol. 27, pp. 4821–4831, July 2015.
- [7] T. Yin, W. C. Lepry, P. Hudon, P. Ouzilleau, K. E. Waters, and S. N. Nazhat, “Mechanism of dissolution reactivity and reactions of various calcium borate glasses and glass-ceramics,” *Journal of Non-Crystalline Solids*, vol. 614, p. 122406, Aug. 2023.

- [8] S. Pourshahrestani, N. A. Kadri, E. Zeimaran, N. Gargiulo, S. Samuel, S. V. Naveen, K. Hasikin, T. Kamarul, and M. R. Towler, “Comparative efficacy of hemorrhage control of a novel mesoporous bioactive glass versus two commercial hemostats,” *Biomedical Materials*, vol. 13, p. 025020, Feb. 2018.
- [9] U. Pantulap, M. Arango-Ospina, and A. R. Boccaccini, “Bioactive glasses incorporating less-common ions to improve biological and physical properties,” *Journal of Materials Science: Materials in Medicine*, vol. 33, p. 3, Jan. 2022.
- [10] S. R. Gavinho, A. S. Pádua, L. I. V. Holz, I. Sá-Nogueira, J. C. Silva, J. P. Borges, M. A. Valente, and M. P. F. Graça, “Bioactive Glasses Containing Strontium or Magnesium Ions to Enhance the Biological Response in Bone Regeneration,” *Nanomaterials*, vol. 13, p. 2717, Oct. 2023.
- [11] W. C. Lepry, G. Griffanti, and S. N. Nazhat, “Bioactive sol-gel borate glasses with magnesium,” *Journal of Non-Crystalline Solids*, vol. 581, p. 121415, Apr. 2022.
- [12] J. Bejarano, P. Caviedes, and H. Palza, “Sol–gel synthesis and *in vitro* bioactivity of copper and zinc-doped silicate bioactive glasses and glass-ceramics,” *Biomedical Materials*, vol. 10, p. 025001, Mar. 2015.
- [13] R. Samudrala, Abdul Azeem P, V. Penugurti, and B. Manavathi, “Cytocompatibility studies of titania-doped calcium borosilicate bioactive glasses in-vitro,” *Materials Science and Engineering: C*, vol. 77, pp. 772–779, Aug. 2017.
- [14] A. Goel, S. Kapoor, A. Tilocca, R. R. Rajagopal, and J. M. F. Ferreira, “Structural role of zinc in biodegradation of alkali-free bioactive glasses,” *Journal of Materials Chemistry B*, vol. 1, no. 24, p. 3073, 2013.
- [15] J. H. Lopes, A. Magalhães, I. O. Mazali, and C. A. Bertran, “Effect of Niobium Oxide on the Structure and Properties of Melt-Derived Bioactive Glasses,” *Journal of the American Ceramic Society*, vol. 97, pp. 3843–3852, Dec. 2014.
- [16] T. Komatsu, T. Honma, T. Tasheva, and V. Dimitrov, “Structural role of Nb₂O₅ in glass-forming ability, electronic polarizability and nanocrystallization in glasses: A review,” *Journal of Non-Crystalline Solids*, vol. 581, p. 121414, Apr. 2022.
- [17] R. Samudrala, P. Abdul Azeem, V. Penugurti, and B. Manavathi, “In vitro evaluation of niobia added soda lime borosilicate bioactive glasses,” *Journal of Alloys and Compounds*, vol. 764, pp. 1072–1078, Oct. 2018.
- [18] K. K. Carneiro, T. P. Araujo, E. M. Carvalho, M. M. Meier, A. Tanaka, C. N. Carvalho, and J. Bauer, “Bioactivity and properties of an adhesive system functionalized with an experimental niobium-based glass,” *Journal of the Mechanical Behavior of Biomedical Materials*, vol. 78, pp. 188–195, Feb. 2018.

- [19] J. H. Lopes, L. P. Souza, J. A. Domingues, F. V. Ferreira, M. De Alencar Hausen, J. A. Camilli, R. A. Martin, E. A. De Rezende Duek, I. O. Mazali, and C. A. Bertran, “In vitro and in vivo osteogenic potential of niobium-doped 45S5 bioactive glass: A comparative study,” *Journal of Biomedical Materials Research Part B: Applied Biomaterials*, vol. 108, pp. 1372–1387, May 2020.
- [20] J. E. Shelby, *Introduction to glass science and technology*. Royal society of chemistry, 2020.
- [21] W. Holand and G. H. Beall, *Glass-ceramic technology*. John Wiley & Sons, 2019.
- [22] A. K. Varshneya, *Fundamentals of inorganic glasses*. Elsevier, 2013.
- [23] E. D. Zanotto and J. C. Mauro, “The glassy state of matter: Its definition and ultimate fate,” *Journal of Non-Crystalline Solids*, vol. 471, pp. 490–495, 2017.
- [24] C. J. Brinker and G. W. Scherer, *Sol-gel science: the physics and chemistry of sol-gel processing*. Academic press, 2013.
- [25] W. H. Zachariasen, “The atomic arrangement in glass,” *Journal of the American Chemical Society*, vol. 54, no. 10, pp. 3841–3851, 1932.
- [26] J. Goubeau and H. Keller, “Raman-spektren und struktur von boroxol-verbindungen,” *Zeitschrift für anorganische und allgemeine Chemie*, vol. 272, no. 5-6, pp. 303–312, 1953.
- [27] A. C. Wright, “Borate structures: crystalline and vitreous,” *Physics and Chemistry of Glasses-European Journal of Glass Science and Technology Part B*, vol. 51, no. 1, pp. 1–39, 2010.
- [28] A. R. Boccaccini, D. S. Brauer, and L. Hupa, *Bioactive glasses: fundamentals, technology and applications*. Royal Society of Chemistry, 2016.
- [29] G. M. Raghavendra, K. Varaprasad, and T. Jayaramudu, “Biomaterials: design, development and biomedical applications,” in *Nanotechnology applications for tissue engineering*, pp. 21–44, Elsevier, 2015.
- [30] S. Donglu, *Introduction to biomaterials*. World Scientific, 2005.
- [31] S. H. Teoh, *Engineering materials for biomedical applications*, vol. 1. World Scientific, 2004.
- [32] V. Migonney, “History of biomaterials,” in *Biomaterials*, pp. 1–10, Wiley Online Library, 2014.
- [33] S. Bose and A. Bandyopadhyay, “Introduction to biomaterials,” in *Characterization of Biomaterials*, pp. 1–9, Elsevier, 2013.

- [34] C. Ning, L. Zhou, and G. Tan, “Fourth-generation biomedical materials,” *Materials Today*, vol. 19, no. 1, pp. 2–3, 2016.
- [35] L. L. Hench, *An introduction to bioceramics*, vol. 1. World Scientific, 1993.
- [36] L. L. Hench, R. J. Splinter, W. Allen, and T. Greenlee, “Bonding mechanisms at the interface of ceramic prosthetic materials,” *Journal of biomedical materials research*, vol. 5, no. 6, pp. 117–141, 1971.
- [37] L. L. Hench, “The story of bioglass®,” *Journal of materials science: materials in medicine*, vol. 17, no. 11, pp. 967–978, 2006.
- [38] T. Kokubo and H. Takadama, “How useful is sbf in predicting in vivo bone bioactivity?,” *Biomaterials*, vol. 27, no. 15, pp. 2907–2915, 2006.
- [39] J. Jones and A. Clare, *Bioglasses: an introduction*. John Wiley & Sons, 2012.
- [40] K. L. Goetschius, M. A. Beuerlein, C. M. Bischoff, and R. K. Brow, “Dissolution behavior of ternary alkali-alkaline earth-borate glasses in water,” *Journal of Non-Crystalline Solids*, vol. 487, pp. 12–18, 2018.
- [41] O. D. Abodunrin, K. El Mabrouk, and M. Bricha, “A review on borate bioactive glasses (BBG): effect of doping elements, degradation, and applications,” *Journal of Materials Chemistry B*, vol. 11, no. 5, pp. 955–973, 2023.
- [42] J. F. Papp, “Niobium,” *Metal Prices in the United States Through 2010*, p. 114, 2010.
- [43] C. G. Bruziquesi, J. G. Balena, M. C. Pereira, A. C. Silva, and L. C. Oliveira, “Nióbio: um elemento químico estratégico para o brasil,” *Química nova*, vol. 42, no. 10, pp. 1184–1188, 2019.
- [44] G. Wu, A.-M. Valente, H. Phillips, H. Wang, A. Wu, T. Renk, and P. Provencio, “Studies of niobium thin film produced by energetic vacuum deposition,” *Thin Solid Films*, vol. 489, no. 1-2, pp. 56–62, 2005.
- [45] D. Finnemore, T. Stromberg, and C. Swenson, “Superconducting properties of high-purity niobium,” *Physical Review*, vol. 149, no. 1, p. 231, 1966.
- [46] S. Schneider, S. G. Schneider, H. M. d. Silva, and C. d. Moura Neto, “Study of the non-linear stress-strain behavior in ti-nb-zr alloys,” *Materials Research*, vol. 8, pp. 435–438, 2005.
- [47] K. Hulka, “The role of niobium in low carbon bainitic hsla steel,” in *Proceedings of the 1st Int. Conference on Super-High Strength Steels/Roma*, pp. 11–24, 2005.

- [48] S. Pérez-Walton, C. Valencia-Balvín, G. M. Dalpian, and J. M. Osorio-Guillén, “Electronic, dielectric, and optical properties of the b phase of niobium pentoxide and tantalum pentoxide by first-principles calculations,” *physica status solidi (b)*, vol. 250, no. 8, pp. 1644–1650, 2013.
- [49] K. Kusumoto, “Dielectric and piezoelectric properties of $\text{KNbO}_3\text{--NaNbO}_3\text{--LiNbO}_3\text{--SrTiO}_3$ ceramics,” *Japanese journal of applied physics*, vol. 45, no. 9S, p. 7440, 2006.
- [50] L. Souza, J. H. Lopes, D. Encarnação, I. O. Mazali, R. A. Martin, J. A. Camilli, and C. A. Bertran, “Comprehensive in vitro and in vivo studies of novel melt-derived Nb-substituted 45S5 bioglass reveal its enhanced bioactive properties for bone healing,” *Scientific Reports*, vol. 8, p. 12808, Aug. 2018.
- [51] E. I. Kamitsos, M. A. Karakassides, and G. D. Chryssikos, “Vibrational spectra of magnesium-sodium-borate glasses. 2. Raman and mid-infrared investigation of the network structure,” *The Journal of Physical Chemistry*, vol. 91, pp. 1073–1079, Feb. 1987.
- [52] R. Iordanova, M. Milanova, L. Aleksandrov, K. Shinozaki, and T. Komatsu, “Structural study of $\text{WO}_3\text{--La}_2\text{O}_3\text{--B}_2\text{O}_3\text{--Nb}_2\text{O}_5$ glasses,” *Journal of Non-Crystalline Solids*, vol. 543, p. 120132, Sept. 2020.
- [53] E. Abdel-Khalek, E. Mohamed, A. Ratep, S. M. Salem, and I. Kashif, “Structural, optical and dielectric characterization of niobium lithium tetraborate glasses doped praseodymium,” *Journal of Non-Crystalline Solids*, vol. 441, pp. 58–65, June 2016.
- [54] D. Ehrt, “Structure, properties and applications of borate glasses,” *Glass technology*, vol. 41, no. 6, pp. 182–185, 2000.
- [55] G. B. de Boer, C. de Weerd, D. Thoenes, and H. W. Goossens, “Laser diffraction spectrometry: Fraunhofer diffraction versus mie scattering,” *Particle & Particle Systems Characterization*, vol. 4, no. 1-4, pp. 14–19, 1987.
- [56] S. Brunauer, P. H. Emmett, and E. Teller, “Adsorption of gases in multimolecular layers,” *Journal of the American chemical society*, vol. 60, no. 2, pp. 309–319, 1938.
- [57] L. G. Joyner, E. P. Barrett, and R. Skold, “The determination of pore volume and area distributions in porous substances. ii. comparison between nitrogen isotherm and mercury porosimeter methods,” *Journal of the American Chemical Society*, vol. 73, no. 7, pp. 3155–3158, 1951.
- [58] U. Chanshetti, V. Shelke, S. Jadhav, S. Shankarwar, T. Chondhekar, A. Shankarwar, V. Sudarsan, and M. Jogad, “Density and molar volume studies of phosphate glasses,” *Facta universitatis-series: Physics, Chemistry and Technology*, vol. 9, no. 1, pp. 29–36, 2011.

- [59] C. Kittel, *Solid state physics*, vol. 3. Shell Development Company Emeryville, 1955.
- [60] M. M. Smedskjaer, J. C. Mauro, S. Sen, J. Deubener, and Y. Yue, “Impact of network topology on cationic diffusion and hardness of borate glass surfaces,” *The Journal of chemical physics*, vol. 133, no. 15, 2010.
- [61] R. D. Shannon, “Revised effective ionic radii and systematic studies of interatomic distances in halides and chalcogenides,” *Acta Crystallographica Section A*, vol. 32, pp. 751–767, Sept. 1976.
- [62] P. Larkin, *Infrared and Raman spectroscopy: principles and spectral interpretation*. Elsevier, 2017.
- [63] B. C. Smith, *Fundamentals of Fourier transform infrared spectroscopy*. CRC press, 2011.
- [64] E. Smith and G. Dent, *Modern Raman spectroscopy: a practical approach*. John Wiley & Sons, 2019.
- [65] A. C. Fischer-Cripps and D. Nicholson, “Nanoindentation. mechanical engineering series,” *Appl. Mech. Rev.*, vol. 57, no. 2, pp. B12–B12, 2004.
- [66] W. C. Oliver and G. M. Pharr, “An improved technique for determining hardness and elastic modulus using load and displacement sensing indentation experiments,” *Journal of materials research*, vol. 7, no. 6, pp. 1564–1583, 1992.
- [67] G. Paramesh and K. Varma, “Mechanical properties of glasses and TiO₂ nanocrystal glass composites in BaO–TiO₂–B₂O₃ system,” *Journal of non-crystalline solids*, vol. 380, pp. 128–134, 2013.
- [68] L. D’Andrea, A. De Cet, D. Gastaldi, F. Baino, E. Verné, and P. Vena, “Estimation of elastic modulus, fracture toughness and strength of 47.5B-derived bioactive glass-ceramics for bone scaffold applications: A nanoindentation study,” *Materials Letters*, vol. 335, p. 133783, 2023.
- [69] W. C. Lepry, G. Griffanti, and S. N. Nazhat, “Bioactive sol-gel borate glasses with magnesium,” *Journal of Non-Crystalline Solids*, vol. 581, p. 121415, 2022.
- [70] E. Rezabeigi, C. Schmitt, A. Hadj Henni, A. N. Barkun, and S. N. Nazhat, “In vitro evaluation of real-time viscoelastic and coagulation properties of various classes of topical hemostatic agents using a novel contactless nondestructive technology,” *ACS Applied Materials & Interfaces*, vol. 14, no. 14, pp. 16047–16061, 2022.
- [71] D. B. Camasao, J. G. Munguia-Lopez, A. Perez, J. A. Correa, C. Schmitt, A. H. Henni, C. Séguin, D. C. Vinh, and S. N. Nazhat, “Coagulation profile and clot

- stiffness analysis from covid-19-positive patients using a contactless viscoelasticity testing technology,” *Biomedical Materials & Devices*, pp. 1–7, 2024.
- [72] G. F. Silva, M. Tanomaru-Filho, M. I. B. Bernardi, J. M. Guerreiro-Tanomaru, and P. S. Cerri, “Niobium pentoxide as radiopacifying agent of calcium silicate-based material: evaluation of physicochemical and biological properties,” *Clinical Oral Investigations*, vol. 19, pp. 2015–2025, Nov. 2015.
 - [73] L. B. Mestieri, A. L. Gomes-Cornélio, E. M. Rodrigues, G. Faria, J. M. Guerreiro-Tanomaru, and M. Tanomaru-Filho, “Cytotoxicity and Bioactivity of Calcium Silicate Cements Combined with Niobium Oxide in Different Cell Lines,” *Brazilian Dental Journal*, vol. 28, pp. 65–71, Feb. 2017.
 - [74] J. M. Guerreiro Tanomaru, I. Storto, G. F. Da Silva, R. Bosso, B. C. Costa, M. I. B. Bernardi, and M. Tanomaru-Filho, “Radiopacity, pH and antimicrobial activity of Portland cement associated with micro- and nanoparticles of zirconium oxide and niobium oxide,” *Dental Materials Journal*, vol. 33, no. 4, pp. 466–470, 2014.
 - [75] A. Saeed, Y. H. Elbashar, and S. U. El Khameesy, “A Novel Barium Borate Glasses for Optical Applications,” *Silicon*, vol. 10, pp. 569–574, Mar. 2018.
 - [76] D. Möncke, E. I. Kamitsos, D. Palles, R. Limbach, A. Winterstein-Beckmann, T. Honma, Z. Yao, T. Rouxel, and L. Wondraczek, “Transition and post-transition metal ions in borate glasses: Borate ligand speciation, cluster formation, and their effect on glass transition and mechanical properties,” *The Journal of Chemical Physics*, vol. 145, p. 124501, Sept. 2016.
 - [77] W. C. Lepry, S. Naseri, and S. N. Nazhat, “Effect of processing parameters on textural and bioactive properties of sol–gel-derived borate glasses,” *Journal of Materials Science*, vol. 52, pp. 8973–8985, Aug. 2017.
 - [78] A. M. Deliormanlı, “In vitro assessment of degradation and bioactivity of robocast bioactive glass scaffolds in simulated body fluid,” *Ceramics International*, vol. 38, pp. 6435–6444, Dec. 2012.
 - [79] C. Gautam, A. K. Yadav, and A. K. Singh, “A Review on Infrared Spectroscopy of Borate Glasses with Effects of Different Additives,” *ISRN Ceramics*, vol. 2012, pp. 1–17, Nov. 2012.
 - [80] S. Agathopoulos, D. Tulyaganov, J. Ventura, S. Kannan, M. Karakassides, and J. Ferreira, “Formation of hydroxyapatite onto glasses of the CaO–MgO–SiO₂ system with B₂O₃, Na₂O, CaF₂ and P₂O₅ additives,” *Biomaterials*, vol. 27, pp. 1832–1840, Mar. 2006.

- [81] L. Balachander, G. Ramadevudu, M. Shareefuddin, R. Sayanna, and Y. Venudhar, “IR analysis of borate glasses containing three alkali oxides,” *ScienceAsia*, vol. 39, no. 3, p. 278, 2013.
- [82] D. Carta, D. Qiu, P. Guerry, I. Ahmed, E. A. Abou Neel, J. C. Knowles, M. E. Smith, and R. J. Newport, “The effect of composition on the structure of sodium borophosphate glasses,” *Journal of Non-Crystalline Solids*, vol. 354, pp. 3671–3677, Aug. 2008.
- [83] Y. Yiannopoulos, G. D. Chryssikos, and E. Kamitsos, “Structure and properties of alkaline earth borate glasses,” *Physics and chemistry of glasses*, vol. 42, no. 3, pp. 164–172, 2001.
- [84] W. C. Lepry and S. N. Nazhat, “The anomaly in bioactive sol–gel borate glasses,” *Materials Advances*, vol. 1, no. 5, pp. 1371–1381, 2020.
- [85] T. Hübert, U. Banach, K. Witke, and P. Reich, “Structural studies of glasses in the system $\text{SrO-B}_2\text{O}_3\text{-Al}_2\text{O}_3\text{-TiO}_2$,” *Physics and Chemistry of Glasses*, vol. 32, pp. 58–66, 1991.
- [86] B. Meera and J. Ramakrishna, “Raman spectral studies of borate glasses,” *Journal of Non-Crystalline Solids*, vol. 159, pp. 1–21, June 1993.
- [87] W. Konijnendijk and J. Stevels, “The structure of borate glasses studied by Raman scattering,” *Journal of Non-Crystalline Solids*, vol. 18, pp. 307–331, Nov. 1975.
- [88] P. Pascuta, R. Lungu, and I. Ardelean, “FTIR and Raman spectroscopic investigation of some strontium–borate glasses doped with iron ions,” *Journal of Materials Science: Materials in Electronics*, vol. 21, pp. 548–553, June 2010.
- [89] B. Sudhakar, N. Chand, H. Prasanna, G. S. Rao, K. V. Rao, and V. Dhand, “Vibrational spectral analysis of structural modifications of Cr_2O_3 containing oxyfluoroborate glasses,” *Journal of Non-Crystalline Solids*, vol. 356, pp. 2211–2217, Sept. 2010.
- [90] A. K. Yadav and P. Singh, “A review of the structures of oxide glasses by Raman spectroscopy,” *RSC Advances*, vol. 5, no. 83, pp. 67583–67609, 2015.
- [91] B. Meera, A. Sood, N. Chandrabhas, and J. Ramakrishna, “Raman study of lead borate glasses,” *Journal of Non-Crystalline Solids*, vol. 126, pp. 224–230, Dec. 1990.
- [92] L. Koudelka, P. Kalenda, P. Mošner, L. Montagne, and B. Revel, “Structure–property relationships in barium borophosphate glasses modified with niobium oxide,” *Journal of Non-Crystalline Solids*, vol. 437, pp. 64–71, Apr. 2016.

- [93] F. Sene, J. Martinelli, and L. Gomes, “Synthesis and characterization of niobium phosphate glasses containing barium and potassium,” *Journal of Non-Crystalline Solids*, vol. 348, pp. 30–37, Nov. 2004.
- [94] T. Cardinal, E. Fargin, G. Le Flem, M. Couzi, L. Canioni, P. Segonds, L. Sarger, A. Ducasse, and F. Adamietz, “Non linear optical properties of some Niobium (V) oxide glass,” *Non linear optical properties of some Niobium (V) oxide glass*, no. 33, pp. 597–605, 1996.
- [95] B. Yu, B. Chen, X. Yang, J. Qiu, X. Jiang, C. Zhu, and K. Hirao, “Study of crystal formation in borate, niobate, and titanate glasses irradiated by femtosecond laser pulses,” *Journal of the Optical Society of America B*, vol. 21, p. 83, Jan. 2004.
- [96] K. I. Chatzipanagis, N. S. Tagiara, E. I. Kamitsos, N. Barrow, I. Slagle, R. Wilson, T. Greiner, M. Jesuit, N. Leonard, A. Phillips, B. Reynolds, B. Royle, K. Ameku, and S. Feller, “Structure of lead borate glasses by Raman, ^{11}B MAS, and ^{207}Pb NMR spectroscopies,” *Journal of Non-Crystalline Solids*, vol. 589, p. 121660, Aug. 2022.
- [97] A. Sharma, S. H. Nandam, H. Hahn, and K. E. Prasad, “Effect of Structural Relaxation on the Indentation Size Effect and Deformation Behavior of Cu–Zr–Based Nanoglasses,” *Frontiers in Materials*, vol. 8, p. 676764, June 2021.
- [98] T. Yin, W. C. Lepry, S. Naseri, M. T. Islam, I. Ahmed, P. Ouzilleau, K. E. Waters, and S. N. Nazhat, “Characterization of sodium and calcium addition on immediate aqueous interactions of binary borate glasses by dynamic vapour sorption with in-situ Raman,” *Journal of Non-Crystalline Solids*, vol. 599, p. 121957, Jan. 2023.
- [99] C. Stähli, M. James-Bhasin, A. Hoppe, A. R. Boccaccini, and S. N. Nazhat, “Effect of ion release from Cu-doped 45S5 Bioglass® on 3D endothelial cell morphogenesis,” *Acta Biomaterialia*, vol. 19, pp. 15–22, June 2015.
- [100] Manupriya, K. Thind, K. Singh, V. Kumar, G. Sharma, D. Singh, and D. Singh, “Compositional dependence of in-vitro bioactivity in sodium calcium borate glasses,” *Journal of Physics and Chemistry of Solids*, vol. 70, pp. 1137–1141, Aug. 2009.
- [101] S. Naseri, W. C. Lepry, V. B. Maisuria, N. Tufenkji, and S. N. Nazhat, “Development and characterization of silver-doped sol-gel-derived borate glasses with anti-bacterial activity,” *Journal of Non-Crystalline Solids*, vol. 505, pp. 438–446, Feb. 2019.
- [102] T. G. M. Bonadio, F. Sato, A. N. Medina, W. R. Weinand, M. L. Baesso, and W. M. Lima, “Bioactivity and structural properties of nanostructured bulk composites containing Nb_2O_5 and natural hydroxyapatite,” *Journal of Applied Physics*, vol. 113, p. 223505, June 2013.

- [103] C. Rey, M. Shimizu, B. Collins, and M. J. Glimcher, “Resolution-enhanced fourier transform infrared spectroscopy study of the environment of phosphate ion in the early deposits of a solid phase of calcium phosphate in bone and enamel and their evolution with age: 2. Investigations in the ν_3 PO₄ domain,” *Calcified Tissue International*, vol. 49, pp. 383–388, Nov. 1991.
- [104] A. Ślósarczyk, C. Paluszkiwicz, M. Gawlicki, and Z. Paszkiewicz, “The FTIR spectroscopy and QXRD studies of calcium phosphate based materials produced from the powder precursors with different ratios,” *Ceramics International*, vol. 23, pp. 297–304, Jan. 1997.
- [105] W. Huang, D. E. Day, K. Kittiratanapiboon, and M. N. Rahaman, “Kinetics and mechanisms of the conversion of silicate (45S5), borate, and borosilicate glasses to hydroxyapatite in dilute phosphate solutions,” *Journal of Materials Science: Materials in Medicine*, vol. 17, pp. 583–596, July 2006.
- [106] I. Kansal, A. Reddy, F. Muñoz, S.-J. Choi, H.-W. Kim, D. U. Tulyaganov, and J. M. Ferreira, “Structure, biodegradation behavior and cytotoxicity of alkali-containing alkaline-earth phosphosilicate glasses,” *Materials Science and Engineering: C*, vol. 44, pp. 159–165, Nov. 2014.
- [107] K. E. Wallace, R. G. Hill, J. T. Pembroke, C. J. Brown, and P. V. Hatton, “Influence of sodium oxide content on bioactive glass properties,” *Journal of Materials Science: Materials in Medicine*, vol. 10, pp. 697–701, Dec. 1999.
- [108] L.-E. Monfoulet, P. Becquart, D. Marchat, K. Vandamme, M. Bourguignon, E. Pacard, V. Viateau, H. Petite, and D. Logeart-Avramoglou, “The pH in the Microenvironment of Human Mesenchymal Stem Cells Is a Critical Factor for Optimal Osteogenesis in Tissue-Engineered Constructs,” *Tissue Engineering Part A*, vol. 20, pp. 1827–1840, July 2014.
- [109] M. H. Prado Da Silva, C. M. Ramirez, J. M. Granjeiro, and A. M. Rossi, “In Vitro Assessment of New Niobium Phosphate Glasses and Glass Ceramics,” *Key Engineering Materials*, vol. 361-363, pp. 229–232, Nov. 2007.
- [110] S. Naseri, N. Koushki, E. Rezabeigi, A. Ehrlicher, and S. N. Nazhat, “A nondestructive contactless technique to assess the viscoelasticity of blood clots in real-time,” *Journal of the Mechanical Behavior of Biomedical Materials*, vol. 110, p. 103921, Oct. 2020.
- [111] S. Pourshahrestani, E. Zeimaran, I. Djordjevic, N. A. Kadri, and M. R. Towler, “Inorganic hemostats: The state-of-the-art and recent advances,” *Materials Science and Engineering: C*, vol. 58, pp. 1255–1268, Jan. 2016.

- [112] R. Chambrey and F. Trepiccione, “Relative Roles of Principal and Intercalated Cells in the Regulation of Sodium Balance and Blood Pressure,” *Current Hypertension Reports*, vol. 17, p. 27, Apr. 2015.
- [113] J. Razavi and A. Arbabian, “Chromatic Properties of Blood During Coagulation,” in *2019 41st Annual International Conference of the IEEE Engineering in Medicine and Biology Society (EMBC)*, (Berlin, Germany), pp. 4733–4736, IEEE, July 2019.
- [114] H. Sakamoto, N. Hibino, Y. Mizukuchi, A. Sato, and T. Torii, “Detection of blood coagulation in an extracorporeal circuit using magnetic and absorbance properties,” *AIP Advances*, vol. 14, p. 015038, Jan. 2024.
- [115] M. P. Belançon, M. Sandrini, R. Valcarenghi, R. D. Bini, M. S. Gibin, V. S. Zanuto, and R. F. Muniz, “ $\text{Eu}^{2+}/^{3+}$: Yb^{3+} co-doped sodium calcium silicate glass: A case study of a spectral converter,” *Journal of Non-Crystalline Solids*, vol. 650, p. 123341, 2025.
- [116] C. E. Scanferla, C. A. Moreira, A. G. Oliveira, H. dos Santos, M. S. Gibin, F. Sato, R. R. S. de Farias, F. P. Garcia, C. V. Nakamura, and D. M. F. de Oliveira, “Multi-functional $\text{Ca}^{2+}/\text{Mg}^{2+}$ codoped ZnO nano-semiconductors with enhanced photocatalytic performance and photo-modulated antibacterial action for the remediation of methyl orange dye and chlorpyrifos pesticide in binary systems,” *Ceramics International*, 2025.
- [117] A. G. Oliveira, M. S. Gibin, F. P. Garcia, J. de Lara Andrade, M. V. P. Companhoni, P. R. S. Bittencourt, F. Sato, T. Ueda-Nakamura, A. A. W. Hechenleitner, E. A. G. Pineda, *et al.*, “Synthesis and characterization of Zn-modified hydroxyapatite photoactive composites from eggshell residues for bone regeneration,” *Journal of Photochemistry and Photobiology A: Chemistry*, vol. 449, p. 115432, 2024.
- [118] J. W. Berrar, V. A. da Silva Almodôvar, M. S. Gibin, A. P. B. Cavalaro, V. S. Zanuto, A. C. Bento, N. G. C. Astrath, E. V. Bergmann, A. C. Tomé, L. C. Malacarne, *et al.*, “Diketopyrrolopyrrole-based organic dyes and their laser-induced photoactive response,” *Journal of Molecular Liquids*, vol. 398, p. 124208, 2024.
- [119] G. B. G. Cândido, G. N. Fraga, A. R. de Souza Rossin, R. L. Lourenço, M. S. Gibin, V. S. Zanuto, J. Caetano, and D. C. Dragunski, “Influence of Lamotrigine concentration on physicochemical properties and transdermal release using PBAT/PLA electrospun fibers,” *Colloids and Surfaces A: Physicochemical and Engineering Aspects*, vol. 686, p. 133216, 2024.
- [120] L. Spessato, L. H. Crespo, M. C. Silva, M. S. Gibin, F. Sato, M. E. Winkler, and V. C. Almeida, “Tuning photodegradation performance using carbon quantum

- dots and niobium pentoxide,” *Journal of Materials Science & Technology*, vol. 191, pp. 157–167, 2024.
- [121] E. R. Machado Filho, A. Lazzari, B. R. Saraiva, D. E. R. Gonzaga, M. S. Gibin, W. D. dos Santos, F. Sato, and P. T. Matumoto Pinto, “Potential of barley straw pretreated with a lignin inhibitor as an adjunct during beer production,” *International Journal of Food Science and Technology*, vol. 59, no. 5, pp. 3142–3150, 2024.
- [122] G. H. D. R. Almeida, R. S. da Silva, M. S. Gibin, V. H. d. S. Gonzaga, H. Dos Santos, R. P. Igreja, L. A. Fernandes, I. C. Fernandes, T. N. G. Nesiya, F. Sato, *et al.*, “Region-specific decellularization of porcine uterine tube extracellular matrix: A new approach for reproductive tissue-engineering applications,” *Biomimetics*, vol. 9, no. 7, p. 382, 2024.
- [123] G. H. D. R. Almeida, M. S. Gibin, J. d. C. Rinaldi, V. H. d. S. Gonzaga, C. R. Thom, R. P. Igreja, R. S. da Silva, I. C. Fernandes, R. O. Bergamo, L. S. Lima, *et al.*, “Development and Biocompatibility Assessment of Decellularized Porcine Uterine Extracellular Matrix-Derived Grafts,” *Tissue Engineering Part C: Methods*, vol. 30, no. 12, pp. 569–589, 2024.
- [124] A. Lazzari, M. S. Gibin, B. R. Saraiva, F. Sato, C. I. L. F. Rosa, and P. T. M. Pinto, “Top-fermented beer enriched with Ceylon Gooseberry residue—The effect on bioactive compound content and sensorial profile,” *International Journal of Gastronomy and Food Science*, vol. 37, p. 100991, 2024.
- [125] M. Sandrini, J. C. Gemelli, M. S. Gibin, V. S. Zanuto, R. F. Muniz, F. S. de Vicente, and M. P. Belançon, “Synthesis and properties of Cerium-doped organic/silica xerogels: A potential UV filter for photovoltaic panels,” *Journal of Non-Crystalline Solids*, vol. 600, p. 122033, 2023.
- [126] T. Moriwaki, R. Falcioni, M. E. Giacomelli, M. S. Gibin, F. Sato, M. R. Nanni, S. M. Lima, L. H. da Cunha Andrade, M. L. Baesso, and W. C. Antunes, “Chloroplast and outside-chloroplast interference of light inside leaves,” *Environmental and Experimental Botany*, vol. 208, p. 105258, 2023.
- [127] G. N. Fraga, D. C. Dragunski, B. H. Vilsinski, C. K. da Silva Azevedo, H. J. Wiggers, M. G. I. Faria, J. Caetano, M. R. da Costa, V. S. Zanuto, A. R. S. Rossin, *et al.*, “Dressings produced from PVA nanofibers containing chloramphenicol,” *Colloids and Surfaces A: Physicochemical and Engineering Aspects*, vol. 674, p. 131760, 2023.
- [128] M. H. Pacheco, M. S. Gibin, M. A. Silva, G. Montagnini, R. C. Viscovini, A. Steimacher, F. Pedrochi, V. S. Zanuto, and R. F. Muniz, “BaO–reinforced SiO₂–Na₂O–Ca(O/F₂)–Al₂O₃ glasses for radiation safety: on the physical, optical,

- structural and radiation shielding properties,” *Journal of Alloys and Compounds*, vol. 960, p. 171019, 2023.
- [129] G. H. D. R. Almeida, L. N. da Silva-Júnior, M. S. Gibin, H. Dos Santos, B. de Oliveira Horvath-Pereira, L. B. M. Pinho, M. L. Baesso, F. Sato, L. Hernandez, C. R. Long, *et al.*, “Perfusion and ultrasonication produce a decellularized porcine whole-ovary scaffold with a preserved microarchitecture,” *Cells*, vol. 12, no. 14, p. 1864, 2023.
- [130] B. R. Saraiva, A. C. M. Cegudo, M. S. Gibin, J. B. Da Silva, F. Sato, M. L. Bruschi, and P. T. Matumoto-Pintro, “Co-product from debittering process of trub (brewing by-product) as natural antioxidant in processed cheese,” *International Journal of Food Science and Technology*, vol. 58, no. 12, pp. 6752–6760, 2023.
- [131] C. M. Paraíso, J. dos Santos Pizzo, M. S. Gibin, E. A. Volnistem, J. V. Visentainer, F. Sato, S. C. da Costa, M. H. M. Reis, and G. S. Madrona, “Intensified ultrafiltration process for fouling mitigation during concentration of bioactive compounds from hibiscus (*Hibiscus sabdariffa* L.) extract: Innovation by using ultrasound and 3D turbulence promoters,” *Chemical Engineering and Processing-Process Intensification*, vol. 195, p. 109612, 2024.
- [132] M. T. C. Wolowski, A. M. S. Grenier, V. A. de Oliveira, C. Anselmi, M. S. Gibin, L. V. de Castro-Hoshino, F. Sato, C. Perez, R. H. Scheffel, J. Hebling, *et al.*, “Performance of self-etching adhesives on caries-affected primary dentin treated with glutaraldehyde or silver diamine fluoride,” *Journal of the Mechanical Behavior of Biomedical Materials*, vol. 150, p. 106293, 2024.
- [133] R. Muniz, V. Zanuto, M. Gibin, J. Gunha, A. Novatski, J. Rohling, A. Medina, and M. Baesso, “Down-and up-conversion processes in $\text{Nd}^{3+}/\text{Yb}^{3+}$ co-doped sodium calcium silicate glasses with concomitant Yb^{2+} assessment,” *Journal of Rare Earths*, vol. 41, no. 3, pp. 342–348, 2023.
- [134] W. R. Weinand, J. A. Cruz, A. N. Medina, W. M. Lima, F. Sato, R. da Silva Palacios, M. S. Gibin, E. A. Volnistem, J. M. Rosso, I. A. Santos, *et al.*, “Dynamics of the natural genesis of β -TCP/HAp phases in postnatal fishbones towards gold standard biocomposites for bone regeneration,” *Spectrochimica Acta Part A: Molecular and Biomolecular Spectroscopy*, vol. 279, p. 121407, 2022.
- [135] B. R. Saraiva, J. C. Zancheta, M. Sversut Gibin, F. A. Anjo, A. Lazzari, E. R. Machado Filho, F. Sato, and P. Matumoto-Pintro, “Brewing by-product valorisation: trub debittered for nutritional and quality improvement of pasta,” *International Journal of Food Sciences and Nutrition*, vol. 73, no. 7, pp. 915–926, 2022.

- [136] R. Falcioni, T. Moriwaki, M. S. Gibin, A. Vollmann, M. C. Pattaro, M. E. Giacomelli, F. Sato, M. R. Nanni, and W. C. Antunes, “Classification and prediction by pigment content in lettuce (*Lactuca sativa* L.) varieties using machine learning and ATR-FTIR spectroscopy,” *Plants*, vol. 11, no. 24, p. 3413, 2022.